Electrolyte/Membrane Design and Engineering for Durable Zinc-Iodine Redox Flow Batteries

by

Mahboubehsadat Mousavi

A thesis
presented to the University of Waterloo
in fulfillment of the
thesis requirement for the degree of
Doctor of Philosophy
in
Chemical Engineering

Waterloo, Ontario, Canada, 2021

Examining Committee Membership

The following served on the Examining Committee for this thesis. The decision of the Examining Committee is by majority vote.

External Examiner	Prof. **Jiganag Zhou** Department of Mechanical and Materials Engineering, University of Western
Supervisor	Prof. **Zhongwei Chen** Department of Chemical Engineering, University of Waterloo
Internal Member	Prof. **Eric Croiset** Department of Chemical Engineering, University of Waterloo
Internal Member	Prof. **Mark Pritzker** Department of Chemical Engineering, University of Waterloo
Internal-External Member	Prof. **Xianguo Li** Department of Mechanical and Mechatronics Engineering, University of Waterloo

AUTHOR'S DECLARATION

This thesis consists of material all of which I authored or co-authored: see Statement of Contributions included in the thesis. This is a true copy of the thesis, including any required final revisions, as accepted by my examiners.

I understand that my thesis may be made electronically available to the public.

Statement of Contribution

The body of this thesis is based upon a combination of published and unpublished studies.

1. Mahboubeh Mousavi, Gaopeng Jiang, Jing Zhang, Ali Ghorbani Kashkooli, Haozhen Dou, Catherine J. Silva, Zachary P. Cano, Yue Niu, Aiping Yu, and Zhongwei Chen. "Decoupled low-cost ammonium-based electrolyte design for highly stable zinc–iodine redox flow batteries." Energy Storage Materials 32 (2020): 465-476.

I designed and carried out the experiments, collected and analyzed the data, and wrote the final manuscript. Dr. G. Jiang assisted with design experiments, analyzing the data, discussion, and manuscript writing. Dr. J. Zhang assisted in analyzing the data and discussion. Dr. A. Ghorbani assisted with the flow battery cell design and discussion. Mr. Y. Niu assisted with DFT calculations and a part of manuscript writing. Ms. C. Silva and Dr. Z. Cano assisted with discussion and manuscript writing. Dr. Chen and Dr. Yu reviewed the manuscript.

2. Mahboubeh Mousavi, Haozhen Dou, Hamed Fathiannasab, Catherine J. Silva, Aiping Yu, and Zhongwei Chen. "Elucidating and tacking capacity fading of zinc-iodine redox flow batteries." "Chemical engineering journal, accepted"

I designed and carried out the experiments, collected and analyzed the data, and wrote the final manuscript. Dr. H. Fathiannasab helped with the theoretical calculations. Dr. H. Dou and Ms. C. Silva assisted with the discussion. Dr. Chen and Dr. Yu reviewed the manuscript.

3. Mahboubeh Mousavi, Catherine J. Silva, Aiping Yu, and Zhongwei Chen. "Task-specific organic additives for robust zinc-iodine redox flow batteries."

I designed and carried out the experiments, collected and analyzed the data, and wrote the final manuscript. Ms. C. Silva assisted with the discussion. Dr. Chen and Dr. Yu reviewed the manuscript.

Abstract

Integrating renewable energy sources into the electricity grid has caused an essential need for large-scale energy storage systems. To fulfill this purpose, redox flow batteries (RFBs) are considered one of the best options to be employed in medium- to large-scale applications. As novel and rapidly growing RFB technologies, zinc-iodine redox flow batteries (ZIFB) exhibit great potential for high energy density large-scale energy storage. However, their practical use has been limited by their poor stability, low efficiency, and high cost. In addition, capacity fade and elusive operational instability over charge-discharge cycling severely hinder their large-scale commercialization of ZIFBs. This thesis focuses on the design and engineering of electrolytes and membranes for durable and low-cost ZIFBs to pave the way for future electrolyte research in high-energy-density storage systems.

In the first study, we implemented a novel strategy to improve the performance and cyclability of ZIFBs, as well as decrease the chemical cost, by utilizing ammonium-based electrolytes. The designed ammonium chloride supported zinc-iodine redox flow battery (AC-ZIFB) achieved a high energy density of 137 Wh L^{-1}, Coulombic efficiency of ~99%, energy efficiency of ~80%, and a cycle-life of 2,500 cycles at an 11-times lower chemical cost than conventional ZIFBs. Such improvements were mainly attributed to the multifunctional roles of cost-effective chemicals utilized in a new decoupled electrolyte design, which mitigates the zinc dendrite formation, facilitates the anodic and cathodic reaction kinetics, and unlocks extra capacity with the primary aid of I_2Cl^- formation. The new design empowered the AC-ZIFB with excellent potential as a robust and practical redox flow battery and more broadly demonstrates a facile strategy of using multifunctional electrolyte chemistry to achieve a reliable, high-performance, and cost-competitive energy storage system. However, when the costly perfluorinated Nafion membrane was replaced with low-cost porous membranes, the AC-ZIFBs suffered from capacity fade and elusive operational instability over charge-discharge cycling, which

hinders their successful penetration into the market. Thus, the next two studies focus on the design and engineering of AC-ZIFBs with low-cost porous polyolefin membranes.

In the second study, the capacity fade in AC-ZIFBs with porous polyolefin (PE) membranes was investigated by systematically evaluating electrochemical performance and electrolyte properties. It was found that the differential hydraulic pressure at both sides of the porous membrane leads to colossal electrolyte transport from catholyte to anolyte via convection. Consequently, an accumulation of (poly)iodide at the negative side is established as cycling proceeds, leading to substantial capacity fade of the flow cells. To remediate the capacity fade, an effective strategy was proposed by adjusting electrolyte flow rate ratios to regulate the induced convection by balancing the hydraulic pressure. Theoretical calculations and experimental analysis confirmed that an asymmetric flow rate condition drastically inhibits catholyte transport and (poly)iodide crossover. Therefore, a strategically designed AC-ZIFB with an optimal catholyte to anolyte flow rate ratio of 1 to 7 was able to achieve energy efficiency (EE) of 82% and cycle life of 1,100 cycles at a high current density of 80 $mA.cm^{-2}$, which is the highest performance of all the reported ZIFBs. The insight gained into the capacity fade mechanism and the proposed methodology to sustain capacity substantially benefit the commercialization of flow batteries, particularly ZIFBs.

In the last study, to combat the convection and subsequent capacity decay, new negative electrolyte (anolyte) chemistries with organic compounds, namely urea and glucose were designed to balance the hydraulic pressure, thereby restricting pressure-dependent active ion transfer across the membrane. In this new design, the urea-supported anolyte was able to triple the lifetime of AC-ZIFBs, while the glucose-based design inhibited the large electrolyte transport and prolonged their cycle life by 25 times. Besides the positive impact of organic additives in balancing the hydraulic pressure, the Zn/Zn^{2+} half-cell study and AC-ZIFB full cell study indicated that both additives also could facilitate zinc reaction kinetics and decrease the ionic resistance of flow batteries, thus improve the electrochemical

performance. The glucose-supported AC-ZIFBs with 1.5 M glucose additive achieved outstanding Coulombic efficiency of ~95% and energy efficiency of ~78% under the current density of 80 mA cm^{-2}, at a cost below 150 US$ kWh^{-1} with discharge times of 8 h. Such improvements in the performance are mainly attributed to the remarkable ability of the designed organic additive-supported anolyte to alleviate electrolyte transport and mitigate capacity decay, all with minimal effect on the cost of the battery system. This straightforward yet impactful strategy to balance electrolyte pressure with the aid of electrolyte chemistries could enable an economically viable scale-up of long-lasting ZIFBs.

Acknowledgements

I would first like to thank my supervisor, Professor Zhongwei Chen, for the guidance and dependable support he provided to me during my PhD degree work. His enthusiasm and openness always made me feel comfortable to work on several different projects during my studies. I also want to thank my entire examining committee for their time in reviewing my proposed work and thesis and for the feedback they gave me.

I would also like to thank all the students and researchers in Dr. Chen's groups for helping me with setting up experiments, giving me suggestions for new things to try, giving me feedback on my writing and presentations, and most importantly for their friendship and kindness. In particular, Dr. Jiang Gaopeng, Dr. Jing Zhang, Dr. Ali Ghorbani Kashkooli, Dr. Haozhen Dou, Catherine Silva, Dr. Zachary Cano, and Dr. Hamed Fathiannasab greatly helped me with my work. I would also like to thank the National Sciences and Engineering Research Council of Canada (NSERC) and the University of Waterloo for providing additional financial support during my studies.

Finally, I would like to thank my family and friends Dr. Elham Karimi, Dr. Kaveh Fereidani, Alireza Zebarjadi, Noushin Farahani, Dr. Sahar Hemmati, Dr. Mina Rafiei, Dr. Elnaz Houlako, Zohreh Hosseinayee, Jake Riesenkonig, Namsimeh Shahrokhi, and Zahra Najafi for their support during my PhD.

Dedication

… this thesis is dedicated to positive change in a world full of opportunity…

Table of Contents

List of Figures

List of Tables

List of abbreviations

RFB – Redox Flow Battery

ZIFB – Zinc-Iodine Redox Flow Battery

ZIBFB – Zinc-Iodine/Bromine Redox Flow Battery

AC-ZIFB – Ammonium Chloride Assisted Zinc-iodine Redox Flow Battery

VRFB – All-Vanadium Redox Flow Batteries

XPS – X-ray Photoelectron Spectroscopy

XRD – X-ray Diffraction

SEM – Secondary Electron Microscopy

DFT – Density Functional Theory

NMR – Nuclear Magnetic Resonance

GF – Graphite Felt

N117 – Nafion 117 Membrane

PE – Polyethylene

CE – Coulombic Efficiency

VE – Voltage Efficiency

EE – Energy Efficiency

LSV – Linear Sweep Voltammetry

CV – Cyclic Voltammetry

CE – Counter Electrode

RE – Reference Electrode

GCE – Glassy Carbon Electrode

HER – Hydrogen Evolution Reaction

Chapter 1
Introduction

1.1 Research Background and Motivation

The increasing global energy demand and growing environmental concerns for climate change have accelerated the transition in energy consumption from fossil fuels to alternative clean renewable resources such as solar, wind, hydroelectric, wave, and tidal energy [1,2]. However, the energy management of these inherently intermittent renewable resources is rather challenging due to the lack of high capacity energy storage [3]. In order to ensure power network stability and reliability, highly effective large-scale electrochemical energy storage is of significant interest and need [4,5]. Among different electrochemical energy storage systems, redox flow batteries (RFBs) offer a better deal in medium- to large-scale stationary applications in terms of reliability, safety, and cost [4,6]. Figure 1.1 depicts the typical structure of an RFB. Two pumps circulate the electrolytes, containing dissolved electro-active species, from the tanks to the surface of inert electrodes in the cell stack, where the electron transfer reactions take place [7]. The positive electrolyte (catholyte) is reduced while the negative electrolyte (anolyte) is oxidized during discharge. The reactions in the catholyte and anolyte are reversible, allowing the battery to be recharged [3,8]. The energy capacity of RFBs is determined by the volume of electrolyte tanks and the concentration of the active redox couple species, while the power rating is determined by the cell electrode area and the number of cells in the stack. Since power is decoupled from the capacity in these batteries, RFBs are ideally suited for renewable energy storage [3,8] .

Since 1986, several aqueous redox flow battery systems have been presented and studied. Among them, the all-vanadium redox flow battery (VRFB) [9] is the most developed system due to the high reversibility of the redox reactions in aqueous solutions and relatively large power output [10,11]. Despite these benefits, the relatively high cost of electrolytes [11] and the insufficient chemical stability

of most membranes to the strongly oxidative V(V) species [10] are amongst the main pitfalls of VRFBs. The strong oxidative electrolyte limits the membrane options to expensive Nafion series due to their high chemical stability [12], which contributes to the high cost of VRFBs.

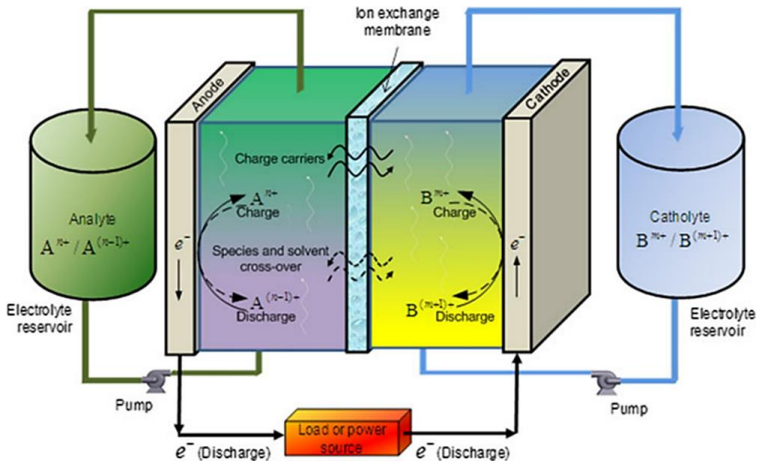

Figure 1.1. A schematic illustrating the operation of redox flow batteries (RFBs) [8].

Regarding the use of less oxidative chemistries to extend membrane durability, zinc-iodine redox flow batteries (ZIFBs) have gained much interest as the next-generation RFBs for their exceptional energy density [5,11,13–19]. Based on the cyclic voltammogram of ZnI_2 on glassy carbon electrodes (Figure 1.2a), a cell with the OCV of 1.29 V was constructed with the redox reaction in Eqs. 1.1-1.3:

$$\textbf{cathode:} \quad I_3^- + 2e^- \leftrightarrow 3I^- \quad E^0 = 0.54\text{V vs SHE} \quad \textbf{(1-1)}$$

$$\textbf{anode:} \quad Zn \leftrightarrow Zn^{2+} + 2e^- \quad E^0 = -0.76\text{V vs SHE} \quad \textbf{(1-2)}$$

$$\textbf{overall:} \quad Zn + I_3^- \leftrightarrow Zn^{2+} + 3I^- \quad E = 1.30\text{ V} \quad \textbf{(1-3)}$$

Figure 1.2b shows a schematic of the Zn-I_2 system of interest. A commercial Nafion 115 (N115) cation exchange membrane (CEM) is placed between two graphite felt electrodes (GFA5, SGL company), while a zinc iodide (ZnI_2) solution is pumped in the two half cells. During discharge, zinc

ion (Zn^{2+}) is reduced at the negative side and deposited on the negative electrode, while iodide (I^-) is oxidized to triiodide (I_3^-) on the positive electrode.

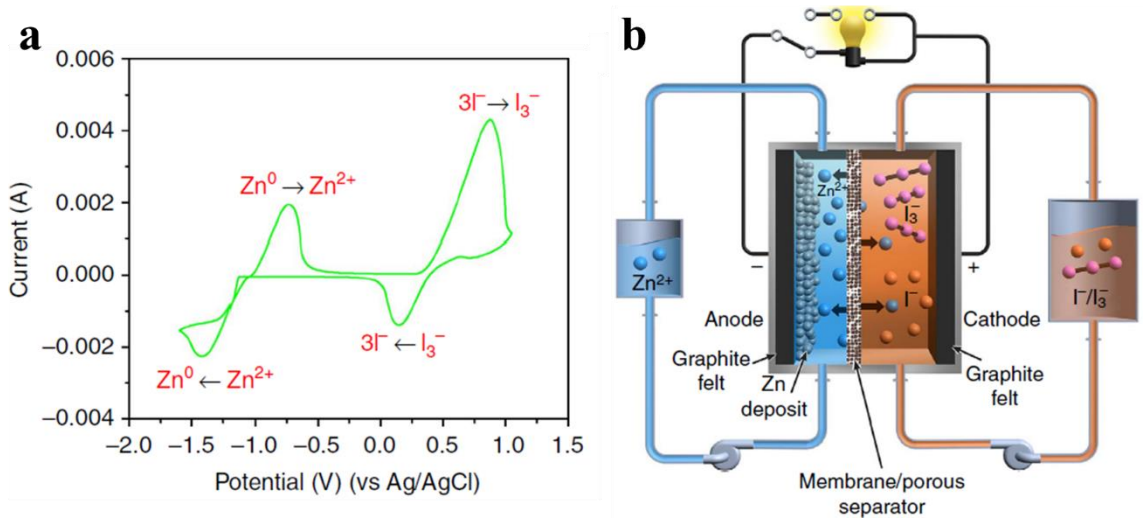

Figure 1.2. The zinc-iodine redox flow battery basics. a) CV of both redox reactions in anolyte and catholyte, and b) The schematic of zinc-iodine redox flow batteries [19].

Some of the main reasons that ZIFBs are among the most promising candidates for future commercial RFBs include their high energy density (167 WhL^{-1}) (Figure 1.3), use of weaker acids as supporting electrolytes, and utilization of environmentally friendly components [19]. Yet, ZIFBs face several challenges in extending the battery capacity, voltage, and cycle life to reach their full potential. Different approaches could address some of these issues by modifying electrolyte design via the incorporation of complex-forming ions like bromide [17] and tailoring the pH of the anolyte [16]. The main remaining challenges are to therefore implement cost-effective and reliable electrolytes and membranes to not only achieve a desirable performance but also reach the US Department of Energy (DOE) target for broad market penetration. By acknowledging the fact that little effort has been devoted to investigating these two important components, the development of ZIFBs' electrolytes and membranes could open a new window to the commercialization of ZIFBs.

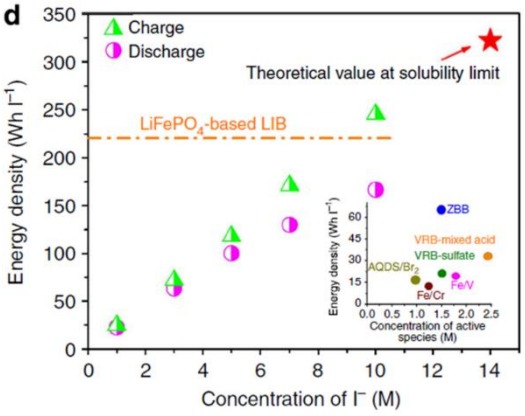

Figure 1.3. The charge and discharge energy densities as a function of I^- concentration. The inset lists other aqueous RFBs for comparison [19].

1.2 Thesis Objectives and Structure

The objectives of this research are to

(i) design robust electrolytes for ZIFBs to improve their electrochemical performance and cycle life while lowering their cost by utilizing reliable and cost-effective materials.

(ii) successfully implement low-cost, porous membranes for high power density ZIFBs by adjusting operational parameters.

(iii) design promising anolytes to integrate low-cost, porous membranes into ZIFBs.

The overall structure of this thesis is presented in Figure 1.4. The content of this thesis is arranged in six chapters. Aside from the current chapter which introduces the research motivations, a brief background and literature review on zinc based RFB chemistries, development of ZIFBs and RFB membranes are presented in **Chapter 2**. **Chapter 3** presents the electrolyte modification of ZIFBs in a decoupled low-cost ammonium-based electrolyte design. The electrochemical performance, cycle life, solution chemistry, and cost evaluation were thoroughly investigated in the newly presented

ammonium-based ZIFBs (AC-ZIFBs). **Chapter 4** deals with a further modification of the AC-ZIFBs with low-cost porous polyolefin (PE) membrane. New insight into the capacity fade mechanism of AC-ZIFBs with porous membranes was discovered and explained. From this, the anolyte to catholyte flow rate ratio adjustments were suggested as a strategy to alleviate active ion crossover, which could improve the electrochemical performance and cycle life. **Chapter 5** presents new anolyte design with additives to inhibit electrolyte transport in the AC-ZIFBs with low-cost porous polyolefin (PE) membranes. The electrochemical performance of two organic additives (urea and α-D-Glucose) and their effect on zinc redox reaction was studied, and the mechanism of how additives extend cycle life was explained. Finally, **Chapter 6** draws general conclusions and highlights the original contributions of the thesis work. Some recommendations for future research are also provided. Figure 1.5 demonstrates an overview of the electrolyte and membrane configurations in this thesis.

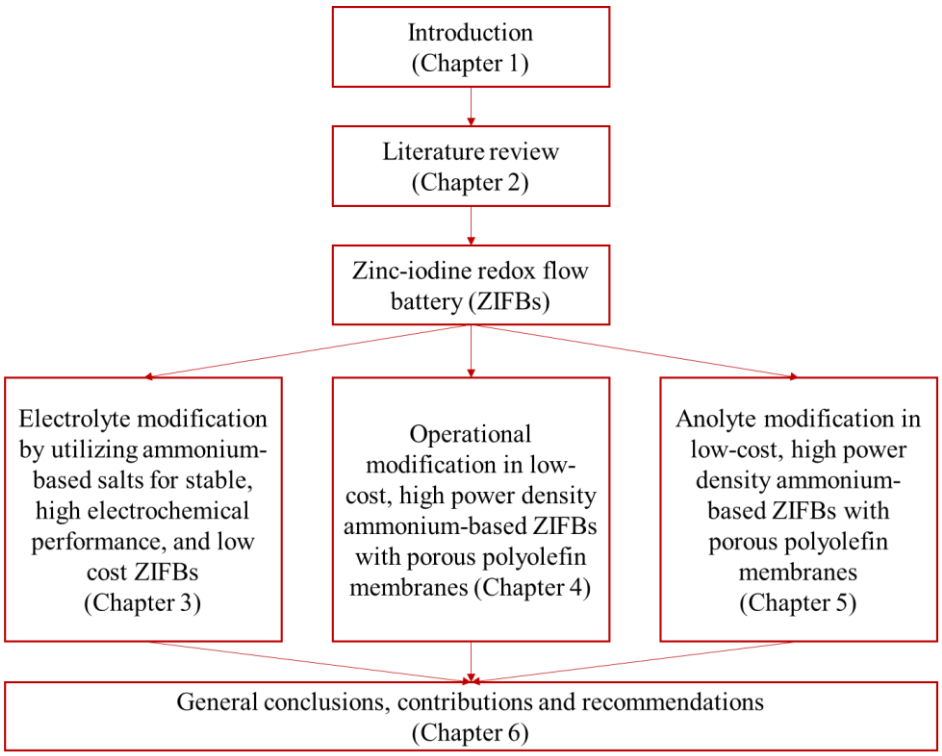

Figure 1.4. Thesis layout.

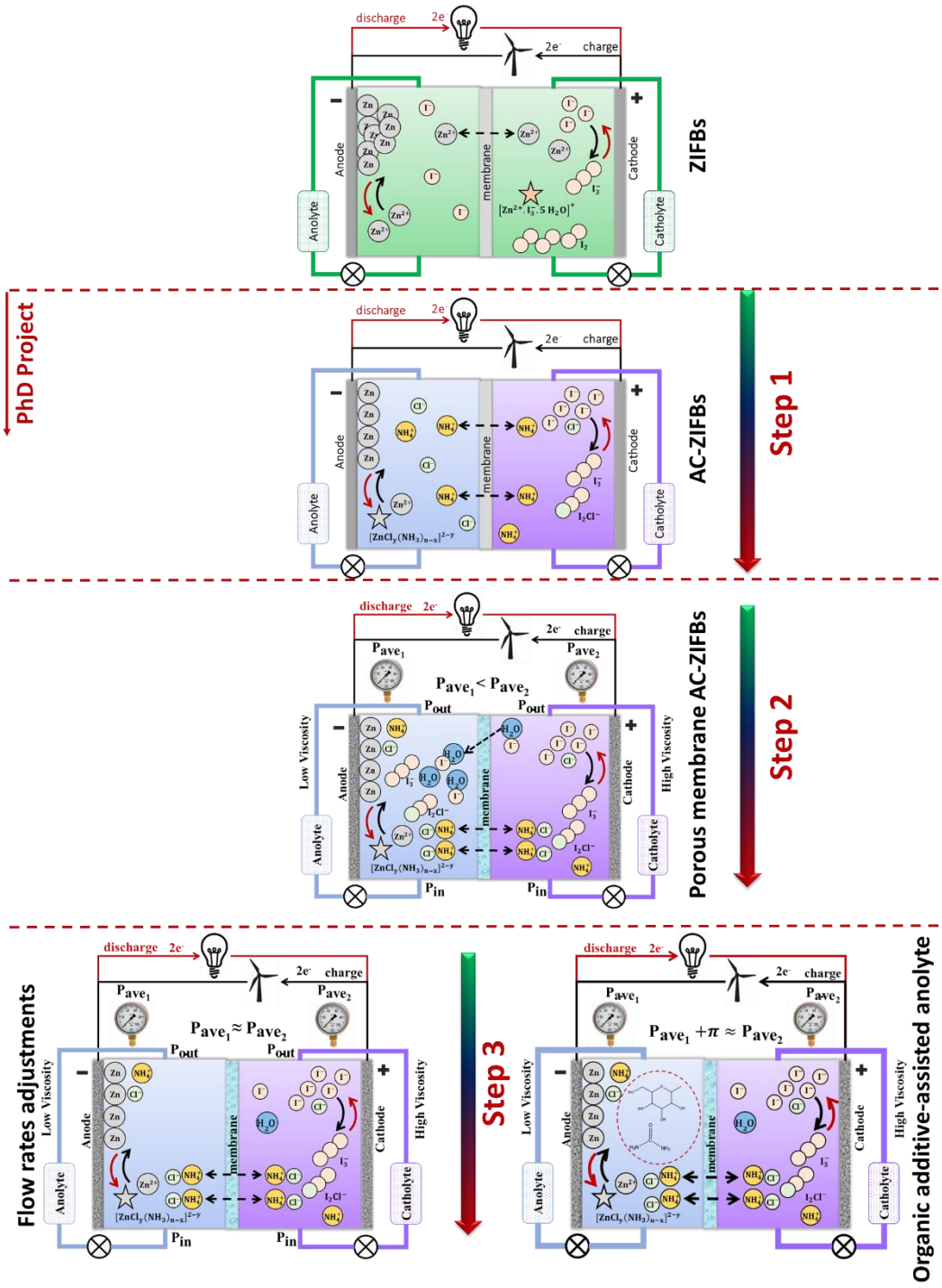

Figure 1.5. Key steps to achieve the research project objectives as illustrated in the original proposal.

Chapter 2
Literature Review

2.1 Redox Flow Batteries

A continued reliance on renewable energy sources has drawn increasing attention to grid-scale energy storage systems. Redox flow batteries (RFBs) are a type of grid-scale energy storage technology that has exhibited exceptional promise for mitigating output fluctuations of renewable energies [20]. Figure 2.1 demonstrates power vs. duration diagram for different energy storage systems. Due to the independency of power and capacity, RFBs can provide a wide range of power and discharging times, from 5 kW to 10 MW and from 30-sec to 1-day, respectively. Besides scalability and flexibility, fast response, reduced environmental impact, high efficiency, and durability are amongst the most attractive features of RFBs [6].

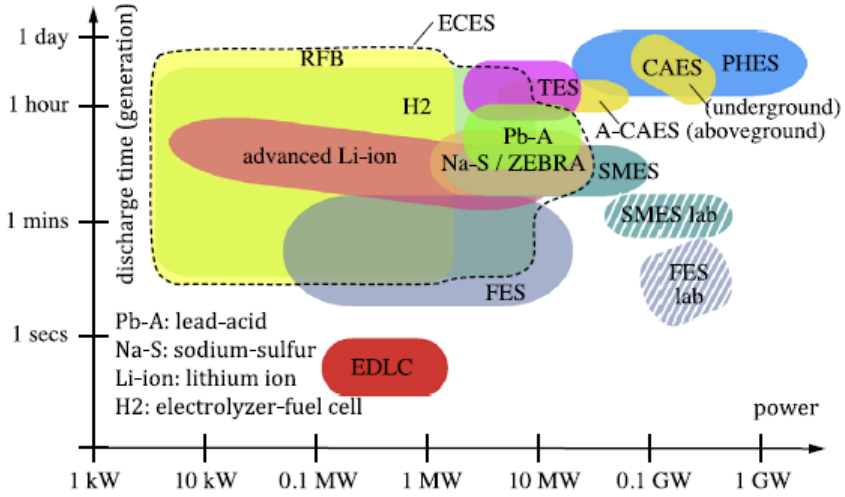

Figure 2.1. Power vs discharge time (duration) diagram for different energy storage systems [6].

The performance of RFBs is highly related to their electrolyte media and dissolved redox-active materials. The non-aqueous electrolytes offer better electrochemical stability and a wider potential

window but at the cost of higher viscosity, ionic resistivity, and cost of electrolytes [21], while the aqueous electrolytes are the most widely used media in RFB chemistries because of better safety, lower cost, and higher ionic conductivity. The electroactive species can be organic or inorganic (mostly metals) materials. The organic-based RFBs are receiving considerable interest because of their low cost and high reversibility in all-liquid RFBs; however, one of their main disadvantages is their low energy densities due to the limited solubilities of active compounds and the low voltage of the cells [11]. Thus, conventional RFBs based on inorganic materials are still more promising than their organic counterparts.

The metal-based redox couples, also known as hybrid RFBs, are a group of inorganic-based RFBs that are renowned because of their relative low-cost and high cell voltage [22]. Zinc, lead, iron, manganese, cadmium, and chromium are the highly abundant, low-cost metal candidates for hybrid RFBs. Among them, zinc has long been the center of attention in primary and secondary batteries due to having the highest energy content as a result of large volumetric capacity (5.85 Ah cm^{-3}) and negative electrode potentials in aqueous solutions (-0.76 V vs SHE in acidic and -1.26 V vs SHE in alkaline) [11].

2.2 Zinc-based Redox Flow Batteries

Aqueous Zn-based RFBs have become a major area of research for energy-storage applications in recent decades thanks to their very negative electrode potential, fast kinetics, great abundance, high solubility, and easy recyclability of zinc compounds. The electro-deposition (plating) and dissolution reaction of zinc can take place in (nearly)acidic or alkaline media by the following reactions [23]:

$$\mathbf{Zn^{2+}+2e^{-}\leftrightarrow Zn_{(s)} \quad E^{0}=-0.76\ V\ vs.\ SHE \quad (2\text{-}1)}$$

$$\mathbf{Zn(OH)_4^{2-}+2e^{-}\leftrightarrow Zn_{(s)}+4OH^{-} \quad E^{0}=-1.26\ V\ vs.\ SHE \quad (2\text{-}2)}$$

Besides these reactions, the hydrogen evolution reaction (HER) is also thermodynamically favorable at the surface of Zn electrodes. However, a large hydrogen overpotential and suitable electrolyte composition of most Zn-based RFBs make the zinc deposition highly efficient (current efficiencies of over 90%). As a result of these positive features, zinc has been coupled with several positive electrode reactions in solid, liquid, and gas phases (Figure 2.2) to provide a desirable voltage and capacity for renewable energy storage. Among zinc-based RFBs, zinc-bromide, zinc-cerium, zinc-nickel, zinc-iron, and zinc-iodine chemistries have received more interest.

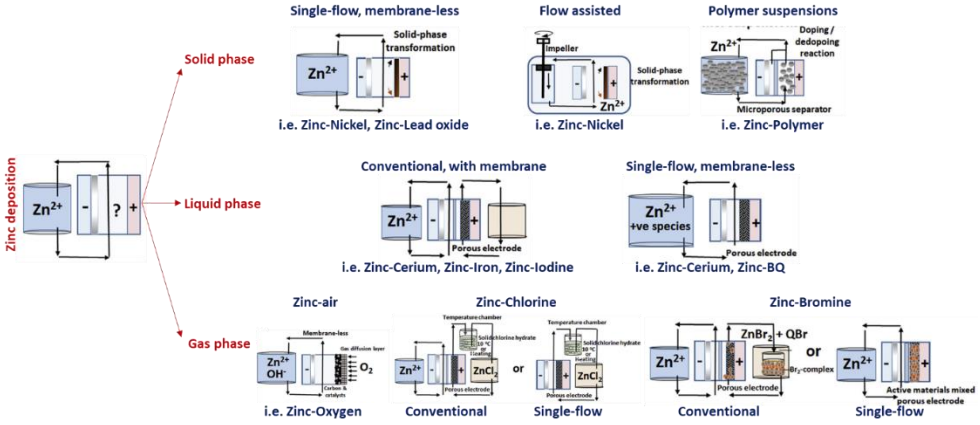

Figure 2.2. Zn-based RFB systems with positive redox reactions in solid, liquid and gas phases [11].

Zinc-Bromide (Zn-Br) RFBs

Zinc-Bromide (Zn-Br) RFBs are the most renowned Zn-based RFBs with almost 50 years of development. Low cost, relatively high open-circuit voltage (OCV) of 1.82 V (Eq. 2-3), and the theoretical energy density of 570 Wh kg^{-1} (70 Wh kg^{-1} in practice) are amongst the main advantages of Zn-Br RFBs. However, high self-discharge and the presence of strongly corrosive bromine in the catholyte are the two main problems of the system [9]. Several complexing agents have been added to the catholyte to bond with the bromine and resolve this problem. Upon addition of these agents, a higher

density Br_2-rich layer with complexing agent additives will form. Thus, a complex flowing system is required in a practical large-scale Zn-Br RFBs [24].

$$\mathbf{Zn+Br_2 \leftrightarrow Zn^{2+}+2Br^-} \qquad \mathbf{E=1.82\ V} \quad \mathbf{(2\text{-}3)}$$

Zinc-Cerium (Zn-Ce) RFBs

Zinc-cerium (Zn-Ce) RFBs are the next well-studied systems with one of the highest OCV of 2.37 V (Eq. 2-4) in RFBs with aqueous electrolytes. To slow down the oxygen evolution reaction and ensure high solubility of active materials, methanesulfonate acid (MSA) solutions have been used as supporting electrolytes in the system. The main limitation of Zn-Ce RFBs is the necessary use of high-cost platinum/titanium positive electrodes due to corrosion of carbon-based electrodes in oxidative cerium electrolytes. Besides the high cost, platinum/titanium positive electrodes have high catalytic activity towards the oxygen evolution reaction, limiting the performance of the battery [9].

$$\mathbf{Zn+2Ce^{4+} \leftrightarrow Zn^{2+}+2Ce^{3+}} \qquad \mathbf{E=2.37\ V} \quad \mathbf{(2\text{-}4)}$$

Zinc-Nickel (Zn-Ni) RFBs

As environmentally-friendly alternatives to zinc-cadmium secondary batteries [25], static zinc-nickel (Zn-Ni) batteries were introduced with a porous matrix of zinc oxide (negative electrodes) and sintered nickel (positive electrodes). The static Zn-Ni batteries were constructed with a cell voltage of 1.7 V (Eq. 2-5). Later, circulating the electrolytes in Zn-Ni RFBs could mitigate some of the problems with the static system including the zinc dendrite formation, shape change, and passivation [11]. A single-flow, membrane-less Zn-Ni RFBs were introduced later by borrowing the concept of lead-acid batteries. The Zn-Ni RFB achieved 86% energy efficiency for 1000 cycles, due to the decreased thickness of the diffusion layer, and subsequent concentration polarization at the surface of the electrode [26].

$$\mathbf{Zn+2\ KOH+2H_2O+2NiOOH \leftrightarrow 2Ni(OH)_2+2K_2Zn(OH)_4} \quad \mathbf{E=1.7\ V\ (2\text{-}5)}$$

Zinc-Iron (Zn-Fe) RFBs

Zinc-iron (Zn-Fe) RFBs have been studied in alkaline, acidic, and alkaline-acidic supporting electrolytes. The main advantage of Zn-Fe RFBs is its utilization of two of the lowest-cost, most-abundant metals in the earth's crust. The conventional Zn-Fe RFBs with alkaline-based electrolytes are also known as "zinc-ferricyanide" batteries. Despite higher cell potential, handling solid zinc oxide precipitates is one of the major problems in zinc based RFBs with alkaline electrolytes. Thus, alkaline-based Zn-Fe RFBs suffer from low durability as a result of zinc oxide precipitation. The acidic version of Zn-Fe RFBs was also constructed with an OCV of 1.53 V (Eq. 2-7) [27]. Two acidic systems are presented in Zn-Fe RFBs: i) by using mixed solution of zinc and iron as anolyte and catholyte, ii) by using electrolyte contains zinc in negative side and iron in positive side. The energy efficiency of 60% at 25 mA cm^{-2}, and columbic efficiency of 91% at 30 mA cm^{-2} was achieved in mixed solution and decoupled one, respectively [11]. The alkaline-acidic supporting electrolyte version of Zn-Fe RFBs with a high power density of 676 mW cm^{-2} and OCV of 2.0 V (Eq. 2-8) was introduced by utilizing supporting solutions with different PH in anolytes (alkaline) and catholytes (acidic) in a double-membrane, three-electrolyte design. The main purpose of such an electrolyte design was to boost the cell voltage of Zn-Fe RFBs [28]. Nonetheless, the high resistance and slow ion diffusion caused by the middle electrolyte, and the low durability of the system due to handling of solid zinc oxide precipitations are the main barriers for this system.

$$\mathbf{Zn + 4\,OH^- + 2Fe(CN)_6^{3-} \leftrightarrow Zn(OH)_4^{2-} + 2Fe(CN)_6^{4-} \quad E = 1.58\ V \quad (2\text{-}6)}$$

$$\mathbf{Zn + 2Fe^{3+} \leftrightarrow Zn^{2+} + 2Fe^{2+} \quad E = 1.53\ V \quad (2\text{-}7)}$$

$$\mathbf{Zn + 4\,OH^- + 2Fe^{3+} \leftrightarrow Zn(OH)_4^{2-} + 2Fe^{2+} \quad E = 2.0\ V \quad (2\text{-}8)}$$

Zinc-Iodine RFBs (ZIFBs)

The zinc-iodine primary system with metallic zinc and potassium iodide was first introduced in a lecture demonstration of electrochemical reactions in 1949. The purpose of the primary system was to illustrate the importance of reactant and product arrangements with respect to the form of energy (heat, electricity, or both) liberated [29]. Around seven decades later, rechargeable zinc-iodine RFBs (ZIFBs) with a high energy density of 167 Wh L^{-1} were proposed by Bin et al. in 2015 [19]. A cell with the OCV of 1.29 V (Eq. 2-9) was attained during discharge by the deposition of Zn on the negative electrode, and oxidation of iodide (I^-) to triiodide (I_3^-) on the positive electrode. Both electrolytes contained zinc iodide (ZnI_2) solution, without any addition of acid or alkaline, which lead to electrolyte with the pH of 3-4 at 0%SOC.

Later in 2017, Weng et al. [17] reported another kind of ZIFB by using Br^- ions in catholyte to stabilize the free iodine (I_2) by forming iodine-bromide (I_2Br^-) ions (Eq. 2-10). The concept of a Br^- ion complexing agent in the zinc-iodine/bromide RFBs (ZIBFB) is presented in Figure 2.3a. With the aid of I_2Br^- formation, the ZIBFBs could achieve higher energy density (202 Wh L^{-1}) than the conventional ZIFBs. However, utilizing the same electrolyte for both half-cells increase the cost of the ZIFB and ZIBFB systems since the imported cost of iodine to the US is as expensive as the vanadium metals [11].

$$\mathbf{Zn^{2+}+3I^-\rightarrow Zn+I_3^-} \quad \mathbf{E=-1.299\ V} \quad \mathbf{(2\text{-}9)}$$

$$\mathbf{Zn+I_2Br^-\leftrightarrow 2I^-+Br^-+Zn^{2+}} \quad \mathbf{(2\text{-}10)}$$

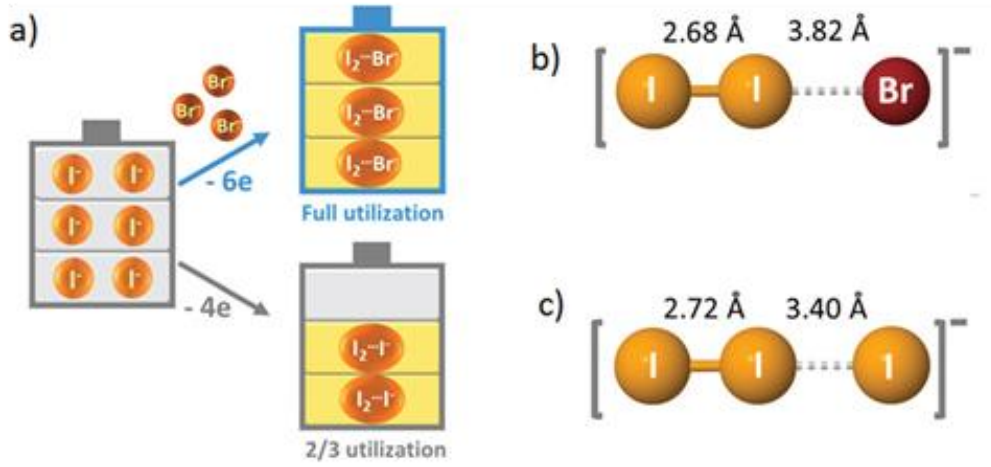

Figure 2.3. Conceptual illustration of bromide complexing agent to stabilize iodine. a) the extended capacity by introducing bromide, b) the chemical structure of I_2Br^-, and c) the chemical structure of I_3^-. [17]

In 2018, Zhang et al. [16] presented an alkaline-based ZIFB that could achieve a higher OCV of 1.796 V (Eq. 2-11), using a similar concept to alkaline-based Zn-Fe RFBs. The alkaline-based ZIFB outweighs the conventional ZIFBs by a 0.497 V increase in battery voltage (Figure 2.4a) and 0.47 in OCV (Figure 2.4b), which further leads to a 38.26% enhancement in energy density [16]. However, low cycle life, as a result of zinc oxide formation in alkaline solutions, and energy efficiency are concerns that still need to be overcome in this system.

$$Zn + I_3^- + 4\,OH^- \leftrightarrow Zn(OH)_4^{2-} + 3I^- \quad E = 1.796\ V \qquad (2\text{-}11)$$

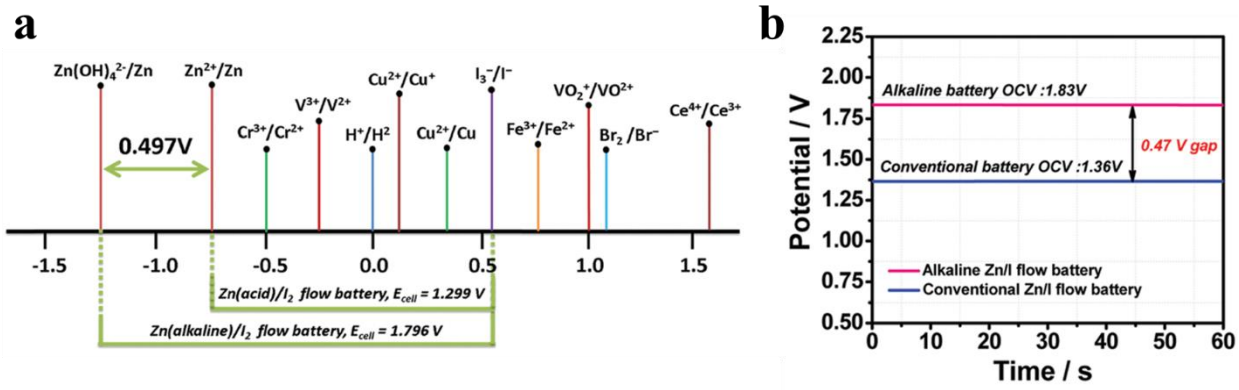

Figure 2.4. Concept illustration of alkaline-based zinc-iodine redox flow batteries. a) The standard redox potentials of some redox pairs in aqueous RFBs. b) The open-circuit-voltage comparison of conventional and alkaline-based ZIFBs. [16]

The schematics of these variations of ZIFBs and the energy density they could provide are presented in Figure 2.5. Due to the partial formation of I_2Br^-, ZIBFBs could achieve higher capacity than that of conventional ZIFBs (Figure 2.5d). However, due to both high voltage and specific capacity, the alkaline-based ZIFBs achieved the highest energy density (330.5 WhL^{-1}) among all the presented ZIFBs (Figure 2.5f) [16].

Similar to other hybrid RFBs, the overall capacity of chemistries based on ZIFBs is limited by the zinc negative electrode, despite the fact that the iodide redox species are highly soluble (e.g. lithium iodide: c.a. 8.2 M; zinc iodide:c.a.5.6 M, potassium iodide: c.a. 8 M) in aqueous solutions. In addition, all these ZIFB chemistries suffer from short cycle-life, low current density, and high cost due to utilizing costly Nafion membranes [11]. The zinc-based redox flow batteries operating conditions are summarized in Table 2.1.

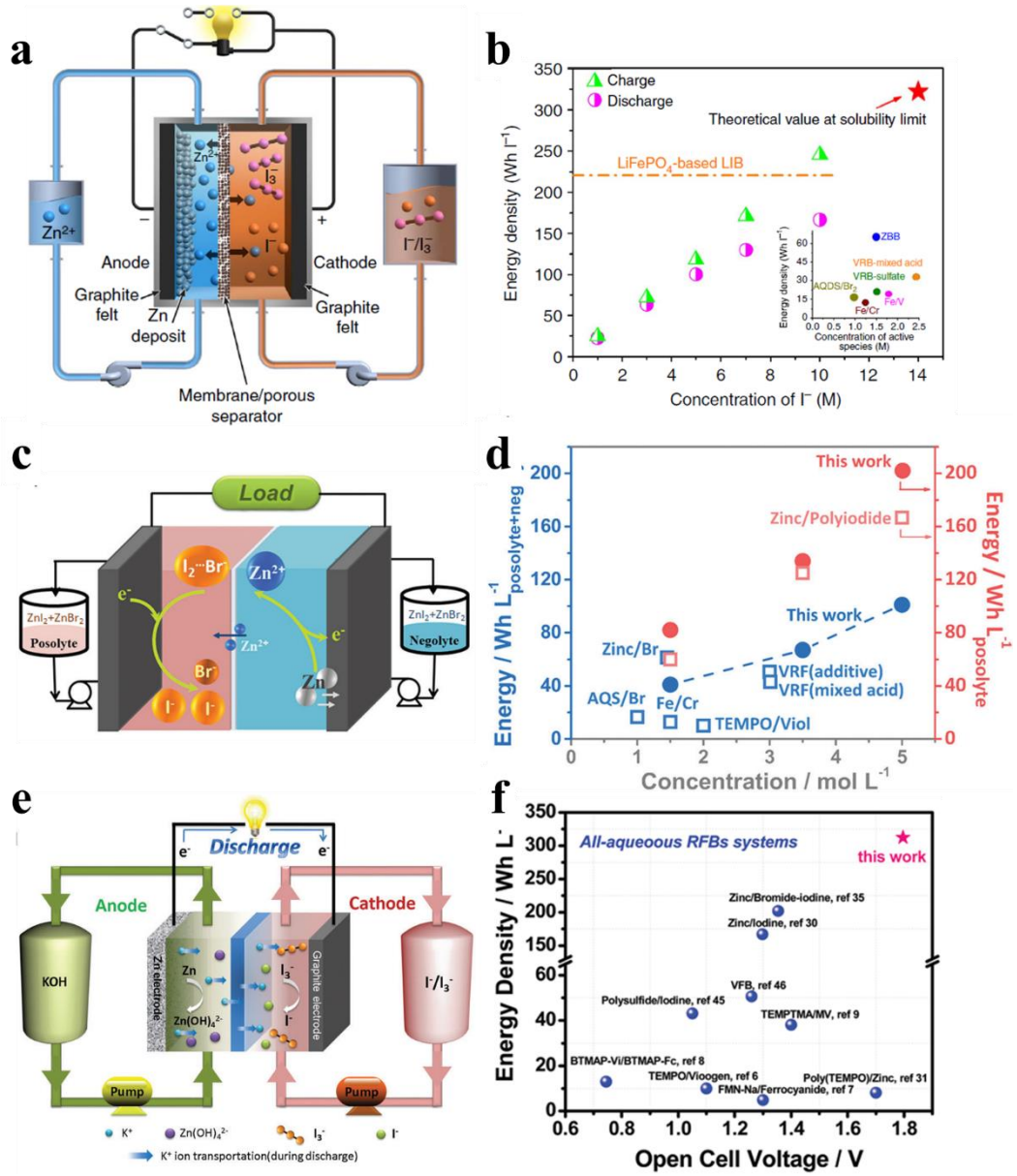

Figure 2.5. The schematic and energy density of a,b) conventional zinc-iodine redox flow batteries (ZIFBs), c,d) zinc-iodine/bromine redox flow batteries (ZIBFBs), and e,f) alkaline-based zinc-iodine redox flow batteries. [16,17,19]

Table 2.1. The summary of Zn-based RFBs operational parameters.

Redox couples	Catholyte	Anolyte	Cathode	Anode	Membrane	Overall discharge reaction	E^0 V vs. SHE	J mA/cm^2	EE %
Zn-Br_2 [30]	2M $ZnBr_2$ in 4M KCl		Carbon	Carbon	N 125	$Zn+Br_2 \leftrightarrow Zn^{2+}+2Br^-$	1.8	20	80
Zn-Ce divided	0.8 M $Ce(CH_3SO_3)_3$+4 .0 M CH_3SO_3H	1.5 M $Zn(CH_3SO_3)_2$+1 .0 M CH_3SO_3H	Pt-Ti mesh stack	carbon polymer plate	N 117	$Zn+2Ce^{4+} \leftrightarrow Zn^{2+}+2Ce^{3+}$	2.3	50	46
Zn-Ce undivided [31]	1.5 M $Zn(CH_3SO_3)$2+0.2 M $Ce(CH_3SO_3)_3$ in 0.5 M CH_3SO_3H		Carbon felt	Carbon plastic	-	$Zn+2Ce^{4+} \leftrightarrow Zn^{2+}+2Ce^{3+}$	2.4	20	75
Zn-Ni undivided [26]	1 M ZnO in 10 M KOH		Ni hydroxide	Cd-plated Ni foil	-	$Zn+2\ KOH+2H_2O+2NiOOH \leftrightarrow 2Ni(OH)_2+2K_2Zn(OH)_4$	1.7	10	86
Zn-Cl_2 undivided [32]	2M $ZnCl_2$ in 4M KCl		Porous graphite	Dense graphite	-	$Zn+Cl_2 \leftrightarrow Zn^{2+}+2Cl^-$	2.1	22	66
Zn-Fe (Mixed pH) [28]	1M $FeCl_2$+1 M HCl	0.5 M $Na_2[Zn(OH)_4]$	Carbon felt	Copper mesh	N 212/ FAA-3 FuMa-Tech	$Zn+4\ OH^-+2Fe^{3+} \leftrightarrow Zn(OH)_4^{2-}+2Fe^{2+}$	2.0	80	60
Zn-Fe (Acidic) [27]	1M $FeCl_2$+1.5 M H_2SO_4	1M $ZnSO_4$+1.5 M NaAc+1.5 HAc	Carbon felt	Zinc foil/Carbon felt	HZ115	$Zn+Fe^{3+} \leftrightarrow Zn^{2+}+Fe^{2+}$	1.53	30	60
Zn-I_2 [19]	5 M ZnI_2		Graphite felt	Graphite felt	N 115	$Zn+I_3^- \leftrightarrow Zn^{2+}+3I^-$	1.3	20	67
Zn-I_2/Br_2 [17]	5 M ZnI_2+ 2.5 M $ZnBr_2$		Graphite felt	Graphite felt	N 117	$Zn+I_2Br^- \leftrightarrow 2I^-+Br^-+Zn^{2+}$	1.4	10	68
Alkaline Zn-I_2 [16]	6M KI + 6M I_2	6 M KOH	Graphite foil	Zn plate	N 117	$Zn+I_3^-+4\ OH^- \leftrightarrow Zn(OH)_4^{2-}+3I^-$	1.8	20	70

2.3 Membranes for Redox Flow Battery Applications

Membranes play key roles in RFBs by preventing cross-mixing of the positive and negative electrolytes, while still allowing the transport of carrier ions to complete the circuit during the passage of current [33]. An ideal membrane for an RFB system must have five key characteristics: (1) good chemical stability under electrolyte conditions (2) high ionic conductivity of the charged carrier to keep the electroneutrality in balance, (3) high ion selectivity to prevent the cross-mixing of active species, (4)

good mechanical strength, and (5) low cost [34]. Ion exchange membranes and porous membranes are the two main types of separators that have been used widely in RFBs.

2.3.1 Ion Exchange Membranes

Ion exchange membranes (IEMs) were proposed in 1980 by realizing that if a membrane is impermeable to an electrolyte then it is impermeable to its cation or anions. The IEMs are categorized into cation exchange membranes (CEMs: contain cationic groups), anion exchange membrane (AEM: contains anionic groups), and amphoteric ion-exchange membranes (contains both cationic and anionic groups) [9]. The IEMs have fixed ion functional groups and oppositely charged counter ions to balance the charge. The functional group forms an electrostatic bond with an ion of the opposite charge, acting as an exchange site. Through the ion exchange process, the mobile counter ion can be replaced by another ion with the same type of charge from the solution [35,36].

Among different types of IEMs, fluorinated CEMs are the most utilized membranes in different aqueous RFB systems due to their exceptional chemical stability towards reductants and oxidants in acidic and alkaline media with moderate concentrations. The most well-known type of these membranes is manufactured by Dupont company under the commercial name of Nafion. The structure of the Nafion membrane is shown in Figure 2.6. As can be seen in the Nafion structure, the sulfonic acid groups are bound to the polymer backbone by polypropylene glycol ether [9].

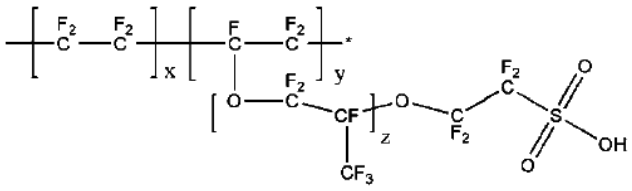

Figure 2.6. Structure of fluorinated cation exchange membrane (Nafion) [35].

Ion transport through Nafion membranes have been explained via several models, including water channel and cluster-network models. The sulfonic acid functional groups are the hydrophilic water channels through which small ions can be easily transported (Figure 2.7); while the hydrophobic polymer backbone with crystallite structure provides the proper mechanical stability [35].

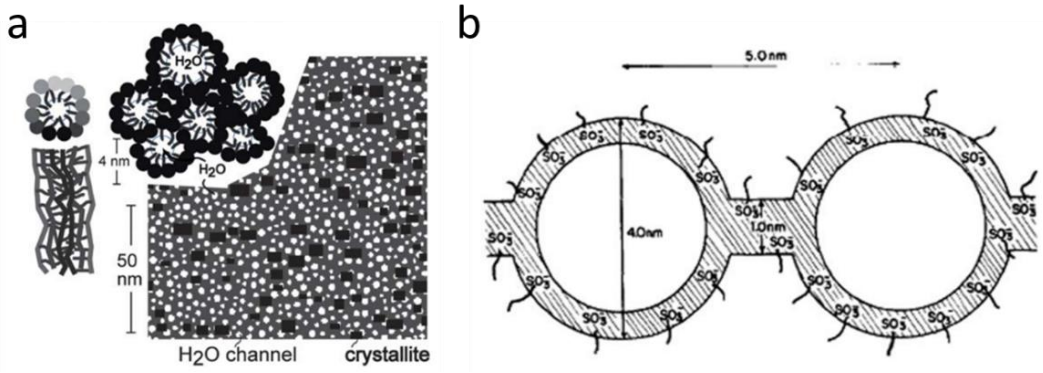

Figure 2.7. The schematic of ion transport by a) Water channel, and b) cluster-network model for the Nafion membranes [35].

However, the Nafion membrane suffers from high cost and poor ion selectivity. The use of ultra-thin Nafion membranes is able to decrease the total cost by utilizing less amount of polymer, however, it also lowers the mechanical stability of the membrane [37]. Thus, mechanically stable substrates (mostly a porous membrane) are typically used in these methods to achieve higher mechanical properties. Coating or mixing Nafion with other materials such as graphene and graphene oxide also showed promising results due to a reduction in the membrane resistance, increase in its mechanical stability, and ionic selectivity [38,39].

2.3.2 Porous Membranes

As an alternative to Nafion membranes, low-cost porous membranes have received great attention due to their comparable electrochemical performance in RFBs. Porous membranes, prepared from polymer

materials filled with inorganic fillers, have also been used in the wastewater treatment industry, flooded lead-acid batteries, and Li-ion batteries [40,41]. It is worth noting that most traditional porous membranes do not possess ion-exchange capabilities. Instead, the porous membrane capitalizes on the different transport speeds of the different ionic species in the liquid electrolyte to achieve the ion separation. For example, in all-vanadium redox flow batteries (VRFBs), the protons and vanadium ions have different Stokes radii and charge densities. As a result, the time required to move through the membrane varies from ion to ion, which is a characteristic that can be exploited to accomplish desirable ion selectivity. For this reason, the combination of pore size and thickness of the membrane is particularly important to ensure the redox reaction can be finished with satisfactory Columbic (CE), voltage (VE) and energy efficiency (EE) [42]. With a lower thickness, more ions can crossover and less Coulombic efficiency is achieved; however, the voltage efficiency is higher due to the lower membrane resistance [40].

Hydrophilicity, mechanical, and chemical stability are three important factors when choosing a porous polymer membrane for an RFB system. The hydrophilicity of the membrane is important in achieving desirable ion conductivity and transport of charge carriers across the membrane, as well as low ohmic resistance. Since most polymeric feedstock materials such as sulfonic acid, carboxylic acid, or quarterly ammonium pendants do not possess hydrophilic functions in their structure, using inorganic fillers with high water absorption properties is required in making a hydrophilic porous polymer membrane. Silica, titania, and zirconia are suitable filler materials for RFB porous polymeric membranes [43]. In addition, the porous polymeric membrane should be flexible and mechanically strong so that they do not break during high compression sealing of the cell stack. For this reason, inorganic porous membranes (such as ceramic ones) are not suitable due to their rigidity. By contrast, porous polymeric membranes are flexible, with cross-linked backbone chains and mechanically stable inorganic fillers, making them suitable for RFB applications [44]. Lastly, the chemical stability of a

membrane can determine the electrochemical performance and cycle life of an RFB system. For a membrane to have a long useful life without degradation, the polymers and fillers should be chosen carefully based on the PHs and level of corrosivity of electrolytes.

2.3.3 Chemical Stability of Membranes in Redox Flow Batteries

In most RFBs, strong acidic solutions are used to provide fast transport of H^+ charge carriers and stabilize the electro-active materials at higher electrolyte concentrations [45]. All- vanadium (All-V) [46], iron- chromium (Fe-Cr) [47–52], all-iron (All-Fe) [53], zinc-vanadium (Zn-V) [54,55], zinc-cerium (Zn-Ce) [56] are examples of RFBs which require highly acidic electrolyte media such as sulfuric acid (H_2SO_4), hydrochloric acid (HCl), methanesulfonic acid (CH_3SO_3H), and mixtures of these acids. The strong acidic environment coupled with the high oxidation potential of the positive half-cell can easily degrade a wide range of polymer materials [45]. The same phenomenon can happen in RFB systems with high oxidation active materials in neutral or alkaline-based electrolytes. Thus, the chemical stability of the membranes is one of the major factors in the expected cycle life of an RFB. Since Nafion membranes are highly stable towards reductants and oxidants, most membrane studies in RFBs focus on presenting porous membranes with chemical stability comparable to Nafion.

Both polymer and inorganic filler in porous polymeric membranes must be chemically stable in the electrolyte environment [43,57]. Depending on the acidic or alkaline environment of electrolytes, some polymers cannot be used as polymer feedstocks. In Zn-Fe [28] and Zn-Ce [58,59] systems, for example, polymers such as polyamide and polyimide cannot be implemented because of their susceptibility to acidic hydrolysis breaking the polymer backbone. Less-durable polymers such as polyolefin-based (Daramic), functionalized olefin-based polymers, and polyacrylonitrile can be safely used in RFB systems with less oxidative electrolytes such as Fe-Cr and Fe-V [60]. However, in more oxidative systems such as VRFBs, Daramic membranes degrade much faster than fully fluorinated membranes such as PTFE membranes because of the presence of highly oxidative V(V) [61].

With a similar concept, polymers such as polyethylene terephthalate (PET) [42], polyvinylidene fluoride (PVDF), and vinylidene fluoride (VDF) copolymers [62] cannot be used in electrolytes containing alkali hydroxide due to their cleavage in alkaline solutions.

Chemically stable membranes for ZIFBs

It is not surprising that halogen-based electrolyte environments act as a poison to easily degrade a wide range of polymer materials. Most polymers such as polysulfone are unstable in chlorine, bromine, and iodine-based RFBs such as bromine- polysulphide (Br-S), vanadium-bromide (V-Br), zinc-bromine (Zn-Br), zinc- chloride (Zn-Cl), zinc- iodide (Zn-I) [63–65]. The insufficient chemical stability of the membranes and the consecutive active species crossover will result in a decrease in CE. The degradation of the membrane can also cause larger polarization which will diminish the VE [66].

Unlike VRFBs, little effort has been made in investigating other RFB membranes especially in chemistries including bromine and iodine electrolytes. It is reported that in the presence of bromine, the sulfonate groups that are directly bonded to the benzene rings (like sulfonated polystyrenes) are susceptible to rapid replacement by bromine (Figure 2.8), thus reducing the membrane performance. The rate of degradation is critically dependent on the activity of free bromine, and chemical degradation occurs through the thickness of the materials and is not limited to their surfaces. When the sulfonate group was directly bonded to the phenyl ring, the degradation occurs via a substitution reaction mechanism where the bromine present in solution acts as a Lewis acid (or electrophile). The product chemical functional group is stable and difficult to replace [64]. In a general sense, similar polymer structures will probably suffer in bromine-based electrolytes for the same reason.

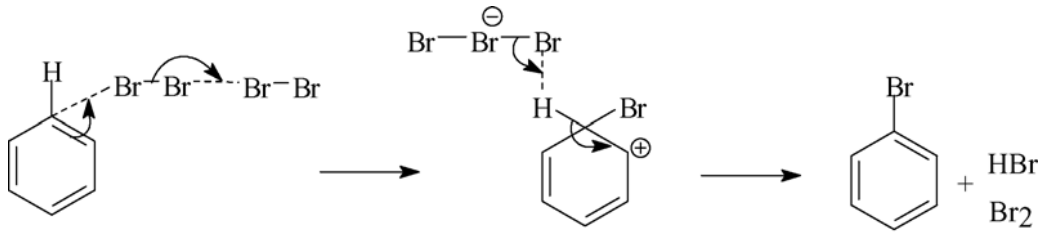

Figure 2.8. Bromination of benzene in aqueous bromine/bromide solution [64].

However, if the sulfonate group is directly attached to a fluorinated linear chain, i.e. perfluorosulfonic acid type membranes, it would be stable in bromine environment [64]. Carbon fluorine structures such as PTFE and PVDF (Figure 2.9) are also stable in these environments [64].

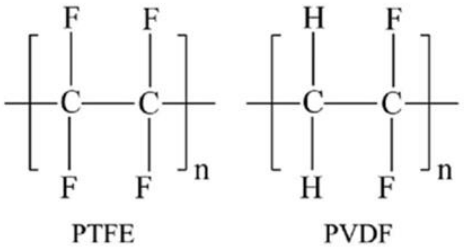

Figure 2.9. Chemical structure of PTFE and PVDF.

While these groups of polymers are relatively expensive, microporous polyolefin (PE) membrane presents as viable options due to their low cost (1-20 US$ m^{-2}) [60], high ion conductivity, and good chemical stability [15] in both bromine and iodine [15] electrolytes. The chemical structure and the schematic of ion transport across of PE membranes are presented in Figure 2.10. However, unlike the ion-exchange membranes, the ion selectivity by these porous membranes is mainly controlled by pore size and Donnan exclusion, and the water and ion transport through the pores can be significant. Thus, the implementation of porous PE in RFB systems can be challenging as it is essential to inhibit the active ion crossover to achieve a desirable electrochemical and cycling performance [67].

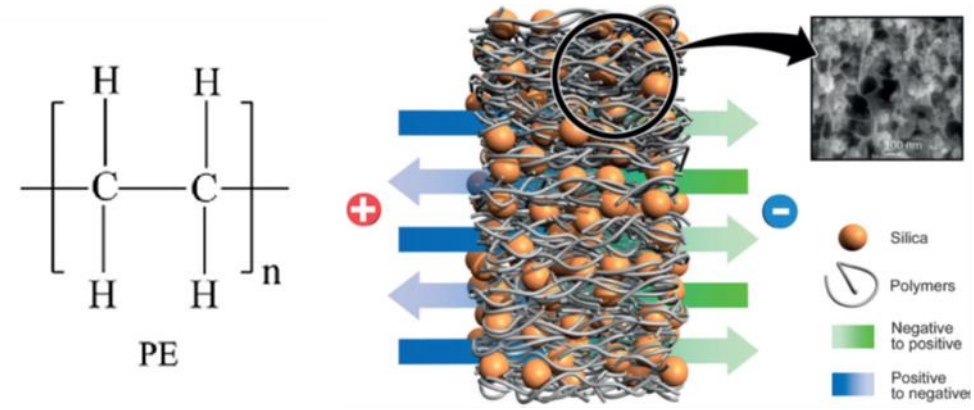

Figure 2.10. Chemical structure of polyolefin (PE) and schematic transportation principle of ions and water with porous PE membranes (in VRBs) [68].

Chapter 3

Decoupled Low-Cost Ammonium-based Electrolyte Design for Highly Stable Zinc-Iodine Redox Flow Batteries

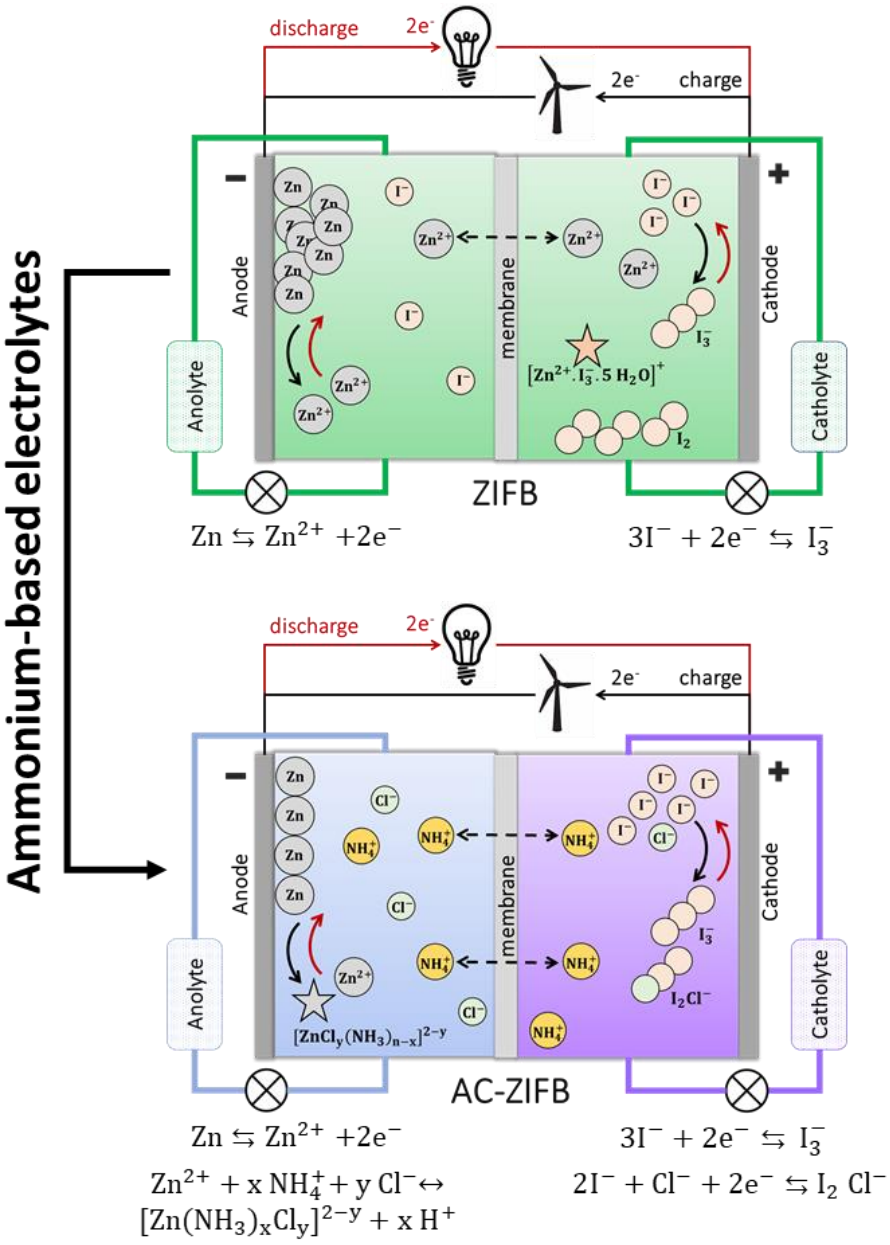

3.1 Introduction

Redox flow batteries (RFBs) are among the most promising candidates for storing energy from clean intermittent renewable resources due to their design flexibility, reliability, and short response time [6,8,9,13,14,69]. However, of the wide range of RFB systems, none has significantly penetrated the marketplace due to various limitations such as low energy density [70–78], poor electrochemical performance [8,79,80], insufficient cycle life [28,80–82], and high cost [8,80]. Among the various RFB chemistries, the zinc-iodine RFB (ZIFB) has emerged as an attractive system with remarkable volumetric energy density related to the utilization of the highly-soluble zinc iodide (ZnI_2) compound conventionally used as both electrolytes (Figure 3.1a) [15,17,19,83–85]. However, several challenges must be addressed for its successful advancement. First, the poor cyclability of ZIFBs, resulting mainly from zinc dendrite formation and insoluble iodine (I_2) precipitation, strongly hinders its practical applications [17,19]. The change in pH during the charging process for the sole ZnI_2-based anolyte can cause hydrolysis of Zn^{2+} and growth of dendrites [15]. The ZnI_2-based electrolyte accelerates formation of I_2 from triiodide (I_3^-) dissociation via the formation of a zinc-complex [19]. In addition, the use of ZnI_2 can also simultaneously produce zinc oxide and iodine through its reaction with O_2 and H_2O [15]. Second, the system suffers from insufficient performance, experiencing limited molar capacity, low voltage efficiency (VE) and low energy efficiency (EE). The molar capacity of the ZIFB is typically limited since one third of the I^- ions coordinate with I_2 to form I_3^- ions instead of entirely participating in electron transfer during charging [17]. The low VE and EE are linked to electrolyte and membrane conductivity and slow kinetics of the redox reactions at the anode and cathode. Third, the use of relatively expensive ZnI_2 for both the anolyte and catholyte increases the total cost of ZIFBs [11,86]. Specifically, the failure to reach the U.S. Department of Energy (DOE) cost target is one of the main hindrances preventing RFBs from successful commercialization [6,8,14,28]. Thus, it is very important to develop new electrolytes for ZIFBs that importantly enhance performance at an economical price.

Herein, an ammonium chloride (NH_4Cl) supported zinc- iodine RFB (AC-ZIFB), based on the ammonium iodide/triiodide (NH_4I/NH_4I_3) electrochemical redox couple, configured as a decoupled electrolyte design, has been introduced to overcome the aforementioned challenges (Figure 3.1b). The novel electrolyte design is shown to have several significant advantages. Firstly, ammonium salts can tune the solution chemistry to suppress formation of zinc dendrites and insoluble iodine. The separation of Zn^{2+} and I^- in the NH_4^+-based electrolyte also prevents the coupled formation of zinc (hydr)oxide and iodine, which typically occurs in the ZnI_2 electrolyte counterpart [15]. In addition, the abundant NH_4^+ ion functions as a weakly acidic buffer to inhibit the hydrolysis of Zn^{2+} and promote uniform deposition of Zn during charging through the formation of coordinated species [78]. At the same time, the chloride (Cl^-) ions can bond with I_2 to form I_2Cl^- in the presence of NH_4^+, which hinders I_2 precipitation during charging. Secondly, the NH_4Cl addition enhances the RFB performance in terms of capacity, voltage and energy efficiency. The formation of I_2Cl^- frees up some of the I^- ions from the formation of I_3^- and hence unlocks additional capacity and, by extension, improves the energy density of the AC-ZIFB. Moreover, the NH_4Cl supporting electrolyte increases the electrolyte and membrane ionic conductivity and significantly improves the kinetics of both I_3^-/I^- and Zn^{2+}/Zn redox reactions, resulting in high VE and EE. Thirdly, replacing the relatively costly ZnI_2 with more cost-effective ammonium salts (i.e. NH_4I, NH_4I_3, or NH_4Cl) in both the catholyte and anolyte effectively reduces the chemical cost of the system. As a result, the installed cost of the AC-ZIFB system in this work drops to one-fifth of the cost of conventional ZIFB designed for a 1-day discharge time. Finally, this electrolyte design strategy provides a battery system with operational flexibility by showing enhanced performance and cyclability independent of starting operation (i.e. starting with either discharge or charge). This new zinc-iodine design was able to achieve an unprecedented cycle life of 2,500 cycles with a high capacity of 128 Ah L^{-1}, high energy density of 137 Wh L^{-1}, excellent Coulombic and energy efficiency of ~99% and ~80%, respectively and achieved the 2023 DOE cost target for RFBs (<150

US$ kWh^{-1}) [28] with the use of polyethylene (PE) membrane with only 5 hours discharge duration. The breakthrough strategy of using a multifunctional supporting electrolyte chemistry combined with a promising decoupled arrangement paves a new path towards reliable, high-performance, and low-cost future RFBs.

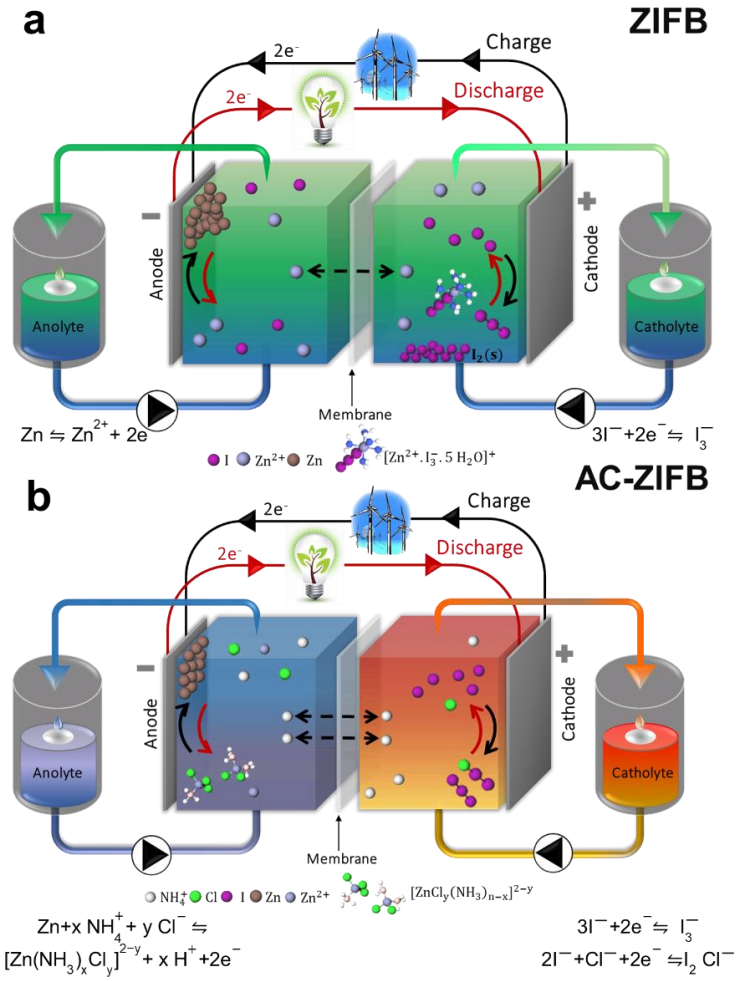

Figure 3.1. Zinc-iodide RFB chemistry. Schematic illustration of a) the conventional ZIFB using zinc iodide electrolyte and b) the AC-ZIFB using ammonium-based electrolyte.

3.2 Materials and Methods

3.2.1 Assembly of the Lab-scale Redox Flow Battery

The ZIFB and AC-ZIFB flow batteries were fabricated by sandwiching a Nafion 117 membrane (N117) between two pieces of heat-treated porous graphite felt (H-GF, SGL Carbon Group, Germany) embedded between graphite plates with an apparent area of 3 cm×3 cm. The fabricated cell was fixed between two aluminum plates (Figure 3.2).

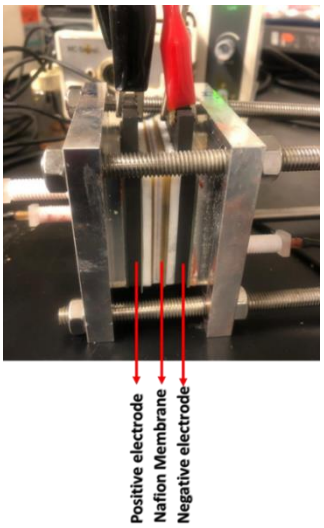

Figure 3.2. Cell assembly of ZIFB and AC-ZIFB.

The H-GF was heat-treated at 500 ℃ for 2 h in an air atmosphere [87], heating rate set to 5 ℃/min (Figure 3.3). N117 underwent a sequential pretreatment in the following boiling solutions for 1 h each: 3% H_2O_2, DDI water, 0.5 M H_2SO_4 and DDI water. Different concentrations of catholyte solutions were prepared by dissolving appropriate zinc iodide ($ZnI_2 \geq 98\%$, Aldrich), ammonium iodide ($NH_4I \geq 99\%$, Aldrich), and ammonium chloride ($NH_4Cl \geq 99.5\%$, Aldrich) in deionized water. Different concentrations of anolyte solutions were prepared by dissolving appropriate zinc iodide ($ZnI_2 \geq 98\%$, Aldrich), zinc chloride ($ZnCl_2 \geq 98\%$, Aldrich), and ammonium chloride

($NH_4Cl \geq 99.5\%$, Aldrich) in deionized water. The volume of catholyte was designed to be 10 ml while enough anolyte remained available in the anolyte reservoir. The electrolytes were circulated through the cell stack with a flow rate of 1 ml min^{-1} using a peristaltic pump. The battery testing was performed on a potentiostat/galvanostat (Land Electronic Co., Ltd., Wuhan) with the voltage cut-off range of 0.6-1.6 V at constant current densities of 20 mA cm^{-2}. The long-term stability of the AC-ZIFB system with 6.5 M I^- (6.5 M NH_4I/3.25 M NH_4Cl) catholyte composition was tested under a current density of 10 mA cm^{-2}.

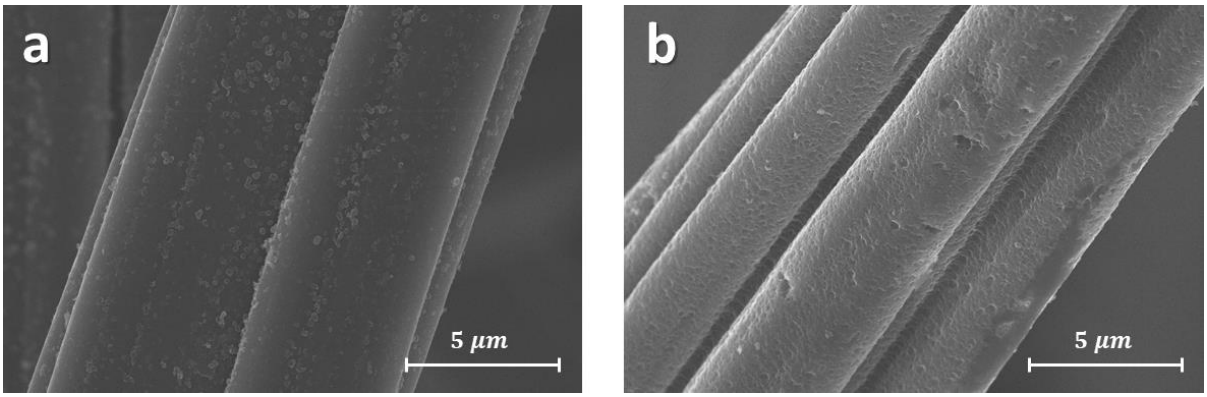

Figure 3.3. SEM images of Graphite Felt (GFA5) a) before and b) after heat treating for 2 h at 500 °C with 5 °C/min ramp rate.

The ZI_3FB and AC-ZI_3FB were fabricated the same way by sandwiching a N117 membrane between H-GF embedded in graphite plate with an apparent area of 3 cm×3 cm (positive electrode) and a well-polished zinc plate with sandpaper (negative electrode). Similarly, the fabricated cell was fixed between two aluminum plates (Figure 3.4). Different concentrations of catholyte were prepared by dissolving an appropriate amount of iodine ($I_2 \geq 99.8\%$, Aldrich) with NH_4I and NH_4Cl solutions, while original anolytes were prepared with corresponding concentrations of NH_4Cl in balanced osmolarity. The electrolytes were circulated through the cell stack with a peristaltic pump at a flow rate of 1 ml min^{-1}, and the charge/discharge cycling tests were done at a constant current density of 10 mA cm^{-2}.

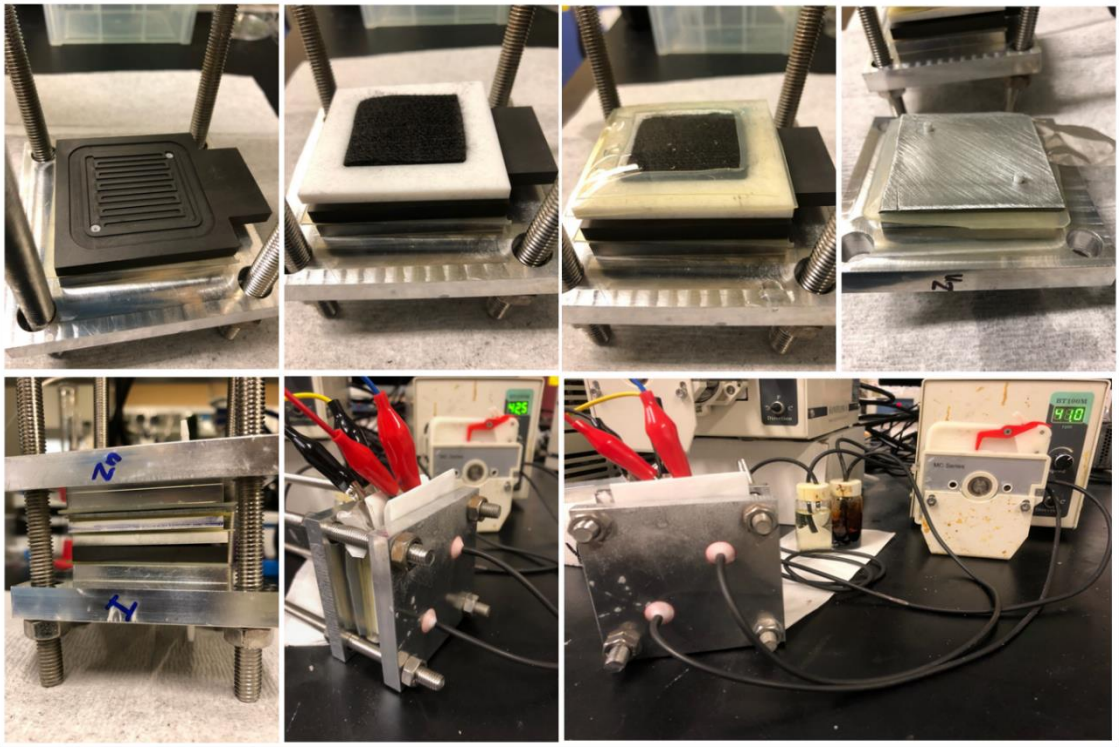

Figure 3.4. Cell assembly of ZI_3FB and AC-ZI_3FB test cells.

3.2.2 Catholyte Electrochemical Characterization

Electrochemical measurements for catholyte half-cell investigation were conducted using an electrochemical workstation (Biologic VSP 300). The three-electrode configuration was employed using a platinum wire, glassy carbon electrode (GCE, 0.196 cm^{-2}) and Ag/AgCl (filled with 3 M KCl) electrode as the counter, working and reference electrodes, respectively. All half-cell studies were conducted in either 10 mM (NH_4I-NH_4I_3) solution or a mixed solution of 10 mM (NH_4I- NH_4I_3) and 15 mM NH_4Cl. All the electrolytes were purged with nitrogen gas for 15 min prior to each experiment, and all experiments were conducted at room temperature.

The cyclic voltammetry curves were obtained using a static GCE at a scan rate of 20 mV s^{-1} and a potential sweep from -0.4 V to 1.0 V (vs Ag/AgCl) to oxidize I^-, followed by a reverse sweep back to -0.4 V to reduce the I_3^- at the surface of the GCE. The diffusion coefficient the reactants of the iodide oxidation and polyiodide reduction reactions were measured with the Randles-Sevick method. Cyclic voltammetry with different scan rates were carried out in the catholyte solutions, and the diffusion coefficient was estimated by:

$$\mathbf{i_p = 0.4463\ nFAc_0\ (\frac{nFvD}{RT})^{\frac{1}{2}}} \qquad \textbf{(3-1)}$$

where i_p is peak current (A); F is Faraday constant (C mol^{-1}), T is temperature (K), n is the number of electron transfer (n=2), A is the electrode surface area (0.196 cm^2), D is the diffusion coefficient (cm^2 s^{-1}), c_0 is the bulk concentration of active species (0.01 M), and v is the scan rate (V s^{-1}).

Linear sweep voltammetry (LSV) was also conducted on a GCE to measure diffusion of I^- ions in dynamic state through the Levich method. The catholyte solutions were studied at the scan rate of 5 mV s^{-1}. The results exhibited mass transport-controlled limiting currents with various plateaus at different rotation rates from 100 to 1600 rpm, and the corresponding electrochemical kinetics of the charge transfer of triiodide/iodide redox couples was calculated by [88,89]:

$$\mathbf{i_L = 0.620\ nFAD^{\frac{2}{3}}\omega^{\frac{1}{2}}\upsilon^{-\frac{1}{6}}c_0} \qquad \textbf{(3-2)}$$

where i_L is the Levich current (A), n is the number of electron transfer (n=2), F is Faraday's constant (96,485 C mol^{-1}), ω is the rotation speed (rpm), A is the electrode area (0.196 cm^2), D is diffusion coefficient (cm^2 s^{-1}), υ is the kinematic viscosity (0.01 cm^2 s^{-1}), and c_0 is the bulk concentration of the catholyte (0.01 mol cm^{-3}) [88]. Using the slopes of the fitted linear Levich plots, the diffusion coefficient D was calculated.

3.2.3 Anolyte Electrochemical Characterization

Electrochemical measurements for anolyte half-cell were carried out by the same device used for catholyte half-cell investigation. 2 M $ZnCl_2$ solutions and a mixed solution of 2 M $ZnCl_2$ and 2 M NH_4Cl were chosen to carry out the half-cell investigation. All experiments were conducted at room temperature. The CVs were obtained using a static GCE at a scan rate of 20 mV s^{-1} and a potential sweep from 0 V to -1.5 V (vs Ag/AgCl) to deposit the zinc metal at the surface of GCE, producing a nucleation loop at the end of the cathodic scan, followed by a sweep back to 0 V, which produced an anodic peak. The nucleation overpotential (NOP) was calculated by measuring the difference between the potential at which cathodic current is first observed and the potential at which the current switches from cathodic to anodic during the reverse scan (crossover potential). To study zinc deposition kinetics, polarization experiments were carried out by scanning the potential in the OCV±250 mV range at a sweep rate of 2 mV s^{-1}, where the Butler-Volmer equation was fitted to the experimental data to obtain exchange current density (i_0), anodic (β_a), and cathodic Tafel slopes (β_c).

3.2.4 Permeability of Zinc ions

Ion permeability testing was done using membrane (N117)-separated diffusion cells (Figure 3.5). 1 M $ZnAc_2$ ($Zn(CH_3CO_2)_2 \cdot 2H_2O$ >98% , Aldrich) , 1 M $ZnAc_2$ + 1 M NH_4Ac and 1 M $ZnAc_2$ + 1 M NH_4Cl solutions were chosen as feeding solutions in the left reservoir (80 ml) and DDI water was filled in the right receptor reservoir (80 ml). After the first 2 h of diffusion, a certain amount of diffused solution in the right receptor reservoir was sampled every hour. The concentration of Zn^{2+} was determined by ICP-OES (Perkin Elmer Ltd., USA). The slope of the Zn^{2+} concentration curve with respect to diffusion time reflects the permeability of Zn^{2+} across the treated Nafion 117 membrane. The Zn^{2+} ion permeability can be calculated by Fick's law with the following equation [16,90,91]:

$$V_R \frac{dc_R(t)}{dt} = \frac{AP}{L}(c_F - c_R(t)) \qquad (3\text{-}3)$$

Where P is permeability of the zinc ions ($cm^2\ min^{-1}$); c_F is initial Zn^{2+} concentration in the feeding cell ($mol\ L^{-1}$); $c_R(t)$ is the Zn^{2+} concentration in the receptor cell at the diffusion time of t; A is the area of membrane (2.54 cm^2); L is the thickness of the membrane (200 µm); V_R is the volume of the receptor cell (80 ml). The following assumptions were made: the changes in Zn^{2+} concentration in the feeding reservoir are negligible, a pseudo-steady state condition is used inside the membrane, and P is independent of concentration [16,90,91].

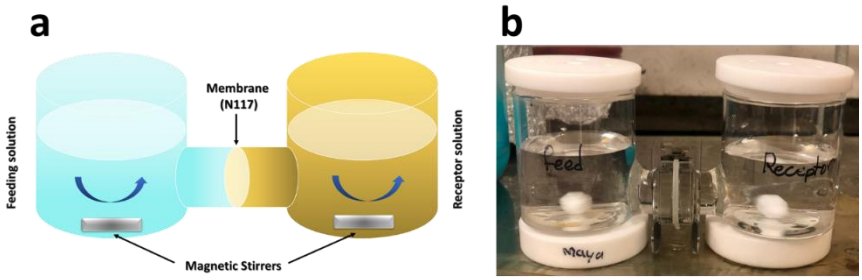

Figure 3.5. a) Schematic representation of diffusion cell used for ion permeability test, b) actual set-up for performing the ion permeability.

3.2.5 Physiochemical Characterization of Electrodes and Electrolytes

The morphology of the graphite felt electrode and zinc dendrites on the anode were imaged by scanning electron microscopy (SEM, LEO FESEM1530). Energy-dispersive X-ray spectroscopy (EDS, LEO FESEM1530) was applied to analyze the elemental composition of zinc dendrites. X-ray photoelectron spectroscopy (XPS, Thermo Scientific, Al K-α X-ray source) was used to analyze the surface chemical composition of the graphite felt electrode. Raman spectra were obtained from a DXR Raman microscope (Bruker Senterra, 532 nm laser) to study polyiodide formation in the catholyte. High resolution electrospray ionization mass spectroscopy (ESI-MS) was run on a Kratos MA890 for 10 µM NH_4I_3-15 µM NH_4Cl catholyte. The ^{1}H-NMR measurements were performed using a Varian

500 Inova spectrometer. The NMR samples were prepared by dissolving the catholyte salts in 1 ml of d-DMSO.

3.2.6 Simulation Method and Computational Modeling

The computational simulations were carried out by Vienna Ab-initio Simulation Package (VASP), which applied projector augmented wave (PAW) pseudo-potentials to reveal the interaction between nuclei and electrons under the direction of Density Functional Theory (DFT). Within the generalized gradient approximation (GGA), the Perdew-Burke-Ernzerhof (PBE) equation was used to describe the electronic exchange and correlation effects. In this work, a graphene supercell with 5 × 5 hexagon units was firstly built. Then, the optimized OH* was anchored on the single-layer graphene to obtain a graphene-OH substrate, which was treated as the model of the electrode. The periodic boundary conditions were set up along the x-axis with a vacuum layer of 15 Å to make the model an infinite tape. The lattice parameter of the model is 12.3 Å × 12.3 Å × 15.0 Å, within which the relaxed graphene piece fits inside. In order to investigate adsorption energy of I_3^- and I_2Cl^- on the as-built single-layer graphene-OH substrate and single-layer graphene (as a contrast), more free space was created in the models along the y and z directions. The Brillioun zone K points meshing was set up as a 2 × 2 × 1 grid making the gamma point centered regarding the Monkhorst Pack Scheme. The simulation was run with a certain setup of INCAR file. The maximum number of ionic steps was 500, the break condition of the electronic SC-loop was 1.0 e^{-5} and 400 eV was used as the cut-off energy. All the simulations were two-step processes, including geometrical optimization and static calculation. The structure of the model was fully relaxed during the geometrical optimization process to obtain all the atoms sitting at the point with the minimum energy. For the calculation process, the adsorptions of I_3^- and I_2Cl^- to the material surface were carried out, and thus the adsorption energy could be obtained.

3.3 Results and Discussion

3.3.1 Ammonium-based ZIFB Designs

The schematic design of the AC-ZIFB is illustrated in Figure 3.1b, and the custom-made cell is shown in Figure 3.2. Two pieces of heat-treated graphite felt (H-GF) were adopted as the cathode and anode and were separated via standard commercial perfluorosulfonic acid (Nafion 117) based cation exchange membrane (CEM). Unlike conventional ZIFB, which uses ZnI_2 as anolyte and catholyte, AC-ZIFB is designed with separated electrolyte. Due to the unique decoupling design of Zn^{2+} and I^- in the electrolyte, counter ions and supporting electrolyte are required in both anolyte and catholyte. In this AC-ZIFB design, NH_4Cl is chosen to be the supporting electrolyte, with NH_4^+ and Cl^- appropriately selected as counter ions. Thus, a formulated anolyte solution of $ZnCl_2$ and NH_4Cl was circulated through the H-GF in the anode while a catholyte mixture of NH_4I and NH_4Cl was circulated through the cathode. Similar to the mechanism of a typical ZnI_2-based ZIFB, when the cell is assembled in the discharged state and is initiated by charging, metallic zinc is electrodeposited on the H-GF anode from the anolyte solution (Eq. 3-4) while I^- ions are oxidized to I_3^- at the electrolyte-electrode interface of the H-GF cathode (Eq. 3-5) [19]. However, in this AC-ZIFB design, the I^- ions can also be oxidized to I_2Cl^- in the presence of the NH_4Cl supporting electrolyte (Eq. 3-6), delivering a similar theoretical cell voltage of a conventional ZIFB, i.e. approximately 1.3 V as calculated from the thermodynamic data in Table 3.1. To maintain ionic charge balance, NH_4^+ ions migrate through the CEM instead of Zn^{2+}, thus decoupling Zn^{2+} and I^-.

$$\textbf{Anode:}\quad \mathbf{Zn(s) \rightleftharpoons Zn^{2+}(aq) + 2e^-} \qquad \mathbf{E^0 = -0.76\ V\ vs.\ SHE} \quad \textbf{(3-4)}$$

$$\textbf{Cathode:}\begin{cases} \mathbf{I_3^-(aq) + 2e^- \rightleftharpoons 3I^-(aq)} & \mathbf{E^0 = +0.54\ V\ vs.\ SHE} \quad \textbf{(3-5)} \\ \mathbf{I_2Cl^-(aq) + 2e^- \rightleftharpoons 2I^-(aq) + Cl^-(aq)} & \mathbf{E^0 = +0.61\ V\ vs.\ SHE} \quad \textbf{(3-6)} \end{cases}$$

During discharge of the battery, deposited Zn particles release electrons and dissolve into the anolyte (Eq. 3-4), forming soluble Zn species ($[Zn(NH_3)_xCl_y]^{2-y}$) in the presence of NH_4Cl [92]. These large-

sized soluble Zn complexes further allow NH_4^+ to be the dominant migrating species through the CEM. At the same time, I_3^- and I_2Cl^-accept the electrons from the external circuit during the discharge process and are reduced into I^- and Cl^- (Eqs. 3-5 and 3-6).

Table 3.1. Thermodynamic data on halides in aqueous state. [23]

Species	I^-	Cl^-	I_3^-	$I_{2(aq)}$	I_2Cl^-
ΔG^0 (kJ mol $^{-1}$)	-51.67	-131.06	-51.50	16.43	-115.98

According to Eq. 3-5, the molar capacity of the NH_4I solution is relatively low as only 2/3 electrons are transferred in the reaction per mole of NH_4I. However, 2 electrons are transferred per mole of NH_4I_3. This indicates 3 times higher potential molar capacity of NH_4I_3 than that of NH_4I, which is also 1.5 times higher than that of a conventional ZIFB (See calculation details in Appendix 1). Thus, to further boost the molar capacity, an alternative AC-ZIFB system is also designed and operated using the same decoupled electrolyte design (Figure 3.1b and Figure 3.4). In this design, a starting mixed solution of NH_4I_3 and NH_4Cl is used as the catholyte while a sole NH_4Cl solution is used as the anolyte. H-GF and zinc plate are adopted as the cathode and anode respectively, which are also separated by a N117. In this configuration, the battery is assembled in a charged state. As a result, during the initial discharge operation, the NH_4I_3 solution flows through the H-GF cathode, and the system is respectfully denoted as AC-ZI_3FB. During discharging, zinc releases electrons to the external circuit and is oxidized into soluble Zn species ($[Zn(NH_3)_xCl_y]^{2-y}$) in the presence of NH_4Cl [92]. At the same time, the I_3^- and I_2Cl^- in the catholyte solution accept electrons and are reduced into I^- and Cl^- at the electrolyte-electrode interface of the H-GF cathode (Eq. 3-6). Then, during charging of AC-ZI_3FB system, the reverse reactions in (Eqs. 3-4 - 3-6) would occur similarly at the anode and cathode. Such operational flexibility is enabled by the decoupling configuration with differentiated anolyte and catholyte, which allows

either oxidative (NH_4I_3) or reductive (NH_4I) operations to utilize the I_3^-/I^- redox couple in the starting catholyte. The effect of starting catholyte will be evaluated by electrochemical means in the AC-ZIFB (NH_4I) and AC-ZI_3FB (NH_4I_3) systems.

3.3.2 Electrochemical Performance of AC-ZIFB

The performance evaluation of ZIFB design was conducted via full charge and discharge test under constant current density of 20 mA cm^{-2} with cut-off voltages of 1.6 V and 0.6 V, respectively (Figure 3.6a). The AC-ZIFB catholyte was a mixture of 2.5 M NH_4I and 1.25 M NH_4Cl (corresponding to a ratio of supporting electrolyte to the electrochemically active electrolyte of 2:1). The AC-ZIFB anolyte was 1.25 M $ZnCl_2$ with the addition of 1.25 M NH_4Cl, same concentration used in catholyte. The conventional ZIFB with 1.25 M ZnI_2 solution as both anolyte and catholyte was also evaluated. It is clearly observed from Figure 3.6a that AC-ZIFB showed approximately 10% enhancement in volumetric capacity relative to conventional ZIFB, even with the same concentration of the iodide ion in both systems (i.e. iodide concentration in AC-ZIFB catholyte equals iodide concentration in both ZIFB electrolyte). The improved volumetric capacity can be attributed to the additional formation of I_2Cl^- in the AC-ZIFB catholyte, thus providing further capacity [17]. Moreover, it is worth noting that the average charge voltages of AC-ZIFB was lower than conventional ZIFB, and the average discharge voltages of AC-ZIFB was higher (See Table 3.2 for details). These low overpotentials experienced during both charging and discharging imply faster reaction kinetics at both the anode and cathode, as well as improved electrolyte and membrane conductivity of AC-ZIFB.

A galvanostatic cycling test with charge/discharge currents of 20 mA cm^{-2} was further conducted for both the AC-ZIFB and conventional ZIFB with 50% SOC. The Coulombic efficiency (CE) of AC-ZIFB was maintained at 99% for 100 cycles while the conventional ZIFB only showed a CE of 90% for around 50 cycles (Figure 3.6b). The high CE can be mainly attributed to the high selectivity of cations

that migrate through the CEM. The anionic nature of the I^-, I_3^-, and I_2Cl^- species intrinsically prevented their migration through the CEM due to electrostatic repulsion. Despite the similarity to vanadium redox flow batteries [93] regarding the fact that all cations can migrate through the CEM, the ability to form zinc complex ions in the AC-ZIFB strongly limited the Zn^{2+} migration and thus improved the ion selectivity through the CEM.

Table 3.2. Summary of ZIFB and AC-ZIFB cell performance in Figure 3.6a.

System	Average charge voltage (V)	Average discharge voltage (V)	Volumetric discharge capacity (Ah L^{-1})	Volumetric energy density (Wh L^{-1})
ZIFB	1.45	1.07	38.0	40.7
AC-ZIFB	1.41	1.17	41.1	48.1

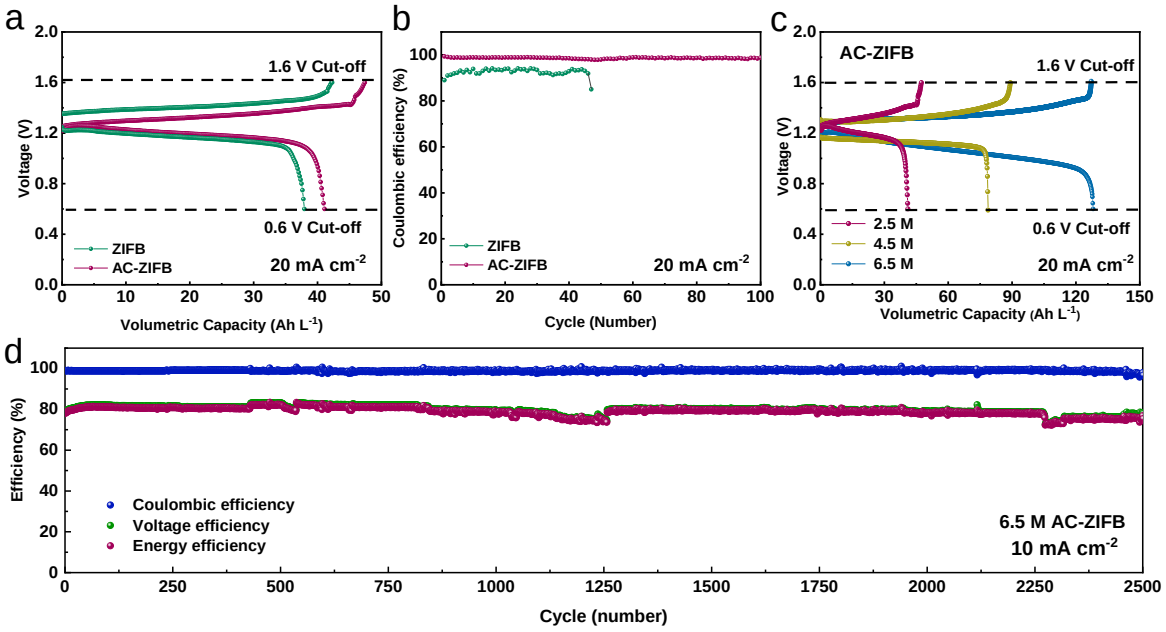

Figure 3.6. Electrochemical performance of the ZIFB and AC-ZIFB systems. a) A representative cell voltage profile and b) associated cycling performance of ZIFB and AC-ZIFB with 2.5 M I^- catholyte composition (1.25 M ZnI_2 and 2.5 M NH_4I/1.25 M NH_4Cl for ZIFBs and AC-ZIFBs, respectively) under current density of 20 mA.cm^{-2}.c) Voltage profiles of the AC-ZIFB with different I^- concentration in catholyte at current density of 20 mA.cm^{-2}. d) The long-term stability of an AC-ZIFB test cell with 6.5 M I^- (6.5 M NH_4I/1.5 M NH_4Cl) catholyte composition under the current density of 10 mA.cm^{-2}.

To further increase the volumetric capacity of the AC-ZIFB, higher concentration electrolytes were prepared and circulated in the cell. The composition of electrolytes with I^- concentrations of 2.5 M, 4.5 M and 6.5 M in the catholyte and corresponding anolytes are listed in Table 3.3. According to Figure 3.6c and Table 3.4, the obtained discharge volumetric capacity and energy density of the AC-ZIFB operated at a current density of 20 mA cm^{-2} increased from 41.0 Ah L^{-1} and 48.0 Wh L^{-1} (2.5 M I^-) to 128.0 Ah L^{-1} and 137.0 Wh L^{-1} (6.5 M I^-), respectively. It must be pointed out that the discharge volumetric capacity obtained in 6.5 M NH_4I exceeded the theoretical volumetric capacity for 6.5 M I^- (116.1 Ah L^{-1}, Appendix 2), further indicating the extra capacity contribution from I_2Cl^- formed during charging. As a function of electrolyte concentration, the average charge and discharge voltages both decreased while the VE maintained a nearly constant value of 85% at 20 mA cm^{-2} current density. This indicates the high reversibility of anodic and cathodic reactions in this NH_4Cl supported electrolyte at a wide range of active component concentrations.

Table 3.3. The catholyte and anolyte composition of AC-ZIFB test cells in Figure 3.6c.

Concentration	Catholyte Solution	Anolyte Solution
	NH_4I / NH_4Cl	**$ZnCl_2$ / NH_4Cl**
2.5 M I^-	2.5 M / 1.25 M	1.25 M / 1.25 M
4.5 M I^-	4.5 M / 2.25 M	2.25 M / 2.25 M
6.5 M I^-	6.5 M / 1.5 M	3.25 M / 1.5 M

Table 3.4. Summary of AC-ZIFB cell performance for different concentrations in Figure 3.6c, operated at 20 mA.cm^{-2} current density.

Catholyte composition	Average charge voltage (V)	Average discharge voltage (V)	Volumetric discharge capacity (Ah L^{-1})	Volumetric energy density (Wh L^{-1})
2.5 M I$^-$	1.41	1.17	41.1	48.0
4.5 M I$^-$	1.32	1.13	78.8	89.0
6.5 M I$^-$	1.34	1.07	128.0	137.0

With prolonged galvanostatic cycling tests at 20 mA cm^{-2} and 20% SOCs, AC-ZIFB with 2.5 M I$^-$showed exceptionally stable performance for 1,200 cycles, maintaining CE at ~99%, VE at ~89%, and EE at ~88% (Figure 3.7). It outperformed the cyclability of conventional ZIFB systems (Table 3.5) [19]. With elevated I$^-$ concentration of 6.5 M and constant current density at 10 mA cm^{-2}, AC-ZIFB demonstrated the highest reported cyclability of a ZIFB system to date of 2,500 cycles (Figure 3.6d and Table 3.5). Moreover, both average VE and EE were maintained at approximately 78%, with ~99% CE. Such remarkable cyclability obtained without modification and development of a specialized membrane further indicate the highly advantageous solution chemistry within the NH_4Cl supported electrolyte.

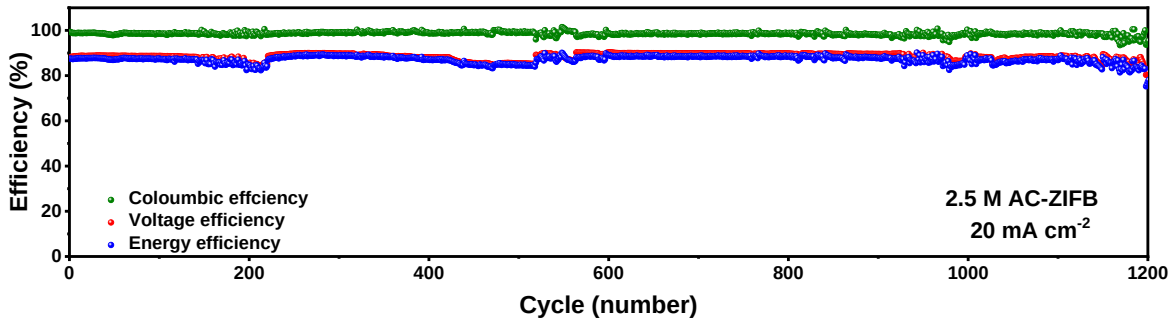

Figure 3.7. The long-term stability of an AC-ZIFBs test cell with 2.5M I$^-$ (2.5 M NH_4I/1.25 M NH_4Cl) catholyte composition at the current density of 20 mA.cm^{-2}.

Table 3.5. Comparison of cyclability of zinc-iodine based redox flow batteries.

System	Con. (M)	Cycle life	Membrane / electrode	Current Density (mA cm^{-2})	SOC (%)	Ref
ZIFB	3.5	39	N117/GF	10	NA	[19]
ZIFB	2.5	50	N117/GF-MOF	30	NA	[83]
ZIFB	3.0	20	-	5	NA	[18]
ZIFB	6.0	500	PE/GF	80	NA	[94]
ZIFB	5.0	1,000	PE/GF	80	NA	[15]
ZI/Br RFB	3.5	50	N117/GF	10	50	[17]
Alkaline ZIFB	6.0	70	N117/GF	20	NA	[16]
AC-ZIFB	2.5	1,200	N117/GF	20	20	This work
AC-ZIFB	6.5	2,500	N117/GF	10	20	This work
AC-ZIFB	5	1,100	PE/GF	80	20	This work
AC-ZI_3FB	2.6	1,500	N117/GF	10	20	This work

3.3.3 Electrochemical Performance of AC-ZI_3FB

The ZI_3FB design is initiated by discharging, where zinc ions stripped from the zinc plate (anode) are dissolved in the weakly acidic NH_4Cl solution in the anolyte. Again, the I_3^- and I_2Cl^- in the prepared catholyte solution are reduced to I^- and Cl^- ions at the surface of H-GF (cathode). To investigate the effect of supporting NH_4Cl on the performance of ZI_3FB arrangement, catholytes were prepared by dissolving the same molar amount of iodine in the sole NH_4I solution and NH_4I-NH_4Cl (1:1.5 ratio) mixed solution. These catholyte solutions are coupled with NH_4Cl anolyte, as listed in Table 3.6 and

assembled into flow cells. The RFB system with supporting NH_4Cl in the catholyte is denoted as AC-ZI_3FB and by comparison, system with sole NH_4I_3 as catholyte is denoted as ZI_3FB. Clearly, the charge/discharge curves obtained at constant current density of 10 mA cm^{-2} and 1 M I_3^- catholyte composition in Figure 3.8a showed an enhanced discharge volumetric capacity for AC-ZI_3FB compared to that of ZI_3FB (51.7 vs. 41.3 Ah L^{-1}) (Table 3.7). The 25% improvement can be attributed to the increased solubility of iodine via the formation of the extra I_2Cl^- ions and hence the observed additional capacity [17]**.**

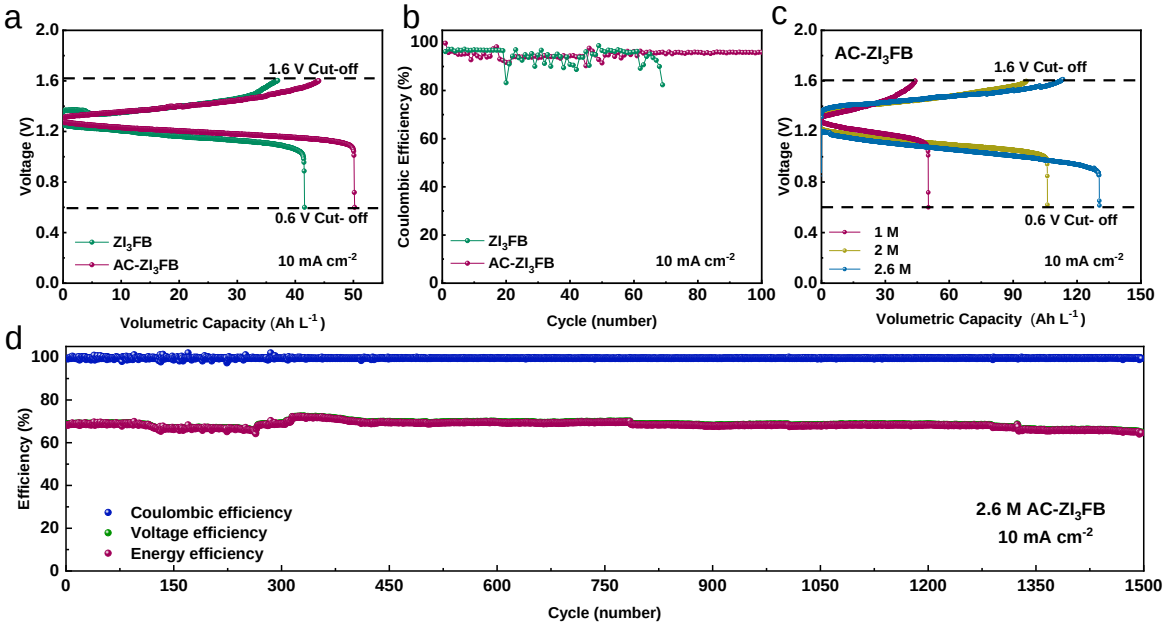

Figure 3.8. Electrochemical performance of ZI_3FBs and AC-ZI_3FBs. a) A representative cell voltage profile and b) associated cycling performance of ZI_3FBs and AC-ZI_3FBs with 1 M I_3^- catholyte composition (1 M NH_4I_3 and 1 M NH_4I_3 /1.5 M NH_4Cl for ZI_3FBs and AC-ZI_3FBs, respectively) under current density of 10 mA.cm^{-2}. c) Voltage profile of the ZI_3FBs with different I_3^- concentration in catholyte at current density of 10 mA.cm^{-2}. d) The long-term stability of an AC-ZI_3FBs test cell with 2.6 M I_3^- (2.6 M NH_4I_3 /5.2 M NH_4Cl) catholyte composition under the current density of 10 mA.cm^{-2}

Table 3.6. Catholyte and anolyte composition of ZI_3FB and AC-ZI_3FB test cells.

System	Catholyte Solution	Anolyte Solution
	NH_4I_3 / NH_4Cl	NH_4Cl / NH_4Cl *shown as total concentration
ZI_3FB	1 M / 0 M	1 M
AC-ZI_3FB	1 M / 1.5 M	2.5 M

Table 3.7. Electrochemical performance summary of ZI_3FBs and AC-ZI_3FBs test cells with 1M electrolyte composition, at 10 mA.cm^{-2} current density, single charge/discharge test.

System	Average charge voltage (V)	Average discharge voltage (V)	Discharge capacity (Ah L^{-1})	Volumetric energy density (Wh L^{-1})
ZI_3FB	1.40	1.16	41.3	47.9
AC-ZI_3FB	1.42	1.19	51.7	61.5

Galvanostatic cycling tests of AC-ZI_3FB and ZI_3FB with 1 M I_3^- were also conducted at constant current density of 10 mA cm^{-2}. The CEs for each system as function of cycling number are compared in Figure 3.8b. The ZI_3FB system could only maintain a high CE of 97% for the first 20 cycles, followed by significant fluctuations over the next 50 cycles and a rapid drop to 80% after 70 cycles. On the contrary, AC-ZI_3FB continuously maintained a high CE of 96% for 100 cycles, showing significant improvement in cell performance brought by the addition of NH_4Cl supporting electrolyte. In particular, the concentration of NH_4Cl in the anolyte was found to tune the morphology of deposited zinc on the zinc plate anode after cycling. The dendrite structure went from a non-uniform assembly of plate-like crystals with exposed rich sharp edges and facets in the anolyte of ZI_3FB (1 M NH_4Cl) (Figure 3.9a) to flat coherent and dense layers in the anolyte of AC-ZI_3FB (1 M NH_4Cl + 1.5 M supporting NH_4Cl) (Figure 3.9b). The preferred morphology resulting from NH_4Cl supporting

electrolyte hindered the growth and proliferation of zinc dendrites, prolonging the cyclability of the AC-ZI_3FB system.

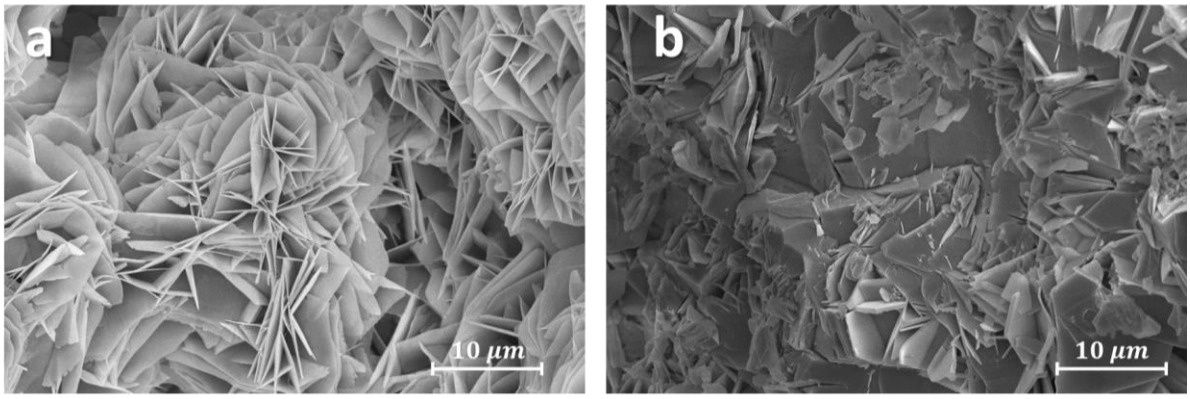

Figure 3.9. SEM images of zinc dendrite morphology at anode surface of a) ZI_3FBs test cell with 1 M NH_4I_3 catholyte composition and b) AC-ZI_3FBs test cell with 1 M NH_4I_3 /1.5 M NH_4Cl catholyte composition.

The charge-discharge curves of AC-ZI_3FB at constant current density of 10 mA cm^{-2} for different anolyte and catholyte concentrations (see Table 3.8 for composition details) are demonstrated in Figure 3.8c. High practical volumetric discharge capacities and energy densities were successfully obtained (fully charged), ranging from 51.8 Ah L^{-1} and 61.7 Wh L^{-1} (1.0 M I_3^- in catholyte) to 130.4 Ah L^{-1} and 136.9 Wh L^{-1} (2.6 M I_3^- in catholyte), respectively (Table 3.9). According to the calculation in Appendix 1 and Table 3.10, the average discharge molar capacity of AC-ZI_3FB (51.7 Ah mol^{-1}) was approximately 2.8 times and 1.5 times higher than that of AC-ZIFB (18.6 Ah mol^{-1}) and a conventional ZIFB reported in the literature (35.1 Ah mol^{-1}). This not only proves the concept of high molar capacity design for AC-ZI_3FB, but also demonstrates the highest electron-atom economy for ZIFB systems.

Table 3.8. Electrolyte composition of AC-ZI$_3$FB test cells in Figure 3.8c.

concentration	Catholyte Solution	Anolyte Solution
	NH_4I_3 / NH_4Cl	NH_4Cl / NH_4Cl *shown as total concentration
1 M I_3^-	1 M / 1.5 M	2.5 M
2 M I_3^-	2 M / 3 M	5 M
2.6 M I_3^-	2.6 M / 3.9 M	6.5 M

Table 3.9. Electrochemical performance summary of AC-ZI$_3$FB test cells with different electrolyte compositions in Figure 3.8c, 10 mA.cm^{-2} current density, single charge/discharge test.

Catholyte composition	Average charge voltage (V)	Average discharge voltage (V)	Discharge capacity (Ah L^{-1})	Volumetric energy density (Wh L^{-1})
1 M I_3^-	1.42	1.19	51.8	61.6
2 M I_3^-	1.46	1.11	106.0	117.7
2.6 M I_3^-	1.48	1.05	130.4	136.9

Table 3.10. Molar capacity of ZIFB, AC-ZIFB, and AC-ZI$_3$FB systems.

	ZIFBs			AC-ZIFBs			AC-ZI$_3$FBs		
Catholyte concentration	**1.5 M**	**3.5 M**	**5 M**	**2.5 M**	**4.5 M**	**6.5 M**	**1 M**	**2 M**	**2.6 M**
C_v (Ah L^{-1})	53.0 [19]	124.0 [19]	160.0 [19]	41.1	78.8	128.0	51.8	106.0	130.4
C_n (Ah mol^{-1})	35.3	35.4	32.0	16.4	17.5	19.7	51.8	53.0	50.2
Average of C_n (Ah mol^{-1})		34.2			17.9			51.7	

Correspondingly to AC-ZIFB, the AC-ZI_3FB system with high-concentration catholyte (2.6 M I_3^-) was assembled and subjected to a long-term galvanostatic cycling test at a current density of 10 mA cm^{-2} and 20% SOCs. As presented in Figure 3.8d, AC-ZI_3FB continuously underwent stable charging and discharging for 1,500 cycles with a CE maintained as high as 99.5% and an average VE and EE of approximately 70%. The excellent cyclability also ranks AC-ZI_3FB as one of the most stable ZIFB systems reported to date (Table 3.5). The outstanding cyclability of both the AC-ZIFB and AC-ZI_3FB systems, independent of the initial operation (discharge or charge), indicates the unique and versatile solution chemistry of NH_4Cl-supported anolyte and catholyte in both systems.

3.3.4 Anolyte Investigation

To gain a greater understanding of the improved cyclability and CE imparted by the NH_4Cl -supported flow batteries, the solution chemistry of NH_4Cl-supported anolyte was firstly investigated by a half-cell study with a glassy carbon electrode (GCE) as the working electrode in various electrolyte solutions. Cyclic voltammetry (CV) curves were obtained using 2 M $ZnCl_2$ and 2 M $ZnCl_2$ + 2 M NH_4Cl anolyte solutions at a scan rate of 20 mV s^{-1}. According to the CV curves in Figure 3.10a, zinc metal began depositing at the surface of the GCE (reduction reaction) below approximately -1.1 V (vs. Ag/AgCl) and a nucleation loop was produced at the end of the cathodic scan. With the reverse scan, an anodic peak, representing Zn^{2+} stripping from anode (oxidation reaction), appeared at approximately –1.0 V (vs. Ag/AgCl). The data extracted from the CVs (Table 3.11) indicated that with the introduction of supporting NH_4Cl, the nucleation overpotential (NOP) of zinc decreased from 48.6 mV in $ZnCl_2$ solution to 13.3 mV in the supported electrolyte solution of NH_4Cl and $ZnCl_2$. This decrease in overpotential indicates the improved reversibility of the zinc plating and dissolution reactions, which subsequently benefits the VE for both AC-ZIFB and AC-ZI_3FB. In addition, from the CV tests, both $ZnCl_2$ and $ZnCl_2$-NH_4Cl solutions showed approximately 100% Coulombic efficiency for zinc

deposition/dissolution, indicating no negative effects of NH_4Cl on the CE of the zinc redox reaction. Therefore, the NH_4Cl-supported anolyte solution displays excellent properties in terms of both lowering the cathodic polarization and maintaining high CE.

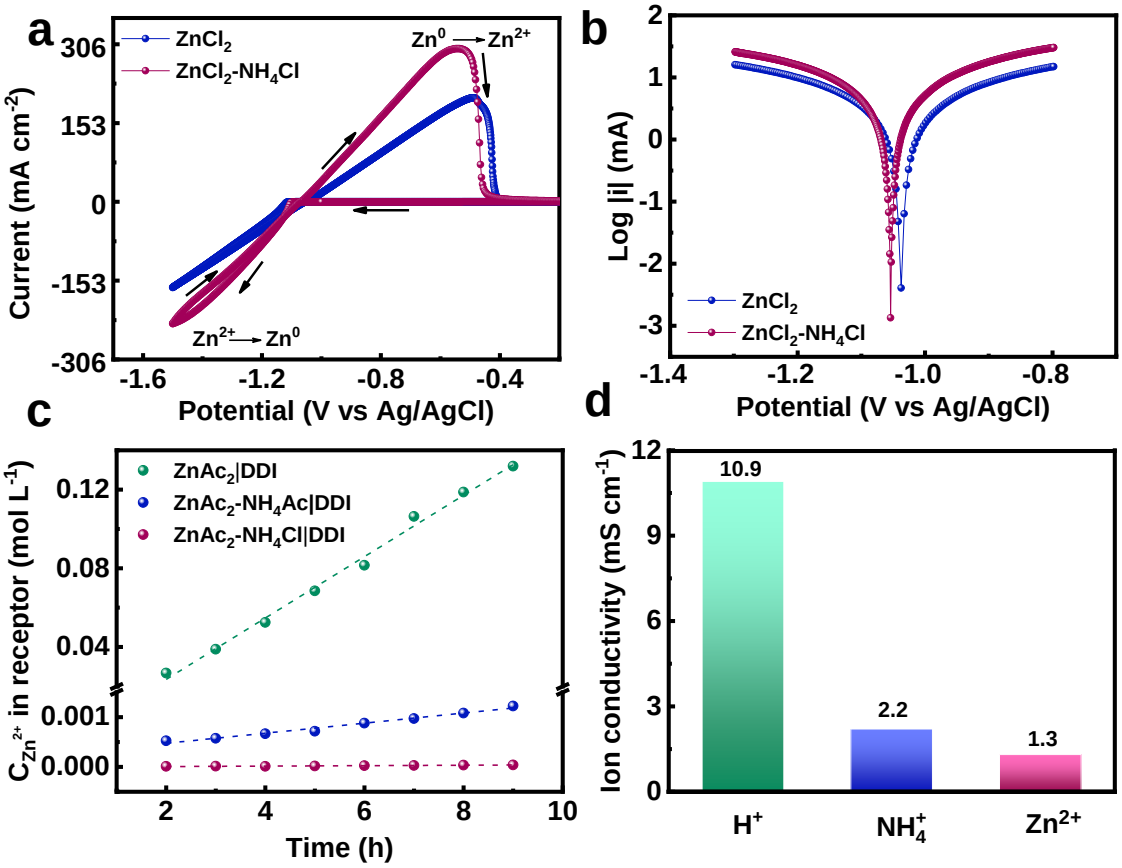

Figure 3.10. Investigation of NH_4-based anolyte. a) Cyclic voltammetry of 2 M $ZnCl_2$ and 2 M $ZnCl_2$ / 2 M NH_4Cl anolyte on a glassy carbon electrode at the scan rate of 20 mV s^{-1}. b) The plots of logarithm of current versus potential of 2 M $ZnCl_2$ and 2 M $ZnCl_2$ / 2 M NH_4Cl mixed solution on a glassy carbon electrode at a scan rate of 2 mV s^{-1}. c) Zn^{2+}concentration change in receptor reservoir of the permeation measuring device versus diffusion time with 1 M $ZnAc_2$, 1 M $ZnAc_2$ /1 M NH_4Cl, and , 1 M $ZnAc_2$ /1 M NH_4Ac mixed solutions in feeding reservoir. d) Through-plane ion conductivity of different ion-form Nafion 117 membrane at room temperature and 100% humidity condition.

Table 3.11. Summary of electrochemical investigation of NH_4Cl-supported anolyte obtained from CV.

Anolyte composition	E^1_{co} (V vs Ag/AgCl)	E^2_{nu} (V vs Ag/AgCl)	NOP[3] (mV vs Ag/AgCl)	Q_{an} [4] (mA s)	Q_{cath}[5] (mA s)	Columbic efficiency (%)
2 M $ZnCl_2$	-1.101	-1.052	48.6	614.94	614.84	99.98%
2 M $ZnCl_2$/2 M NH_4Cl	-1.084	-1.071	13.3	1004.5	1003.65	99.92

The influence of NH_4Cl supporting electrolyte on the Zn^{2+}/Zn kinetics were also investigated by Tafel plot analysis (Figure 3.10b). According to the extracted data, summarized in Table 3.12, no significant changes were found for the Tafel slopes in the cathodic and anodic regions in the two electrolyte systems. This indicated that the addition of NH_4Cl supporting electrolyte had negligible effects on the reaction mechanism of zinc deposition and dissolution. However, the exchange current density (i_0) in the supported electrolyte solution of NH_4Cl and $ZnCl_2$ almost doubled in comparison to the value obtained in the sole $ZnCl_2$ solution. This can be partially attributed to the bridge effect of chloride ions, where Cl^- adsorbed on the surface of the GCE facilitates charge transfer between the metal cation and electrode surface [56,95,96].

Table 3.12. Summary of electrochemical investigation of NH_4Cl-supported anolyte obtained from Tafel plots.

Anolyte Composition	E_{OCP} (V)	β_c (mV decade $^{-1}$)	β_a (mV decade $^{-1}$)	i_0 (mA cm^{-2})
2 M $ZnCl_2$	-1.039	247	258	11.84
2 M $ZnCl_2$ /2 M NH_4Cl	-1.053	239	230	20.16

Due to the separation of Zn^{2+} and I^- in the electrolytes, the migration of Zn^{2+} from the anolyte to the catholyte through the CEM would cause a gradual loss of capacity and decrease the CE during long-

term cycling. However, as displayed in Figure 3.6d and Figure 3.8d, surprisingly excellent cyclability with stable performance was obtained in both the AC-ZIFB and AC-ZI_3FB systems; this suggests low Zn^{2+} permeability in the unique solution chemistry of the NH_4Cl supporting anolyte. As illustrated in Figure 3.5, a permeability test was conducted in an H-cell where the CEM (N117) used in both RFB systems was sandwiched between two compartments, containing DDI water in the receptor compartment and a feed solution in the other. The concentration of Zn^{2+} in the receptor compartment increased linearly with respect to diffusion time (Figure 3.10c), with the Zn^{2+} permeability calculated accordingly in Table 3.13. To examine any species interaction of Zn^{2+}, three Zn-containing feed solutions were tested: zinc acetate ($ZnAc_2$), $ZnAc_2$-NH_4Ac and $ZnAc_2$-NH_4Cl. Apparently, in the absence of NH_4^+, Zn^{2+} in the 1 M $ZnAc_2$ feed solution migrated freely through the CEM to DDI water in the receptor compartment, leading to a rapid increase of Zn^{2+} concentration (green dots in Figure 3.10c) and represents high permeability. Surprisingly, when an equimolar concentration of NH_4^+ was introduced with Zn^{2+} in the 1 M $ZnAc_2$-1 M NH_4Ac feed solution, the permeation of Zn^{2+} through the CEM was drastically inhibited (blue dots in Figure 3.10c). The permeability of Zn^{2+} was reduced by approximately 15 times in the presence of NH_4^+ (Table 3.13), indicating the dominant permeation of NH_4^+ over Zn^{2+} at an equimolar concentration. The reason for this likely lies in the inherent electronic differences between Zn^{2+} and NH_4^+ ions. The monovalent NH_4^+ ion tends to a have weaker interaction with the negatively-charged sulfonic groups in the CEM compared to that of the divalent Zn^{2+} ion [97], promoting the migration of NH_4^+. Moreover, in theory, to maintain charge balance, the monovalent NH_4^+ concentration is likely to be double the amount in the CEM compared to that of the divalent Zn^{2+} ion, which further promotes the permeation of NH_4^+ over Zn^{2+}. In addition, the smaller hydrated radius of NH_4^+ versus that of Zn^{2+} further improves the CEM selectivity of NH_4^+ over Zn^{2+} [98]. As a result, permeability of Zn^{2+} ions through the CEM is effectively less preferred.

When Cl^- was also introduced into the feed solution (1 M $ZnAc_2$-1 M NH_4Cl), the permeation of Zn^{2+} was further inhibited, showing a Zn^{2+} permeability three magnitudes lower than the 1 M $ZnAc_2$-1 M NH_4Ac mixture (red dots in Figure 3.10c, and Table 3.13). Thus, it is believed that Zn^{2+} interacts with both NH_4^+ and Cl^- to form large complex ions and possible small protons/hydroniums [92] according to the following reaction:

$$\mathbf{Zn^{2+} + x\ NH_4^+ + y\ Cl^- \leftrightarrow [Zn(NH_3)_x Cl_y]^{2-y} + x\ H^+} \qquad \mathbf{(3\text{-}7)}$$

The resulting large Zn-complex ions cannot easily migrate through the CEM due to size exclusion. In this case, Zn^{2+} is not only less probable to migrate through the CEM, but it is also hindered from doing so, thus further decreasing its permeability. At the same time, the generated protons/hydroniums can travel through the CEM even faster than NH_4^+ under the applied electric field in the RFB cells. The through-plane ion conductivities of different ions through fully hydrated CEMs at room temperature are summarized in Figure 3.10d. The ion conductivity of H^+-form CEM is approximately one order of magnitude higher than that of NH_4^+-form and Zn^{2+}-form CEMs. It is also noteworthy that the ion conductivity of NH_4^+-form CEM is nearly two times higher than that of Zn^{2+}-form CEM. Overall, the addition of NH_4Cl in the anolyte not only successfully exchanges the dominant charge carrier migrating through the CEM from slow larger-sized divalent Zn^{2+} ions to fast smaller-sized monovalent ions (NH_4^+, H^+), but it also beneficially further enlarges the size of Zn-based ions via coordination to prohibit the permeation of Zn ion species. Therefore, the solution chemistry of NH_4Cl supporting anolyte guarantees the high CE and cyclability of both AC-ZIFB and AC-ZI_3FB systems.

Table 3.13. Comparison of Zn^{2+} ion permeability through Nafion 117 membrane with different feeding solutions.

System	$ZnAc_2$|DDI	$ZnAc_2$-NH_4Ac|DDI	$ZnAc_2$-NH_4Cl| DDI
Zn^{2+} Permeability coefficient ($cm^2\ min^{-1}$)	1.88×10^{-4}	1.22×10^{-5}	3.78×10^{-8}

3.3.5 Catholyte Investigation

The solution chemistry of the NH_4-based catholyte was investigated using both experimental and theoretical approaches. To isolate and understand the functionality of supplementary Cl^-, the catholyte solutions used in ZI_3FB and AC-ZI_3FB systems, i.e. $NH_4I_3$and NH_4I_3-NH_4Cl respectively, were studied by Raman spectroscopy. As illustrated in Figure 3.11a, two distinctive peaks at 110 and 157 cm^{-1} appeared in the spectra for both catholytes. The former peak is assigned to the symmetric stretch of linear I_3^- while the latter is ascribed to the outer symmetric stretch of V-shaped polyiodide. [19] With the addition of NH_4Cl to NH_4I_3, a new band appeared at 227 cm^{-1}, which represents the formation of the I_2Cl^- complex in the catholyte.

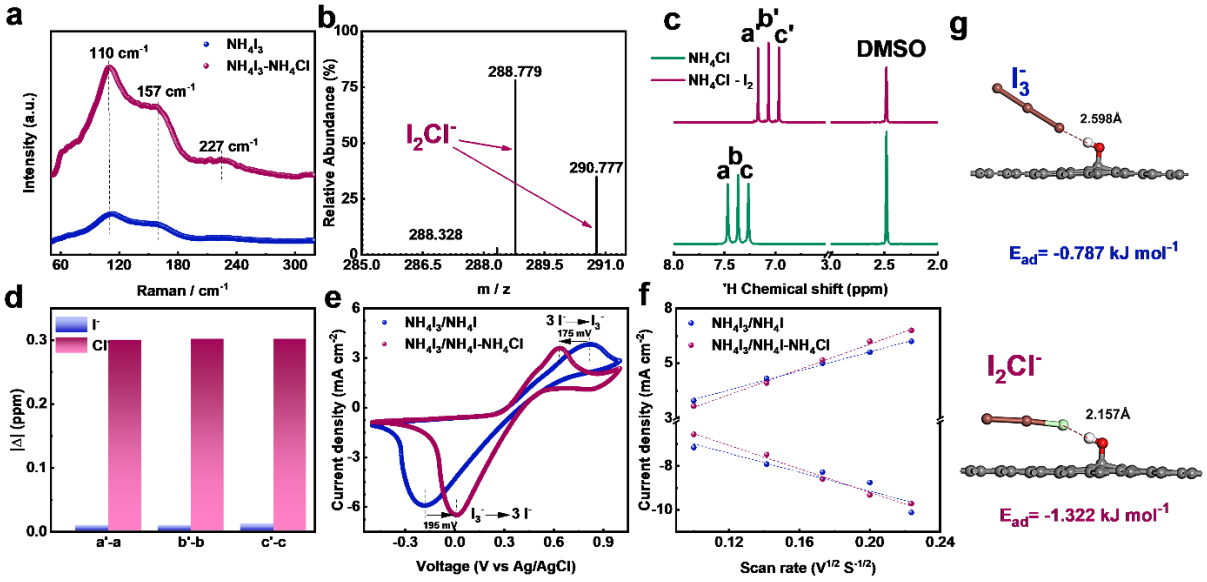

Figure 3.11. Investigation of NH_4-based catholyte, red and blue color represent electrolyte composition with and without NH_4Cl supporting electrolyte, respectively. a) Raman spectra of 1 M NH_4I_3- NH_4I and 1 M NH_4I_3- NH_4I -1.5 M NH_4Cl catholytes. b) Electrospray ionization mass spectrometry (ESI-MS) spectrum of 10 µM NH_4I_3-15 µM NH_4Cl catholyte, c) 'H NMR spectroscopy of 1 M NH_4Cl solution with and without 1 M I_2. d) Change in ^1H Chemical shift (ppm) of a', b' and c' peaks in NH_4I and NH_4Cl catholytes with and without I_2. e) Cyclic voltammetry of 10 mM NH_4I_3- NH_4I and 10 mM (NH_4I_3- NH_4I)- 15 mM NH_4Cl catholytes on a glassy carbon electrode at a scanning rate of 20 mV s^{-1}. f) Plot of current versus scan rate for oxidation and reduction of I_3^-. g) DFT-optimized molecular structure of the I_3^-, and I_2Cl^- anions at the surface of H-GF cathode.

The existence of I_2Cl^- is further proven by the split m/z (mass/charge number) peaks of the I_2Cl^- ion cluster at 288.78 and 290.78 in the electrospray ionization mass spectrometry (ESI-MS) spectrum of the NH_4I_3-NH_4Cl catholyte solution presented in Figure 3.11b. It is noted that the intensity of the I_2Cl^- cluster peaks was found to be 10% of the I^- cluster peaks in the full ESI-MS spectrum in Figure 3.12, indicating considerable amount of I_2Cl^- species in the NH_4Cl -supported catholyte solution.

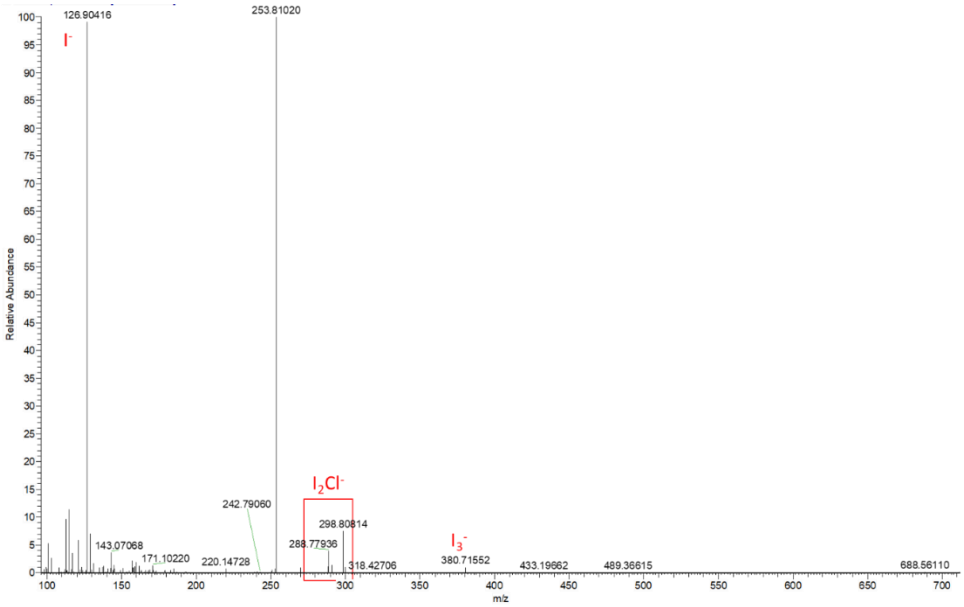

Figure 3.12. The full Electrospray ionization mass spectrometry (ESI-MS) spectrum of 10 mM NH_4I_3-10 mM NH_4Cl catholyte.

Considering the abundance of NH_4^+ in the catholyte, its influence on the formation of I_2X^- (X= I and Cl) species was further investigated by proton nuclear magnetic resonance (^{1}H NMR) spectroscopy. As presented in Figure 3.11c, the typical triplet peaks for NH_4^+ appear in the ^{1}H NMR spectra of the NH_4Cl solution before and after the introduction of iodine molecules. The significant upfield shift of the triplet in the presence of iodine molecules is attributed to the increased shielding effects of iodine and formed I_2Cl^- on NH_4^+. Similarly, the same upfield shift phenomenon was also observed for the NH_4I solution after the introduction of additional I_2 (Figure 3.13a). The observed differences in chemical shift of the

triplet are compared in Figure 3.11d, and evidently shows that the NH_4Cl solution demonstrated a dramatically higher upfield shift compared to the NH_4I solution after the introduction of iodine. This implies a much stronger NH_4^+ shielding effect of the formed I_2Cl^- as opposed to I_3^-. Furthermore, as shown in the ^1H NMR spectra of iodine-added NH_4X solutions (Figure 3.13), the triplet peaks of NH_4Cl-I_2 were located downfield upon addition of I_2 as opposed to the triplet peaks of NH_4I-I_2 which barely changed. This indicates the stronger hydrogen bond formed between NH_4^+ and I_2Cl^- as opposed to the I_3^- species. Overall, these results show that NH_4^+ promotes the formation of I_2Cl^- and further stabilizes it via the strong interaction between the respective species.

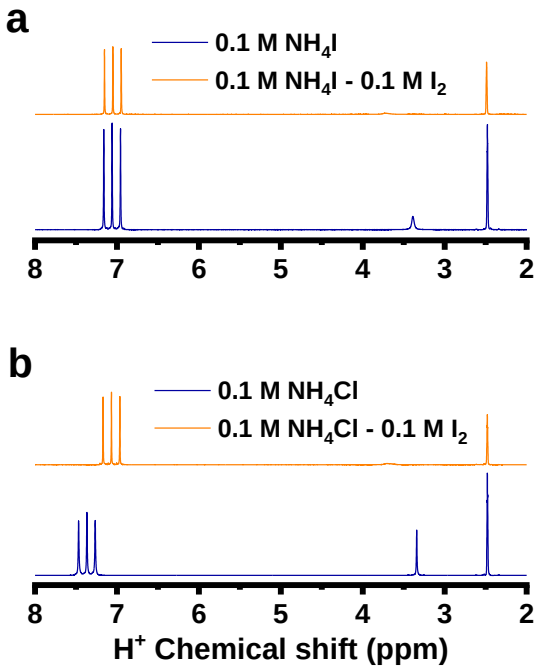

Figure 3.13. Full length NMR spectroscopy of a) 0.1 M NH_4I and 0.1 M NH_4I/0.1 M I_2 mixed solution, and b) 0.1 M NH_4Cl, 0.1 M NH_4Cl/0.1 M I_2 catholyte.

To evaluate the effect of added NH_4Cl on the catholyte redox reaction kinetics, half-cell studies were performed in mixed I_3^-/I^- electrolyte composition. The obtained CV curves for 10 mM (NH_4I_3/NH_4I) and 10 mM (NH_4I_3/NH_4I)-15 mM NH_4Cl solutions displayed in Figure 3.11e show two distinctive

peaks on each curve representing the redox reactions of the I_3^-/I^- redox couple. It is evident that the introduction of NH_4Cl as supporting electrolyte significantly decreased the overpotentials of both iodide oxidation and triiodide reduction by 175 and 195 mV, respectively. As a result, the total anodic and cathodic peak potential difference (ΔE) was reduced by 370 mV in the presence of NH_4Cl (Table 3.14). This not only suggests the improved reversibility of the I_3^-/I^- redox reaction brought about by the supporting NH_4Cl, but it also supports the observed high VE in both AC-ZIFB and AC-ZI_3FB.

Table 3.14. Anodic and cathodic peak potential of 10 mM (NH_4I_3- NH_4I) and 10 mM (NH_4I_3- NH_4I)-15 mM NH_4Cl catholyte obtained from CV curves.

Catholyte composition	E_{pa} [1] (V vs Ag/AgCl)	E_{pc} [2] (V vs Ag/AgCl)	ΔE (V)
NH_4I_3	0.814	-0.186	1
NH_4I_3- NH_4Cl	0.639	0.009	0.63

1 Anodic Peak Potential

2 Cathodic Peak Potential

According to Figure 3.11f and Figure 3.14, the oxidation and reduction peak currents at different scan rates showed a linear dependence on the square root of the scan rate, implying that the I_3^-/I^- redox reaction rate was limited by diffusion in both solutions. The calculated diffusion coefficients of I^-(cathodic peak) and I_3^- (anodic peak) based on the Randless-Sevcik equation in Table 3.15 showed an increase of 81% and 77% in the presence of NH_4Cl, respectively.

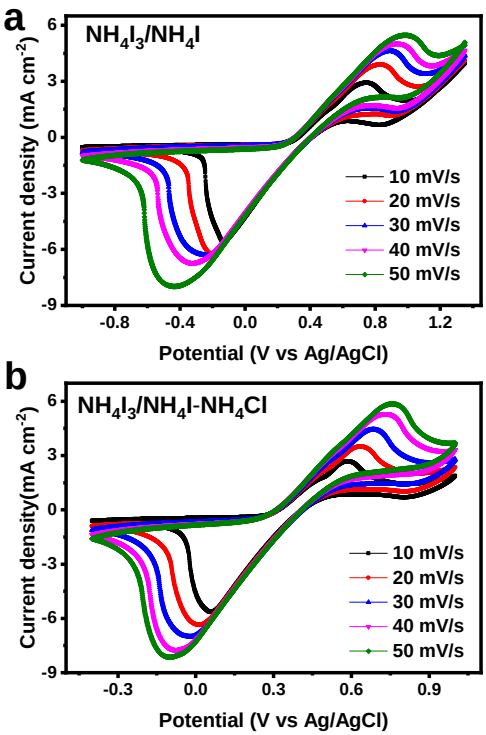

Figure 3.14. Cyclic Voltammetry showing effect of NH_4Cl : a) 10 mM (NH_4I_3- NH_4I), and b) 10 mM (NH_4I_3- NH_4I)-15 mM NH_4Cl catholytes at different scan rates.

Table 3.15. Comparison of diffusion coefficients for I^- and I_3^- ions in different catholytes obtained by the Randles-Sevcik method (Data extracted from Figure 3.14).

Catholyte composition	D_{I^-}		$D_{I_3^-}$	
	Absolut value (10^{-5} cm s^{-1})	Improvement * (%)	Absolut value (10^{-5} cm s^{-1})	Improvement * (%)
NH_4I_3	1.31	-	0.85	-
NH_4I_3- NH_4Cl	2.37	81%	1.50	77%

* Improvement (%)$= \frac{D_{NH_4I_3/NH_4Cl} - D_{NH_4I_3}}{D_{NH_4I_3}}$

The enhancement of diffusion coefficients in the presence of additional NH_4Cl was also validated by the calculation through Levich equation and linear sweep voltammetry curves at different rotation rates (Figure 3.15 and Table 3.16). Thus, the kinetics of iodide oxidation and triiodide reduction were

significantly enhanced in the NH_4Cl-supported catholyte via the enhancement of diffusion coefficients for the I_3^-/I^- species.

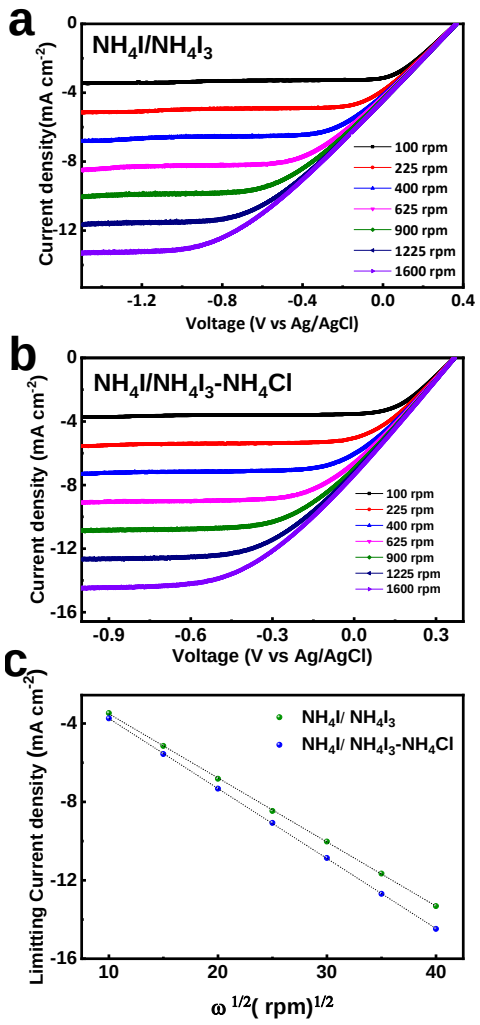

Figure 3.15. Linear Sweep Voltammetry showing effect of NH_4Cl: a) 10 mM NH_4I_3-10 mM NH_4I, b) 10 mM NH_4I_3-10 mM NH_4I-15 mM NH_4Cl catholytes with different rotation speeds. c) limiting current (i_L) versus the square root of rotational speed ($w^{0.5}$) plots for the aforementioned solutions.

Table 3.16. Comparison of diffusion coefficients for I^- ions in different catholytes using the Levich method (Data extracted from Figure 3.15).

Catholyte composition	D_{I^-}	
	Absolute value (10^{-5} cm s^{-1})	Improvement * (%)
NH_4I_3	4.17	-
NH_4I_3- NH_4Cl	4.77	14%

* Improvement (%)$=\frac{D_{NH_4I_3/NH_4Cl} - D_{NH_4I_3}}{D_{NH_4I_3}}$

To gain theoretical insight into the interaction and kinetics of different catholytes with the cathode, X-ray photoelectron spectroscopy (XPS) of the graphite felt electrode and density functional theory (DFT) simulations were both conducted. First, XPS was performed on the graphite felt electrode before and after heat-treatment, which was designed to improve its hydrophilicity. The H-GF was heat-treated at 500 ℃ for 2h in an air atmosphere [87] (Figure 3.3). The XPS results showed that abundant oxygenated species (mainly hydroxide groups) were formed on the surface of the oxidized/hydrophilized graphite felt electrode (Figure 3.16). Thus, the OH-functionalized graphite (G-OH) surface was adopted in the DFT model to accurately simulate the behavior of a real flow battery electrode (Figure 3.11g). DFT results showed that the adsorption energy of I_2Cl^- on G-OH was calculated to be higher than that of I_3^-, suggesting that the former can undergo accelerated electrochemical reactions on the OH-functionalized graphite electrode. Furthermore, in comparison with I_3^-, I_2Cl^- showed a shorter X···H bond length and closer spatial distance to the G-OH plane (Table 3.17).

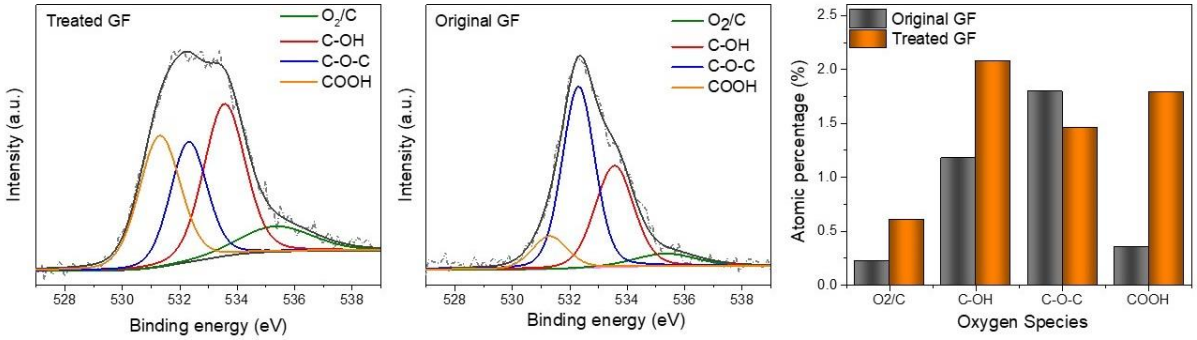

Figure 3.16. XPS results of original and heat-treated graphite felt.

Table 3.17. Summary of DFT calculations for the adsorption of I_2X^- species on hydroxide-functioned graphene plane.

Configuration	E_{ad} (kJ mol^{-1})	Bond length (pm)				Spatial distance of I_2X^- to G-OH (pm)
		O-H	H···X	X-I	I-I	
G-OH/I_3	-0.787	99.2	259.8	297.9	284.8	355.8
G-OH/I_2Cl	-1.322	99.9	215.7	265.9	283.6	329.5

3.3.6 Techno-economic Analysis

Techno-economic analyses of the three tested zinc-iodine RFB systems (namely ZIFB, AC-ZIFB and AC-ZI_3FB) were conducted based on the model presented by Darling et al. [99,100] (See Appendix C for cost calculation details). The cost of energy (US$/kWh) can be defined as the ratio of power cost (US$/kW), including cost of tanks and electrolytes, to total storage duration (h). Therefore, a log-log plot of installed cost versus energy/power ratio (E/P) can be utilized as a rational way to present the cost of storage on an equal basis for different systems [99]. The corresponding log-log plot of installed cost vs. total storage duration (i.e. the ratio of (E/P)) is presented in Figure 3.17a. The unique design of flow batteries, which allows for independent scaling of power and energy, makes all three systems more cost-effective when designed for a longer storage duration (discharge time). However, the ZIFB system

cannot reach the 2023 DOE cost target for energy storage devices (<150 US$ kWh^{-1}) [28] even with 1-year storage duration. By contrast, AC-ZIFB achieves the DOE cost target with 42 hours storage duration. The main reason for these lower costs lies in the fact that low-cost NH_4I (2.7 US$ kg^{-1}) [101], $ZnCl_2$ (1.0 US$ kg^{-1}) [99] and NH_4Cl (0.14 US$ kg^{-1}) [99] in the AC-ZIFB and AC-ZI_3FB systems replaces relatively costly ZnI_2 (15 US$ kg^{-1}) [101] which is inconveniently used in both the anolyte and catholyte of the conventional ZIFB system. Consequently, the chemical cost of AC-ZIFB and AC-ZI_3FB was reduced respectively by 11 and 5 times compared to that of ZIFB, simply by implementing decoupled electrolytes. The difference in cost for AC-ZIFB and AC-ZI_3FB is mainly attributed to the additional price of I_2 used in the AC-ZI_3FB catholyte. Since the chemical cost of AC-ZIFB reaches as low as 43.66 US$ kWh^{-1} (Figure 3.17a), the major contributor to the total installed cost is the expensive CEM used in the AC-ZIFB, i.e. Nafion 117 (500 US$ m^{-2}) [99].

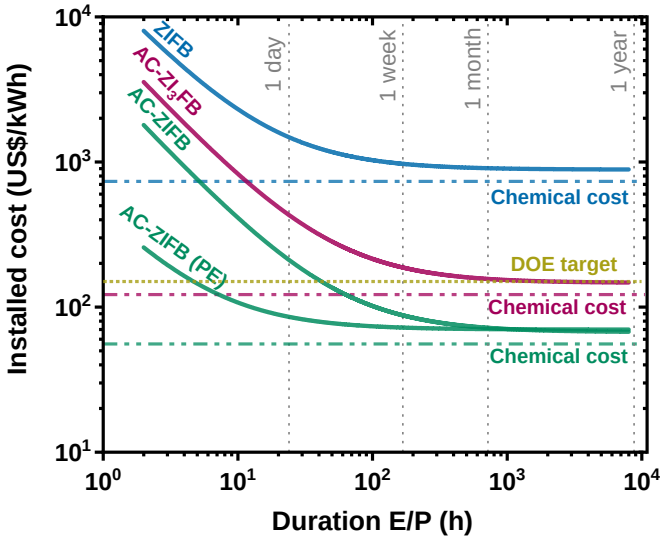

Figure 3.17. log-log plot of installed cost versus storage duration for ZIFB, AC-ZIFB, and AC-ZI_3FB systems. The thick dashed lines represent the chemical cost of each RFBs, the yellow dashed line represents the DOE target for 2023.

The cost calculation of the AC-ZIFBs with the predicted future cost of Nafion 117 membrane (75 US$ m^{-2}) [99] was done based on the same method, and the future installed cost plot is presented in Figure 3.18. With the optimistic expectation of Nafion 117 to reduce its price, the installed cost of AC-ZIFB can be further reduced and meet the DOE cost target with a storage duration of only 11 hours.

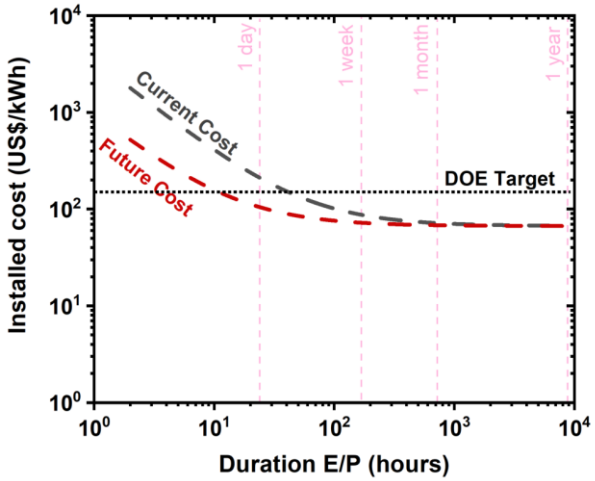

Figure 3.18. Comparison of the installed cost of AC-ZIFB system, using current cost and near-future predicted cost of Nafion membrane.

However, there are still many opportunities for improvement, such as better membrane selection. For example, if a currently available low-cost non-perfluorosulfonic acid (PFSA) based membrane is used as an alternative to Nafion, the installed cost can be further decreased [102,103]. To demonstrate the potential viability of this option, a low-cost microporous polyolefin (PE) membrane (1-20 US$ m^{-2}) [60] was assembled in AC-ZIFB and operated at higher current density. The concentration of 5 M I^- in the catholyte displayed respectable charge-discharge curves at current densities as high as 80 mA cm^{-2} (Figure 3.19a). This system showed average charge and discharge voltages of 1.5 V and 1.2 V respectively, with stable cyclability of 1,100 cycles with high CE (93%), VE (80%) and EE (75%) at the current density of 80 mA cm^{-2} (Figure 3.19b).

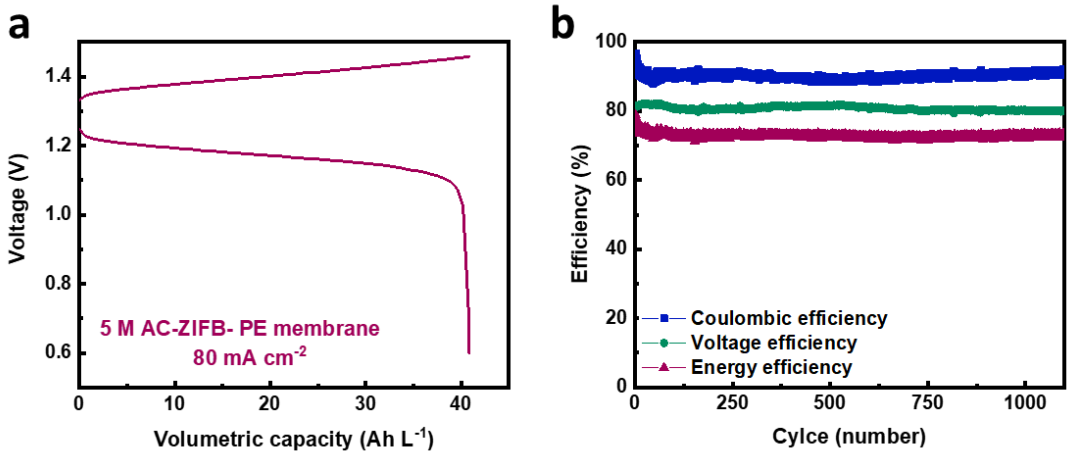

Figure 3.19. Electrochemical performance of AC-ZIFB with 5M I^- test cell using PE membrane at current density of 80 mA.cm^{-2}. a) Charge-discharge profile b) Cycling performance.

Similarly, the cost calculation of the AC-ZIFBs with PE membrane (10 US$ m^{-2}) [60] was done using the same cost calculation, and presented in the log-log plot (Figure 3.17). The installed cost of AC-ZIFB with low-cost membrane could reduce to below 150 US$/kWh in just 5 h discharge time. Further comparison of installed cost with previous scenarios is presented in Figure 3.20. The calculated installed cost was reduced by 5.7, 4.9 and 4.3 times for storage durations of 4 h, 6 h and 8 h, respectively. The decoupled electrolyte design combined with a cost-effective membrane is the first zinc-iodine RFB to demonstrate substantial cost savings and achieve the 2023 DOE cost target for RFBs.

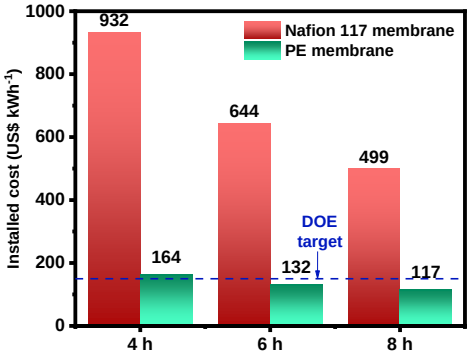

Figure 3.20. Comparison of the installed cost of the AC-ZIFBs for 4 h, 6 h and 8 h storage durations with Nafion membrane versus PE membrane used in cell stack.

The comprehensive evaluation of cyclability and EE together with techno-economic analyses of the three systems (using Nafion 117 CEM) is compared in Figure 3.21. Both AC-ZIFB and AC-ZI_3FB systems demonstrate highly improved cyclability and enhanced EE, in addition to cost reductions in terms of chemical costs, total installed cost with 1-day storage and long-term energy cost compared to the conventional ZIFB system. Notably, considering all five aspects in the radar plot, AC-ZIFB is highlighted to be the most promising and cost-effective zinc-iodine RFB system.

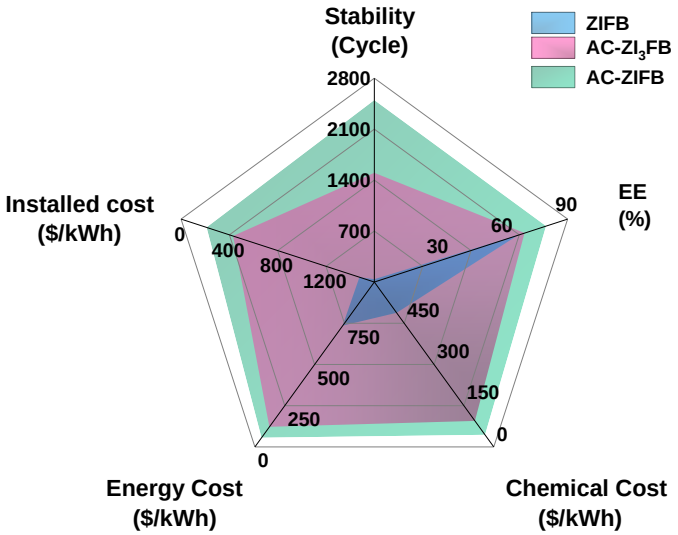

Figure 3.21. Comparison of ZIFB (blue area), AC-ZI_3FB (red area), and AC-ZIFB (green area) systems in terms of stability, energy efficiency and chemical, energy, and installed costs for 1-day storage duration.

3.4 Summary

We have clearly demonstrated through experimental work, further supported by theoretical computation, that implementation of a decoupled multifunctional NH_4Cl supported electrolyte improved the performance, flexibility and practical feasibility of ZIFBs over several aspects. Firstly, the cycle life was substantially improved, accomplishing 2,500 cycles, as a result of NH_4Cl primarily facilitating zinc deposition and suppressing zinc dendrite formation at the anode. NH_4Cl addition also

unlocked enhanced capacity (128.0 Ah L^{-1}), owing to the beneficial effects of both NH_4^+ and Cl^- ions. Firstly, NH_4^+ simultaneously improved charge carrier conductivity while suppressing capacity loss by mitigating Zn^{2+} crossover. Secondly, NH_4^+ also stabilized the formation of I_2Cl^-complex during charging, which increased capacity. Overall, NH_4Cl improved energy efficiency by improving the kinetics of both I_3^-/I^- and Zn^{2+}/Zn redox reactions. The flexibility of the proposed electrolyte system was also demonstrated, having maintained excellent performance and cyclability independent of charge/discharge state. On top of these, utilizing low-cost ammonium salts in a decoupled electrolyte, instead of the moderately costly zinc iodide (ZnI_2) in a matched electrolyte, dramatically reduced the installed cost of a flow battery system. In fact, the AC-ZIFB is the first demonstrated zinc-iodine RFB that achieved a low installed cost of 150 US$/kWh with only 5-hours discharge time, utilizing a cost-effective porous membrane. However, though these preliminary results are promising, challenges including electrolyte crossover problem, electrode polarization, zinc dendrite formation. Development of a membrane [104], highly active electrocatalyst [105] and advanced cell design [106] can further idealize this system in the future. Overall, this breakthrough approach in electrolyte chemistry can significantly promote the application of RFBs for large-scale energy storage by not only paving the pathway for zinc and iodine electrolyte systems, but also, in a broader sense, all RFB chemistries that face the same challenges and conflicting requirements at the anolyte and catholyte.

Chapter 4

Elucidating and Tackling Capacity Fading of Zinc-Iodine Redox Flow Batteries

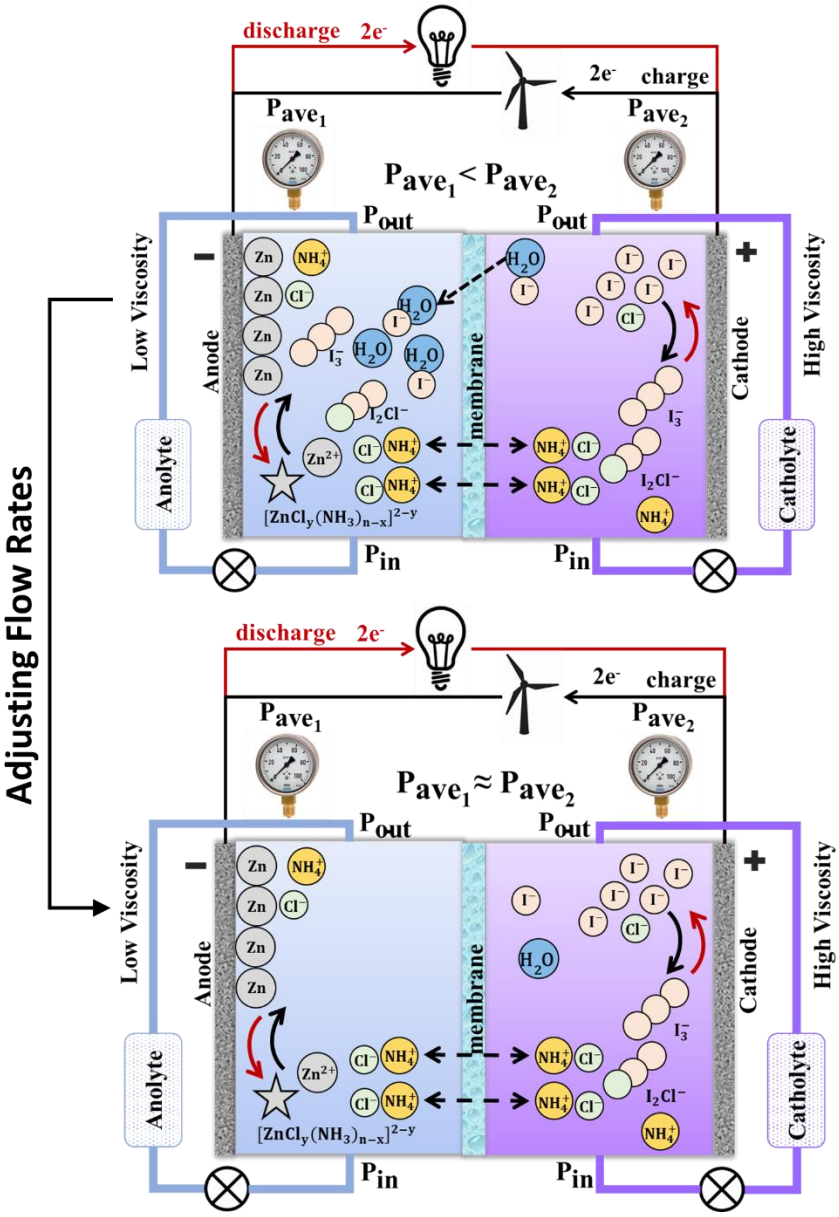

4.1 Introduction

Redox flow batteries (RFBs) with inherent attributes of high safety, high efficiency, and long cycle life are one of the most promising large-scale energy storage technologies to integrate with renewable energies [8,107–109]. Development of RFBs has focused largely on all-vanadium redox flow batteries (VFBs) due to their impressive reliability [10,36]. Despite that, one of the main pitfalls of VFBs is the limited chemical stability of membranes to the strongly oxidative V(V) species [5,33,36,110–112], which narrows down the options to high-cost Nafion-based membranes [12,112]. Regarding the use of less oxidative chemistries, high energy density zinc-iodine redox flow batteries (ZIFBs) with electrolytes containing I_3^-/I^- (positive) and Zn^{2+}/Zn (negative) redox couples have gained much interest as next-generation RFBs [5,11,13–18]. Compared to strongly oxidative V(V) species, the less oxidative nature of I_3^-/I^- allows the implementation of inexpensive hydrocarbon-based membranes. Yet, ZIFBs have also faced enormous challenges to reach their full potential, including extending the battery capacity, voltage, and cycle life while reducing the overall cost. Different approaches have been explored to address some of these challenges, such as modifying electrolyte design via incorporation of bromide [17] and chloride [113] complex-forming ions, tailoring anolyte pH [16], and integrating low-cost ammonium-based salts (AC-ZIFBs) [113]. However, the broad market penetration of ZIFBs is still an unsolved challenge. To reach the cost target of the US Department of Energy (DOE) and enable the mass adoption of ZIFB, costly Nafion ($500 m^{-2}) must be replaced by low-cost alternatives such as Daramic microporous polyolefin (PE) membranes ($1-$20 m^{-2}) [60]. Therefore, ZIFBs equipped with porous PE membrane and durable low-cost ammonium-based electrolyte are one of the most promising RFB systems for the energy storage market.

Despite the flourishing development of ZIFBs, they suffer from similar embarrassing operational instability seen with VFBs, where capacity significantly decays over long-term cycling due to species crossover. Besides causing capacity fade, crossover can also lead to other cross-contamination

problems such as precipitation, membrane fouling, or component degradation [114]. The painstaking intermittent replenishment or replacement of electrolyte is needed for long-lasting smooth operation of VFBs and ZIFBs, which increases maintenance burden and hinders technological large-scale commercialization. Substantial efforts have been devoted to mitigating capacity fade in porous-membrane based VFBs by replenishment of electrolyte [114,115], pulse electrolyte flow [116], applying asymmetric pressures to the tanks [68], and addition of draw solutes [117]. By virtue of these efforts to decreasing the magnitude of active ions crossover, VFBs are one of the most widely commercialized RFB systems. Despite the similar promising results of porous membrane- based ZIFBs [15], their capacity fade over long-term charge-discharge cycling has never been revealed, let alone the mechanism of capacity fade and coping strategies to limit its impact on ZIFB performance, longevity, and, ultimate commercial viability.

Herein, insight is gained into the mechanism of capacity fade over long-term ZIFB cycling through a systematic investigation. A ZIFB with porous PE membrane and an ammonium-based, decoupled $Zn^{2+}$and I^- electrolyte (AC-ZIFB) is evaluated as a prototypical example to reveal the exceptional potential of a strategically designed system. First, the changes in electrolyte properties were measured and correlated with electrochemical performance during cycling. It was found that different viscosities and densities of the anolyte and catholyte disrupt the pressure balance within the cell stack, thus accelerating the electrolyte transport from catholyte to anolyte via convection. The colossal catholyte transport causes severe (poly)iodide crossover and accumulation in the anolyte, eventually resulting in capacity fade. Based on the understanding of this mechanism, manipulating the flow rates of electrolytes was suggested to simultaneously decrease the individual pressure drops in all flow cell components (graphite felt electrodes, pipes, and flow channels), consequently decreasing the total pressure drop within the cell stack. An AC-ZIFB with catholyte to anolyte flow rate ratio of 1 to 7 was able to significantly inhibit the (poly)iodide crossover and achieved the highest reported cycle life of

1,100 cycles at a high current density of 80 mA cm^{-2}.The deep insight into the capacity fade mechanism and the proposed methodology to sustain capacity can positively contribute to the commercialization of redox flow batteries.

4.2 Materials and Methods

4.2.1 Assembly of the Lab-scale Redox Flow Battery

The AC-ZIFB flow cells were fabricated by sandwiching Daramic microporous polyolefin (PE) membranes between two pieces of heat-treated graphite felt (H-GF, SGL Carbon Group, Germany) embedded in graphite plates with an apparent area of 3 cm×3 cm, fixed between two aluminum plates. The graphite felt was heat-treated in air atmosphere at 500°C for 2 h. The Daramic polyolefin microporous membranes had median pore size, porosity, and thickness of 0.15 µm, 57%, and 900 µm, respectively. A cross-sectional scanning electron microscopy (SEM) image is provided in Figure 4.1, indicating silica particles embedded in polyolefin matrix. The PE membrane was sonicated in DDI water for 1 h prior to use to remove trapped air bubbles in the membrane matrix. In all flow cells in this work, the catholyte is composed of 5 M ammonium iodide ($NH_4I \geqslant 99\%$, Aldrich) with addition of 2.5 M ammonium chloride ($NH_4Cl \geq 99.5\%$, Aldrich) as supporting electrolyte and the anolyte consists of 2.5 M zinc chloride ($ZnCl_2 \geq 98\%$, Aldrich) with addition of 2.5 M ammonium chloride ($NH_4Cl \geq 99.5\%$, Aldrich) as supporting electrolyte. The electrolytes, with volume of 10 ml, were then purged with nitrogen for 30 min and sealed to minimize exposure to oxygen prior to testing.

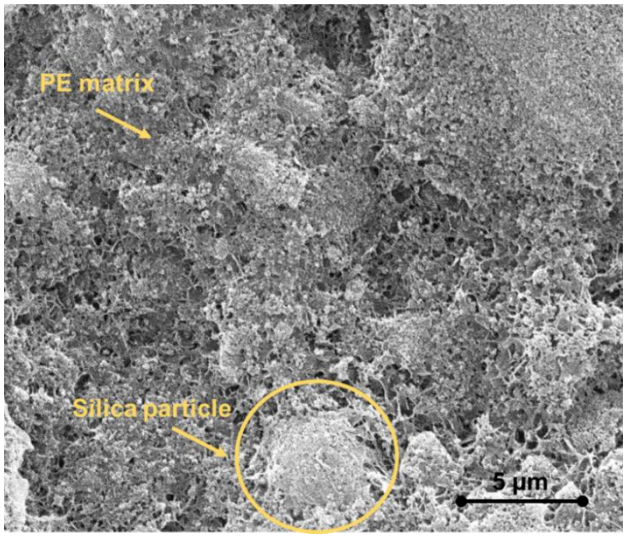

Figure 4.1. SEM image of the as-received porous PE membrane.

4.2.2 Electrochemical Measurements

The electrochemical charge-discharge tests were conducted on a potentiostat/galvanostat (Land Electronic Co., Ltd., Wuhan) with the voltage cut-off range of 0.6-1.6 V at constant current density of 80 mA cm^{-2}. The electrolytes were circulated in the cell stack using peristaltic pumps at flow rates listed in Table 4.1.

Table 4.1. Operating conditions of flow cells, with anolyte and catholyte operating in the same and tuned flow rate conditions.

Operating condition	Catholyte to anolyte flow rate ratio (Q_c:Q_a)	Anolyte flow rate		Catholyte flow rate	
		RPM	ml min^{-1}	RPM	ml min^{-1}
Same flow rate condition	1:1	100	15	100	15
Tuned flow rate condition	1:3	100	15	33	5
	1:5	100	15	20	3
	1:7	100	15	14	2

4.2.3 Electrolyte Viscosity Measurements

The electrolyte viscosity was measured by a capillary-type viscometer at 25°C. The instrument was first calibrated with pure DDI water. Then, the viscosity of electrolytes were calculated based on Eq. 4-1 [118]:

$$\mu_s = \frac{\mu_w \times \rho_s \times t_s}{\rho_w \times t_w} \qquad (4\text{-}1)$$

where μ_s (Pa. s) and μ_w (9.354×10^{-4} Pa. s) are viscosity coefficients, ρ_w (9.47 g cm^{-3}) and ρ_s (g cm^{-3}) are densities, and t_w (s) and t_s (s) are flow time through viscometer for the electrolyte and DDI water, respectively.

4.3 Results and Discussion

4.3.1 Capacity Fade of AC-ZIFBs

During charging of the flow cell, metallic zinc is electrodeposited on the H-GF anode while I^- ions are oxidized to I_3^- and I_2Cl^-, delivering an approximate theoretical cell voltage of 1.3 V [113]. The Coulombic efficiency (CE), voltage efficiency (VE) and energy efficiency (EE) over cycling are presented in Figure 4.2a. The CE values decreased gradually from 94% to 90% over the first 11 cycles until it dropped to 70% at the 12^{th} cycle. In general, flow cells with porous membranes exhibit lower CE than those with Nafion membranes due to the different ion transport mechanism. In AC-ZIFBs with porous membranes, the inter-connected micro-pores provide much larger channels than Nafion for charge carrier transport. Thus, beside the counter ions (mostly NH_4^+ and Cl^-) [119], active species (i.e. polyiodide) must encounter less barriers to cross through the membrane, mainly due to the lower selectivity of PE membrane [60]. The higher cross-contamination of active species from the cathode side to the anode side will lead to lower CE in PE-based ZIFBs. Despite the gradual decrease in CE values, the VE remained almost constant with an average value of 83% for 12 cycles. As a result, the

EE value (EE=CE×VE) decreased gradually from 78% to 70% over the first 11 cycles until it fell sharply to 60% at the 12th cycle.

Figure 4.2b depicts the charge-discharge curves as a function of time. The steady increase of charging overpotential was observed as the cycling proceeded, exhibiting operational instability of the AC-ZIFB flow cell. The change in anolyte and catholyte volume as a function of cycle number is plotted in Figure 4.2c. As cycling proceeds, the volume of anolyte increased while the volume of catholyte decreased with almost the same rate until 2/3 of the catholyte tank was emptied at the end of 12 cycles. This undesirable transport was most likely the underlying reason for the substantial instability during the operation of AC-ZIFB, which eventually led to termination when the catholyte was heavily depleted. Consequently, insight to the causes of this drastic electrolyte transport can solve the puzzle of performance loss in flow batteries. Ultimately, further investigation is essential to find a sensible correlation between volume change and performance degradation in order to implement solutions that prevent large electrolyte volume and performance changes during cycling.

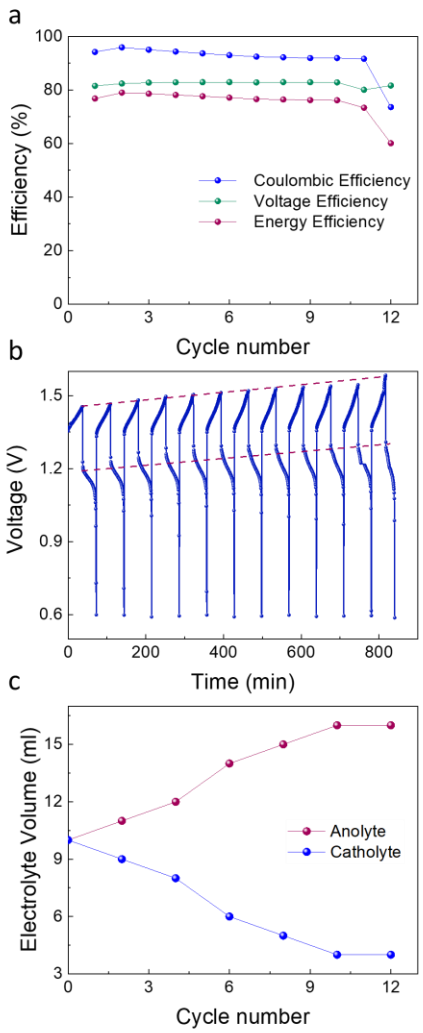

Figure 4.2. Electrochemical performance and electrolyte volume of AC-ZIFB with PE membrane at the current density of 80 mA.cm^{-2}. (a) Cyclic performance in terms of CE, VE and EE, (b) Voltage profile as a function of time, and (c) Electrolyte volume change during cycling at current density of 80 mA.cm^{-2}.

4.3.2 Capacity Fade Mechanism

Transport through membranes is at the heart of various underlying issues affecting the long-term viability of RFBs, especially under heavy duty cycling. In a general sense, undesirable transport of active species through the membranes is a common mode of capacity fade. Crossover of active species leads to concentration imbalance of active ions in both anolyte and catholyte sides, resulting in a net

decrease in the accessible capacity. To have optimum capacity retention, only supporting ions must exchange between the two electrolytes in order to maintain charge neutrality and balance of redox reactions; however, the imperfect selectivity of membranes eventually results in unwanted active species and solvent passage between the electrolytes [114]. The crossover of active species is driven by a combination of concentration (i.e. diffusion), potential (i.e. migration), and pressure (i.e. convection) gradients between the two sides of membranes, i.e. catholyte and anolyte [67,68]. While diffusion and migration are not commonly inferred to as the dominant reasons for severe ion species crossover, the convective forces caused by unbalanced hydraulic pressure plays a major role in the collective movement of the catholyte solution through the porous membrane to the negative side [68]. Convection originates from pressure gradients, known as hydraulic pressure, across the membrane. As described by Darcy's Law (Eq. 4-2), the hydraulic pressure can drop inside a flow battery cell stack when a viscous solution moves a given distance in a graphite felt electrode [120].

$$\Delta p_{porous} = \frac{l}{A}\frac{\mu Q}{k} \qquad (4\text{-}2)$$

where l, μ, A, k, and Q are the length of the porous medium, the dynamic viscosity of the fluid, cross-sectional area, flow rate, and the permeability of the porous electrode, respectively. The permeability of the porous electrode can be determined by Eq. 4-3 [120]:

$$k = \frac{d_f^2}{16K}\frac{\varepsilon^3}{(1-\varepsilon)^2} \qquad (4\text{-}3)$$

where d_f, K, and ε are the fiber diameter, Kozeny-Carman constant, and porosity, respectively. According to the Eq. 4-2, the electrolyte viscosities are the only variables affecting hydraulic pressure drops in graphite felt electrodes when the anolyte and catholyte flow rates are the same. Thus, the electrolyte viscosities were measured at different SOCs (Figure 4.3a) to shed light on the observed performance instability of the flow cell.

The results show that the viscosity of catholyte continually increased at SOCs higher than 20%, while the viscosity of anolyte remained almost unchanged after an initial slight change at 20% SOC. As depicted from Darcy's equation, viscosity and pressure drop are linearly correlated when all other parameters (cross-sectional area, the permeability of the porous electrode, and flow rates) are identical at two sides of membrane. As a consequence, the catholyte must experience higher average pressure ($P_{ave}=\frac{P_{in}+P_{out}}{2}=P_{out}-0.5\Delta P$) [68] than anolyte. This induced pressure gradient drives the transport of electrolyte from high pressure (catholyte) to low pressure (anolyte),carrying bonded (poly)iodide active ion species [114]. When poly(iodide) moves to the negative side, it can contribute to capacity fade in two ways. First, by chemical reaction with the deposited zinc at the surface of the electrode to Zn^{2+}, i.e. self-discharge the battery (Figure 4.3b). Second, by accumulating (poly)iodide ions at the anode side, it renders the catholyte ineffective in providing capacity due to unavailability of (poly)iodide active species at the cathode side. To validate this theory, the rates of capacity fade of 50% SOC-charged flow cells were measured and anolyte titration after cycling were performed. The trends in capacity fade are presented in Figure 4.3c using the flow cell discharge profiles after a given time period. The results show an average of 11% loss in capacity due to self-discharge per hour with a gradual increase in discharge overpotential. This supports the notion that (poly)iodide significantly crosses from catholyte to anolyte and contributes to capacity fade by chemical reaction with the deposited zinc at the surface of the electrode.

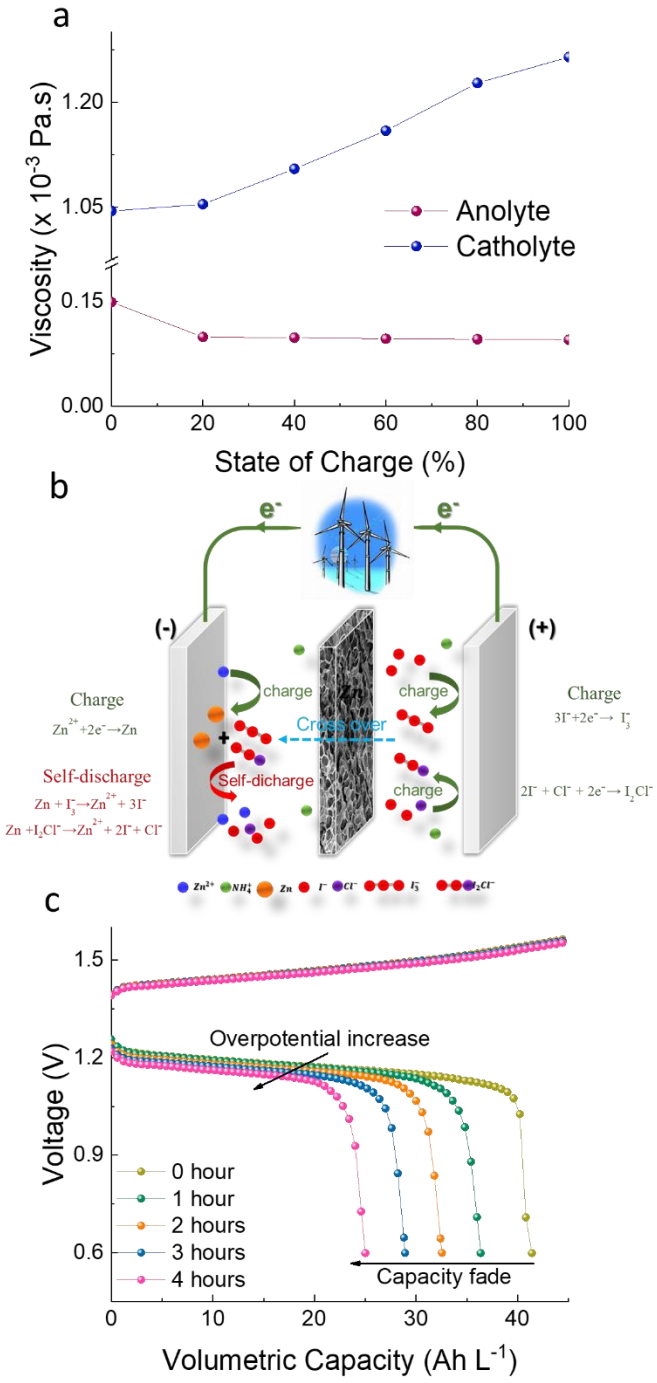

Figure 4.3. Capacity fade mechanism in ZIFBs with PE membrane. a) The viscosity measurements of anolyte and catholyte at different state of charges (SOC), b) The schematic of capacity fade mechanism by self-discharge of the flow cell, c) The charge-discharge profile of 50%-SOC flow cells for a given times.

Additionally, soluble starch was utilized as an indicator of (poly)iodide to perform the titration of anolyte as the cycling proceeds. The color change of anolyte to red upon addition of the indicator (Figure 4.4) further confirmed the presence of (poly)iodide and the extent of (poly)iodide loss in the catholyte during cycling.

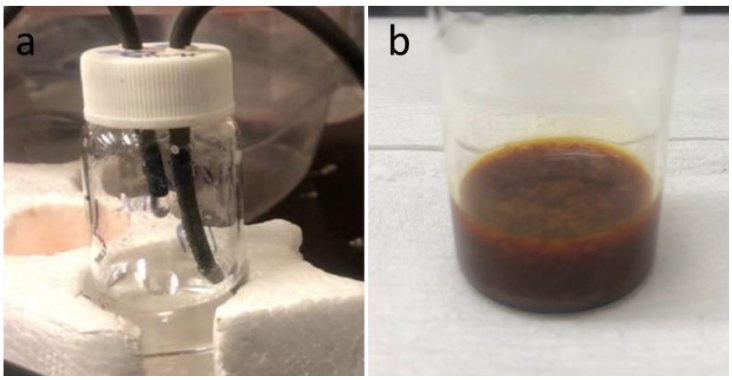

Figure 4.4. The color change of anolyte solution from a) transparent to b) red, upon addition of soluble starch.

4.3.3 Capacity Remediation Strategy

Based on the described capacity fade mechanism and our experimental results, the capacity could be sustained if the asymmetric water flux, and subsequently (poly)iodide crossover, are inhibited. Therefore, an intuitive approach to mitigate electrolyte transport is to maintain a balanced hydraulic pressure between the two side of porous membrane. Hydraulic pressure has long been applied as the driving force to counteract osmosis pressure in water purification processes such as micro-, ultra-, and nano-filtration, and reverse osmosis. The higher hydraulic pressure impels the water to transport in the opposite direction of concentration gradient up to a point that the equilibrium is reached [60]. In a similar manner, it is conceivable to reduce the unbalanced transport of active (poly)iodide species along with catholyte by applying counter-hydraulic pressure to the negative side of AC-ZIFBs. In essence, AC-ZIFBs capacity fade issue is addressed by adopting different flow rates at the catholyte and anolyte

to balance the hydraulic pressure across the porous membrane, thereby diminishing the volume change during long cycling.

The total pressure loss that an AC-ZIFB flow cell experiences is the sum of the pressure drops in each individual cell stack components. Besides the pressure drop in GF electrode ($\Delta p_{porous} = \frac{l}{A}\frac{\mu Q}{k}$), pressure losses in pipes and flow channels are the other two main contributors in this regard. Darcy-Weisbach's Law (Eq. 4-4) was employed to calculate the pipe head loss and flow channel pressure drops:

$$\Delta \mathbf{p_{pipe,\ channel}} = \mathbf{f_D}\frac{\mathbf{L}}{\mathbf{d}}\frac{\boldsymbol{\rho}\ \mathbf{(Q.A)^2}}{\mathbf{2}} \quad \textbf{(4-4)}$$

where f_D represents the Darcy friction factor, d, L, ρ, Q, and A are the pipe (or channel) diameter, pipe (or channel) length, fluid density, flow rate, and pipe (or channel) area, respectively. Since the fluid flow remains in the laminar region, the Darcy friction factor is obtained based on Reynolds number (Eq. 4-5):

$$\mathbf{f_D} = \frac{\mathbf{64}}{\mathbf{Re}} \qquad \textbf{(4-5)}$$

Accordingly, to maintain a balanced hydraulic pressure, the combined pressure drops in pipe, flow channel, and porous must be minimized. Taking a closer look at the above equations, length to pipe (or channel) diameter ratio (L/d), length to cross section area of electrode (l/A), and flow rate (Q) are the variables that can affect the total pressure drop in a flow cell stack. Among these variables, only flow rate can be easily manipulated to regulate all three hydraulic pressure drop contributors through a linear relationship.

Given the significant impact of electrolyte flow conditions on induced pressure gradients, estimating the pressure drop at various asymmetric flow rates of anolyte and catholyte can provide invaluable insight on the magnitude of electrolyte transport and consequently, the cell performance and durability.

Using the constant parameters in Table 4.2, the absolute value of pressure drops in porous medium, pipe, and flow channel for a wide range of flow rate ratios, Q_c:Q_a, were calculated and presented in the Figure 4.5a.

Table 4.2. Parameters for theoretical optimization calculations.

Parameters	Value
Anolyte density (g/cm^3)	1.2
Catholyte density (g/cm^3)	1.4
Porous electrode dimension (cm)	3 × 3 × 0.6
Fiber diameter (μm)	5
Electrode porosity (%)	94
Kozeny-Carman constant	4.28
Ratio of pipe length to cross-sectional area (cm^{-1})	497
Ratio of channel length to cross-sectional area (cm^{-1})	750

When the Q_c:Q_a ratio is lower than 1:7, the pressure drops in the cathode side is higher than the anode side. At Q_c:Q_a ratio of 1:1 the difference in pressure drop of the anolyte and catholyte in graphite felts, pipes, and flow channels are 50.6 Pa, 119.7 Pa, and 144.4 Pa, respectively. As mentioned earlier, this pressure difference acts as a driving force for convection within the cell stack, leading to electrolyte transport from the side with higher pressure (cathode side) to lower pressure (anode side). While viscosity does not affect the pressure drop in flow channels and pipes, the density of anolyte and catholyte can directly affect the pressure drop in these compartments. Since the density of anolyte is lower than the catholyte, the pressure drops in flow channels and pipes in the cathode side is lower than the anode side. In addition, while the viscosity contributes to the pressure drop in porous electrodes, the electrolyte density has a linear relationship to the viscosity. Thus, the density of electrolyte indirectly affects the pressure drops in porous electrodes, leading to lower pressure drop in anode side than cathode side due to lower density of anolyte. In general, it can be concluded that both viscosity

and density are the main factors that play major roles in pressure drop in anode and cathode sides. With increasing Q_c:Q_a ratio, the pressure drop in the anode side starts to increase and the difference in the pressure drop has a downward trend which at Q_c:Q_a ratio of 1:7 the minimum value of 2.2 Pa, 8.4 Pa, and 10.2 Pa for pressure drop difference graphite felts, pipes, and flow channels, respectively, are achieved. However, the pressure drop at the anode side becomes larger than the cathode side when Q_c:Q_a ratio is higher than 1:7, consequently the convection leads to electrolyte transport in a reverse direction (from anode side to cathode side). In general, pressure drop in flow channels and electrode have the most and least significance, respectively, in the total pressure drop at different catholyte: anolyte flow rate ratios. The total average pressure drops can be defined as the difference in the average hydraulic pressure of anolyte and catholyte ($0.5\ \Delta P_{total}$). The value for the flow cells with different flow rate ratios are presented in Figure 4.5b. As is depicted from the plot, the difference in average hydraulic pressure of the two sides is more balanced when the optimum Q_c:Q_a ratio is 1:7.

It is anticipated that compared to the AC-ZIFBs operating with the same flow rate (Figure 4.5c), manipulating operating parameters can act as a means of generating an effective counterpressure to reduce capacity fading and inhibit (poly)iodide crossover. Considering the calculation results, a cell running under Q_c:Q_a ratio of 1:7 must exhibit the most stable performance due to a more balanced pressure drop between both sides of membrane as a result of inhibited (poly)iodide crossover (Figure 4.5d).

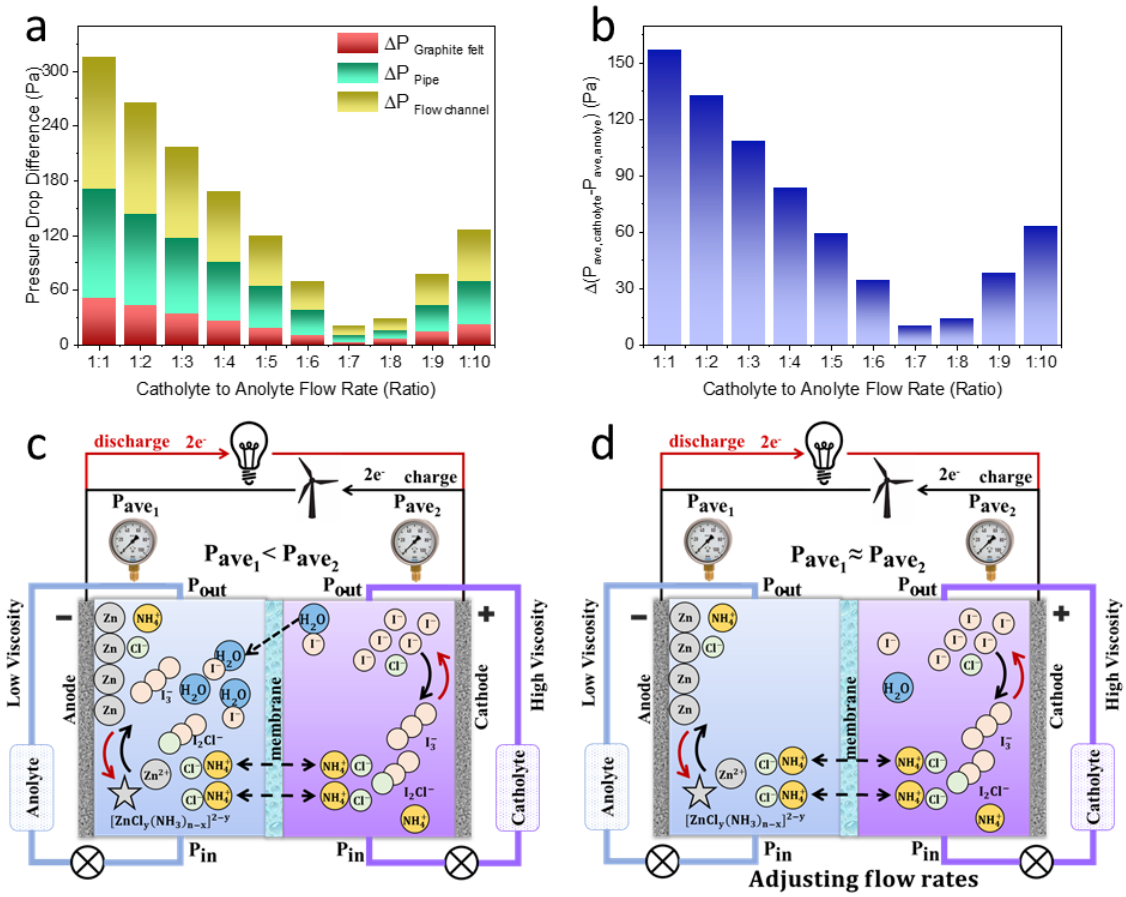

Figure 4.5. The principles of capacity remediation strategy for AC-ZIFBs. a) The difference in the catholyte and anolyte pressure drops in graphite felts, pipes, and flow channel, b) The difference in the average pressure of catholyte and anolyte as a function of Catholyte: Anolyte flow rate ratio, c) The schematic of unbalanced hydraulic pressure inside a ZIFB cell stack and consequent transport of water and (poly)iodide species. d) The proposed strategy to remediate capacity fade by balancing the pressure at the two sides of the membrane by the adjusted flow rate ratio of 1:7.

4.3.4 Flow Cell Performance

With a deeper understanding of the capacity fade mechanism and the proposed remediation strategy, flow cells were tested with different Q_c:Q_a ratios at a current density of 80 mA cm^{-2} for further investigation. The goal was to explore whether decreasing the catholyte flow rate can effectively mitigate electrolyte transport and stabilize the electrochemical performance.

Since the major effect of unbalanced hydraulic pressure was observed to be asymmetric electrolyte transport, water displacement was closely monitored for the first 10 cycles (Figure 4.6a). Compared to operating with the same flow rates (Q_c:Q_a = 1:1), slightly higher relative anolyte flow rate (Q_c:Q_a = 1:3) resulted in a minor but measurable improvement in electrolyte volume change (i.e. lesser volume change over cycling). The electrolyte volume became stable when operated under the electrolyte flow rate ratio of 1:5 and 1:7.

The electrochemical performance of the cells is also compared for the first 10 cycles. The CE, VE and EE of the flow cells are compared for the first 10 cycles (Figure 4.6b, c and d). As can be seen, the CE of all flow cells were almost identical, indicating that electrolyte flow rate did not have a significant effect on parasitic reactions in the flow cells. However, at higher Q_c:Q_a electrolyte flow rate ratios, the VE, and thus EE, was improved.

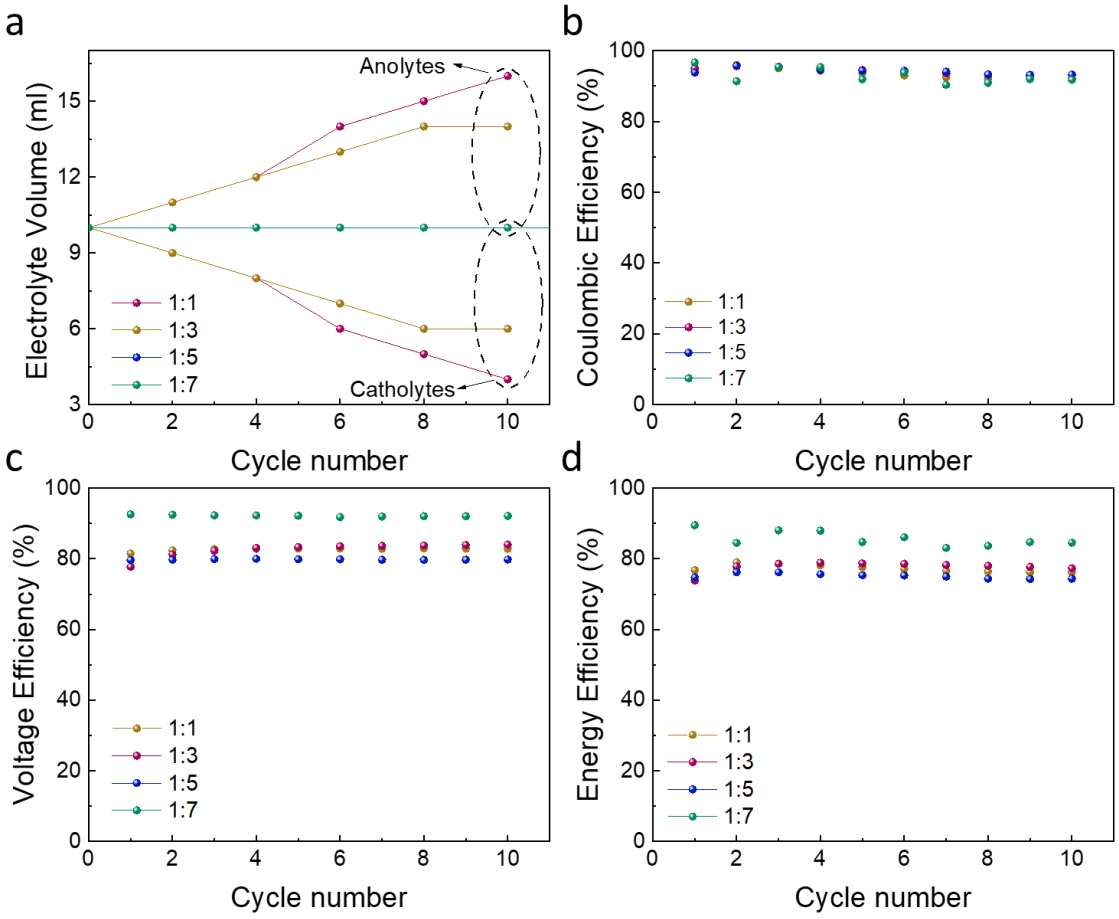

Figure 4.6. Water transport and electrochemical performance of AC-ZIFBs operated with catholyte: anolyte flow rate ratio adjustments. a) The volume change of anolyte and catholyte over cycling at different flow rate ratios with 5M I^- catholyte under current density of 80 $mA.cm^{-2}$ (Note that the volume of anolyte and catholyte with 1:5 and 1:7 flow rates remained unchanged during the first 10 cycles; thus, all points overlap along the same line in the graphs). Electrochemical performance of ZIFBs in terms of b) CE, c) VE and d) EE under current density of 80 $mA.cm^{-2}$.

The flow cells operated with different flow rates were further tested under heavy duty cycling at the current density of 80 mA cm^{-2} where the volume change of electrolytes and specific capacity were closely monitored. The objective was to evaluate the longer effect of flow rate modifications on electrolyte volume change and electrochemical performance. An ideal scenario would be that no change

in electrolyte volume and performance loss is observed during cycling when the counterbalance pressure is imposed to compensate for the developed pressure inside the cell stack.

At a slightly higher anolyte flow rate (Q_c:Q_a= 1:3), a noticeable electrolyte volume change was observed throughout e cycling, indicating water transfer from the positive to the negative side (Figure 4.7a). The volume change for the Q_c:Q_a = 1:5 was almost stable over the first 100 cycles, while a decrease in catholyte volume (and subsequent increase in anolyte volume) was observed afterwards (Figure 4.7b). With the Q_c:Q_a= 1:7, the positive and negative electrolytes maintained a constant volume during cycling with no observable volume change for 380 cycles, indicating negligible water transfer between positive and negative half-cells. A gradual decrease in catholyte volume (and subsequent increase in anolyte volume) was then detected until the flow cell reached 1,100 cycles (Figure 4.7c). At this point, it can be concluded that the lower flow rate of the catholyte is effective for decreasing the net flux of water; hence, the tuned flow rate could reduce the difference in hydraulic pressure and mitigate catholyte transport.

The extended electrochemical performance and specific volumetric capacity of the flow cells under asymmetric flow rate condition were studied by cycling at 80 mA cm^{-2} with charging to 50% SOC (37 minutes for each charge cycle) unless the 1.6 V cut-off limit was reached first. While the cycle life under the symmetric flow rate condition was short-lived (12 cycles), a slightly higher anolyte flow rate (Q_c:Q_a= 1:3) exhibited minor improvement in the cycle life since depletion of catholyte was slightly delayed, but its cycle life was still unacceptable (Figure 4.7d). The CE, VE and EE for the Q_c:Q_a= 1:5 was mainly stable over 180 cycles, with slight variations most likely due to volume changes (Figure 4.7e). When the Q_c:Q_a= 1:7 was chosen, a stable electrochemical performance is observed for 1100 cycles (Figure 4.7f) cycles with slight variations, mainly due to the much slower electrolytes volume change over cycling. This is the highest reported cycle life of the AC-ZIFB at high current density of

80 mA.cm^2. Overall, the cycling performance of the flow cell with Q_c:Q_a= 1:7 was stable, although noticeable electrolyte volume oscillations existed. It can be highlighted that both Q_c:Q_a= 1:5 and Q_c:Q_a= 1:7 asymmetric conditions could verify the initial assumption that a more balanced hydraulic pressure can lead to improved performance, while the Q_c:Q_a= 1:7 showed the most promising results both in stable electrolyte volume, electrochemical performance and cycle life. Thus, the water and combined (poly)iodide ion transfer during the battery operation was reduced, enabling the system to deliver a much-improved capacity-retention capability. The specific capacity of the flow cells under asymmetric flow rate condition is also presented in Figure 4.7g,h,i. The batteries were charged to 50% SOC without reaching the cut-off voltage of 1.6 for 17, 100, and 330 cycles in Q_c:Q_a= 1:3, 1:5, and 1:7, respectively. After that, the flow cells experienced gradual capacity loss over the remaining cycles and exhibited a drop in % SOC until it reaches ~20% SOC. When the catholyte of the symmetric flow rate and asymmetric flow rate conditions are compared, the asymmetric flow rate condition has a consistently larger amount of iodide/polyiodide species in the catholyte over each cycle due to the lower rate of capacity loss. Thus, the rate of capacity decay can be alleviated significantly by a modified flow rate strategy which counterbalances the hydraulic pressure and reduces the iodide crossover. However, the non-equilibrium transfers of water and iodide ions still exist, ultimately leading to electrolyte imbalance.

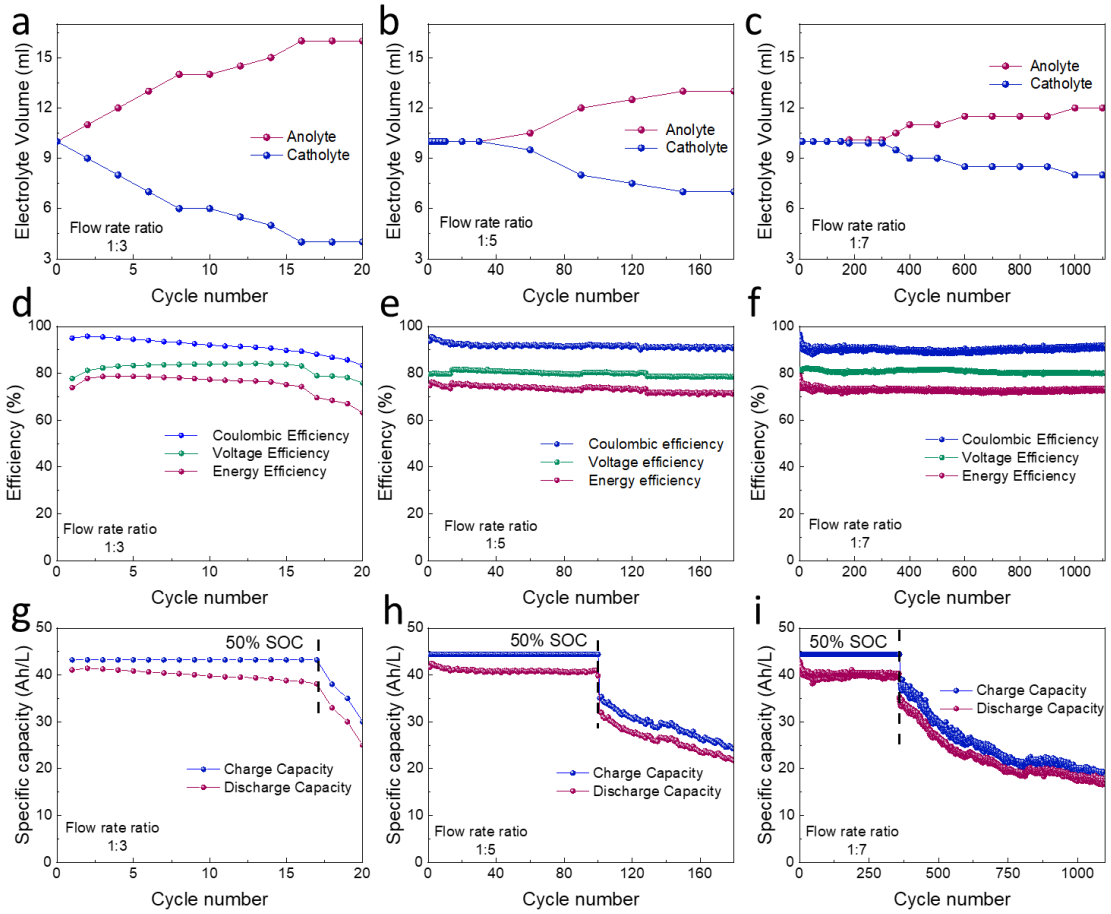

Figure 4.7. Water transport behaviour and electrochemical performance of AC-ZIFBs with catholyte: anolyte flow rate ratio adjustments under heavy duty cycling. The Volume change of anolyte and catholyte under anolyte: catholyte flow rate ratio of a) 1:3, b) 1:5, and c) 1:7. Extended cycling performance of the flow cells at flow rate ratios of d) 1:3, e) 1:5, and f) 1:7. The specific capacity of the flow cells at flow rate ratios of g) 1:3, h)1:5, i)1:7 with 5M I^- catholyte under current density of 80 mA.cm^{-2}.

4.4 Summary

The viable application of RFBs heavily relies on improving capacity retention since capacity fade constitutes one of the major barriers hindering RFB commercialization. In this study, the mechanism of capacity fade was investigated in ammonium chloride-assisted zinc-iodine redox flow batteries (AC-ZIFBs) with porous PE membrane and low-cost Zn^{2+} and I^-decoupled electrolytes. It was suggested that convection, which is a result of the imbalanced hydraulic pressure at the two sides of the membrane,

accelerates electrolyte transport from catholyte to anolyte. Catholyte transport leads to (poly)iodide species crossover, which is known as the main reason of capacity fade. Insights into the underlying cause of capacity loss alluded to a potential solution involving manipulation of operating factors, i.e. adjusting electrolyte flow rates. Upon modifying the electrolyte flow rate ratios, a simultaneous decrease in the pressure drops of graphite felt electrodes, pipes, and flow channels were theoretically predicted, which could effectively lessen the total pressure drop within the cell stack. Aligned with the theoretical calculations, experimental investigations confirmed the successful suppression of catholyte transport and (poly)iodide crossover by establishing a counter-pressure. Consequently, an AC-ZIFB with catholyte to anolyte flow rate ratio of 1 to 7 was able to successfully achieve the highest reported cycle life of 1,100 cycles at a high current density of 80 $mA.cm^{-2}$. The valuable insight into the capacity fade mechanism and the suggested effective strategy offers a variety of RFB systems the ability to achieve their full potential as reliable, long lasting, and cost-competitive energy storage systems.

Chapter 5

Task-Specific Organic Additives for Robust Zinc-Iodine Redox Flow Batteries

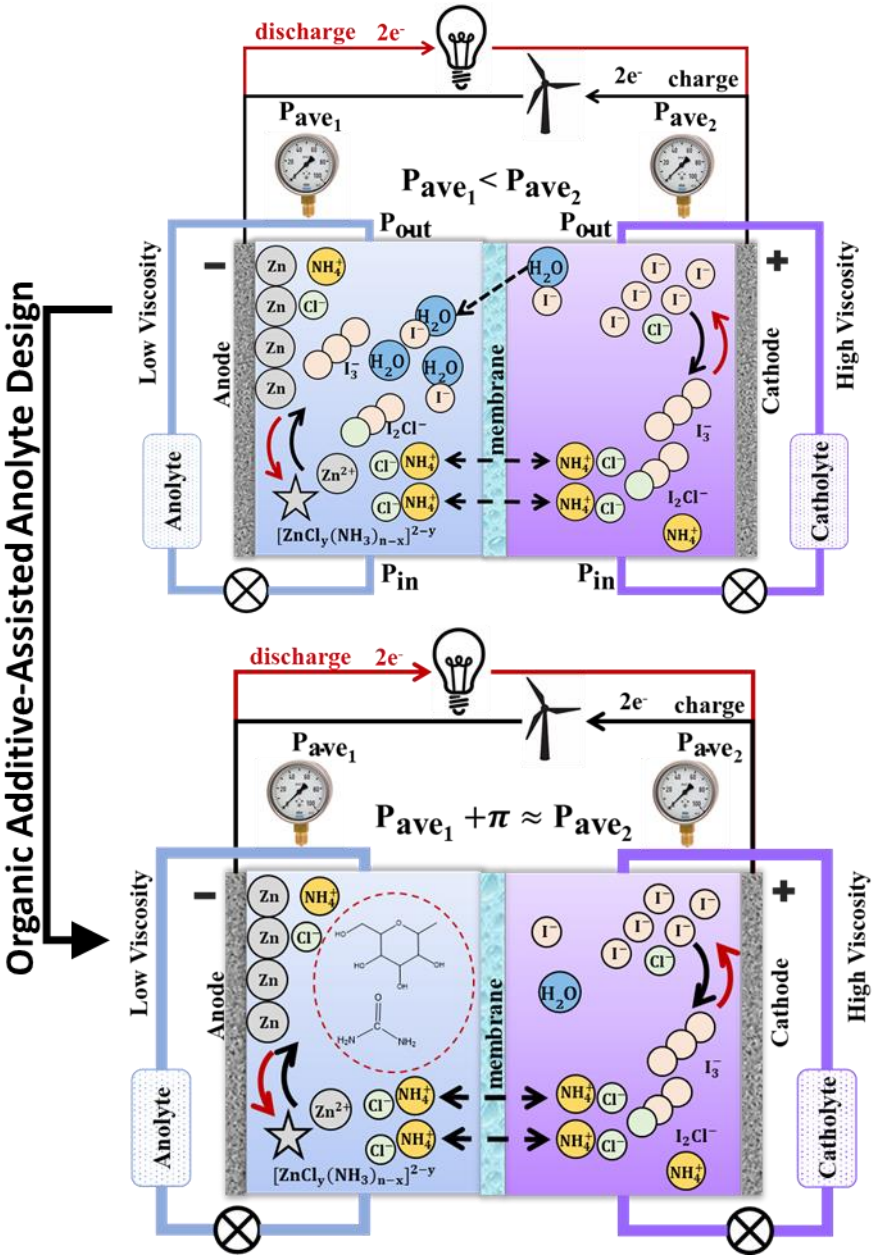

5.1 Introduction

Growing demand for intermittent renewable energy has brought extensive attention to redox flow batteries (RFBs), which are among the most promising types of large-scale energy storage systems due to their flexible energy and power output [8,14,69,121]. Among the viable RFB chemistry options, zinc-iodine redox flow batteries (ZIFBs) are of great interest due to their high energy density, fast redox reaction kinetics, and low environmental impacts [5,13,14,19,113]. Despite the aforementioned superiority, the issues with respect to the volumetric capacity, output power, electrochemical efficiencies, and the cost of the battery are still concerning. To advance the performance of ZIFBs, different electrolyte designs for ZIFBs have been reported and include modifying electrolyte design via modifying anolyte pH [16], integrating of complex-forming ions (bromide [15,17,94] and chloride [113]), and incorporation ammonium-based salts [113,122]. Regardless of the positive outcome from these electrolyte designs, the expensive Nafion membranes ($500-$700 m^{-2}), which are typically used to separate electroactive species in ZIFBs, still greatly restricts the economic viability for large-scale commercialization of ZIFBs [123–125]. Aside from their high cost, Nafion membranes suffer from high ionic resistance [34,42,45,126], leading to significant overpotential under high current densities and thus overall low power density of flow batteries. To avoid these disadvantages, non-fluorinated porous membranes have been developed as alternatives to Nafion membranes [127]. Particularly, porous polyolefin (PE) membranes are promising candidates owing to their low cost ($1-$20 m^{-2}) [60,113], high ionic conductivity [60], and excellent chemical stability in ZIFBs electrolytes [15,94,113]. However, the physical properties (viscosity and density) of the anolyte and catholyte in ZIFBs are mismatched, causing a severe disruption in the hydraulic pressure balance between the two sides of membrane [68]. This unbalanced hydraulic pressure eventually leads to fast capacity decay as a result of migration of the electrolyte [128,129] (and subsequently polyiodide active species) from the cathode to the anode side. Thus, the use of porous membrane in ZIFBs is limited because of the rapid

capacity decay and hence the poor cycle life. The challenge of extending the capacity relates to controlling electrolyte transport and crossover of active species through the porous membrane, and the need for customizing the electrolyte design to inhibit this unwanted catholyte transportation becomes critical [67].

Another way to balance the pressure in customized electrolyte designs for ZIFBs with porous membranes, additive can be introduced to the side with lower hydraulic pressure (i.e. anode side). Aside from balancing the hydraulic pressure, a tailored anolyte for ZIFBs requires cost, toxicity, and ionic resistance all to be minimum [130,131]. At the same time, the following advantageous features and properties are also preferred for the additive, such as improving zinc deposition efficiency, enhancing zinc redox reaction kinetics, having high solubility in aqueous solutions, and being compatible with zinc compounds. Organic compounds have been used widely for zinc electroplating [132], reducing nitrogen oxide emission [133], and wastewater desalination [134], due to their unique properties as brightening agents [132], selective catalysts [133], and draw solutes [134], respectively. In this regard, organic compounds can effectively be implemented in a pressure-balanced electrolyte design to alleviating capacity decay and improving the cycle life of ZIFBs.

In the present study, additive-supported anolytes were designed to inhibit catholyte transportation through the membrane, improve cycle life, and enhance electrochemical performance of AC-ZIFBs. To best demonstrate the mechanism and benefits from such a design, we focused on two well-known, low-cost, and organic compounds: urea (\$1.3-\$1.8 kg^{-1}) and glucose (\$1-\$5 kg^{-1}). These organic compounds were deliberately chosen to study the effect of additives in balancing hydraulic pressure because of their high solubility, high viscosity and density of their aqueous solution , and minimal effect on the total electrolyte cost [135]. The electrolyte transport, cycle life, and energy efficiency of AC-ZIFBs with new design were investigated. The results exhibited that the addition of both compounds can improve the cycle life by inhibiting the electrolyte transport to some extent. However, urea was less

effective in inhibiting catholyte migration and capacity loss, while the glucose-supported anolyte presented more stable electrochemical performance. In addition, both additive supported ZIFBs presented higher voltage and energy efficiency than the pristine one. To investigate the additives contribution in electrochemical performance, their effect on zinc redox reaction kinetics and deposition efficiency was also evaluated. The exchange current density of zinc reaction was improved by 15% and 20% by implementing urea and glucose, respectively. The addition of glucose and urea also lead to 99.7% and 99.5% current efficiency for zinc deposition. As a result of introducing multi-functional additive, the AC-ZIFBs with customized anolyte (1.5 M glucose-2.5 M zinc chloride-2.5 M ammonium chloride) successfully demonstrated over 300 charge-discharge cycles at 50% state-of-charge (SOC) and 80 mA cm^{-2}, revealing that the transport of water and (poly)iodide active ions were effectively limited. The breakthrough strategy of using multi-functional additives in anolyte chemistries combined with decoupled electrolyte arrangement and low-cost porous membranes paves a new path towards solving the issue of pressure-dependent active ion crossover and moves the field of energy storage a step closer to achieving robust and large-scale RFBs integrated with renewable energy systems.

5.2 Materials and methods

5.2.1 Flow battery Assembly

The construction of AC-ZIFB single cells was described in detail in previously published paper [16]. The flow cells were fabricated by sandwiching Daramic microporous polyethylene (PE) membranes with pore size, porosity, and the thickness of 0.15 μm, 57%, and 900 μm, respectively, between two pieces of heat-treated graphite felt (area of 9 cm^2, H-GF, SGL Carbon Group, Germany) embedded graphite plates. The graphite felt was thermally treated in an air atmosphere at 500◦C for 2 hours. The positive electrolyte was a 10 mL aqueous solution of 5 M ammonium iodide ($NH_4I \geq 99\%$, Aldrich) with 2.5 M ammonium chloride ($NH_4Cl \geq 99.5\%$, Aldrich) as supporting electrolyte, and the negative

electrolyte was a 10 mL aqueous solution of 2.5 M zinc chloride ($ZnCl_2 \geq 98\%$, Aldrich) with 2.5 M ammonium chloride ($NH_4Cl \geq 99.5\%$, Aldrich) as supporting electrolyte. Urea ($NH_2CONH_2 \geq 99\%$, Aldrich) and α-D-Glucose ($C_6H_{12}O_6 \geq 96\%$, Aldrich) with various concentrations were added to the anolyte as organic compound additives. The ZIFB with Nafion membrane was fabricated in the same set up by sandwiching a Nafion 117 membrane (N117) between two pieces of H-GF for EIS measurements. N117 underwent a sequential pre-treatment in the following boiling solutions for 1 h each: 3% H_2O_2, DDI water, 0.5 M H_2SO_4 and DDI water.

5.2.2 Electrochemical Characterization

The charge-discharge tests were conducted on a potentiostat/galvanostat (Land Electronic Co., Ltd., Wuhan) with a voltage cut-off range of 0.6-1.6 V at a constant current density of 80 mA cm^{-2}. To compare the flow cells on an equal basis, all polarization tests were carried out at state-of-charge (SOC) of 50%. The electrochemical impedance spectroscopy (EIS) of full-cell flow batteries were carried out in potentiostatic mode using a Gamry impedance analyzer over a frequency range from 1 MHz to 0.2 Hz and a 0.01 V sinusoidal perturbation amplitude. Before each measurement, the flow cells were allowed to rest for 2 min at their open circuit voltages (OCVs).

Electrochemical measurements for half-cell investigation were conducted using an electrochemical workstation (Biologic VSP 300). A platinum wire, glassy carbon electrode (GCE, 0.196 cm^{-2}) and Ag/AgCl electrode were chosen as the counter, working and reference electrodes, respectively, in a three-electrode configuration. A mixed solution of 0.5 M $ZnCl_2$ and 0.5 M NH_4Cl were selected as the blank solution, and the addition of 0.1 M of urea and 0.1 M glucose to the blank solution were also studied. All solutions were studied at room temperature using a static GCE at a scan rate of 20 mV s^{-1} and a potential sweep from 0 V to -1.2 V (vs Ag/AgCl) to deposit the zinc metal at the surface of GCE, followed by a sweep back to 0 V, which produced an anodic peak. The effect of additives on

zinc deposition kinetics was studied using Tafel plots by scanning the potential in the OCV±250 mV range at a sweep rate of 2 mV s^{-1}. To calculate the exchange current density (i_0), anodic (β_a), and cathodic Tafel slopes (β_c), the Butler-Volmer equation was fitted to the experimental data.

5.3 Results and discussion

5.3.1 Electrochemical Performance

The electrolyte volume and electrochemical performance of the flow cells with additive-supported anolyte design were studied under heavy duty cycling to determine if the additives could inhibit excessive catholyte migration and stabilize the electrochemical performance over longer periods of operation. All cells were cycled at 80 mA cm^{-2} current density and charged to 50% SOC (37 minutes charge) for a justified comparison. The AC-ZIFBs was first charged and discharged with no organic compound additives to obtain the controlled performance. The water displacement was closely monitored and evaluated by measuring the electrolyte volumes of the anolyte and catholyte sides, as shown is shown in Figure 5.1a. The observed electrolyte volume changes during cycling in the baseline flow cell were drastic, leaving almost no electrolyte left on the cathode side after the short cycling test. Then, the addition of 0.1 M urea or 0.1 M glucose in the anolyte was examined. The urea-supported anolyte was able to moderately decrease the rate of catholyte transport, resulting in a less drastic change of electrolyte volume compared to the baseline flow cell. However, this rate of catholyte transport is likely not suitable for heavy duty cycling, since the catholyte was depleted relatively quickly. However, the 0.1 M glucose-supported anolyte significantly improved the electrolyte volume stability over the long-term cycling, with no electrolyte displacement detected until after 50 cycles, suggesting that glucose-assisted AC-ZIFBs can feasibly be used for long cycling applications.

The Coulombic efficiency (CE), voltage efficiency (VE) and energy efficiency (EE) of the flow cells were also measured and are presented in Figure 5.1b, c and d, respectively. Note that the cycle life is

defined here as the number of cycles where charging to 50% SOC was possible. The CE of all flow cells were similar over the first three cycles with urea and glucose-assisted cells showing higher CE initially. However, as the cycling proceeded, the glucose-supported cell displaying the best CE retention while the CE of the control AC-ZIFB decreased appreciably. From this result, it can be concluded that the organic compound additions did not have any detrimental effects on zinc redox reactions in the flow cells, and in fact could improve the CE stability.

While the cycle life resulting from the control/pristine anolyte is short-lived (12 cycles, Figure 5.1b), the urea-supported anolyte showed minor improvement (30 cycles, Figure 5.1c) since the depletion of catholyte was slightly delayed. Nevertheless, this cycle life is still considered unacceptable for practical application. However, when glucose was employed, stable electrochemical performance with ~75% EE is observed throughout 100 cycles (Figure 5.1d), mainly due to the insignificant volume change during the cycling experiment. Thus, while the employment of both organic compounds can verify the initial assumption that more balanced hydraulic pressure can lead to improved cycling performance, glucose offers the most promising electrochemical stability.

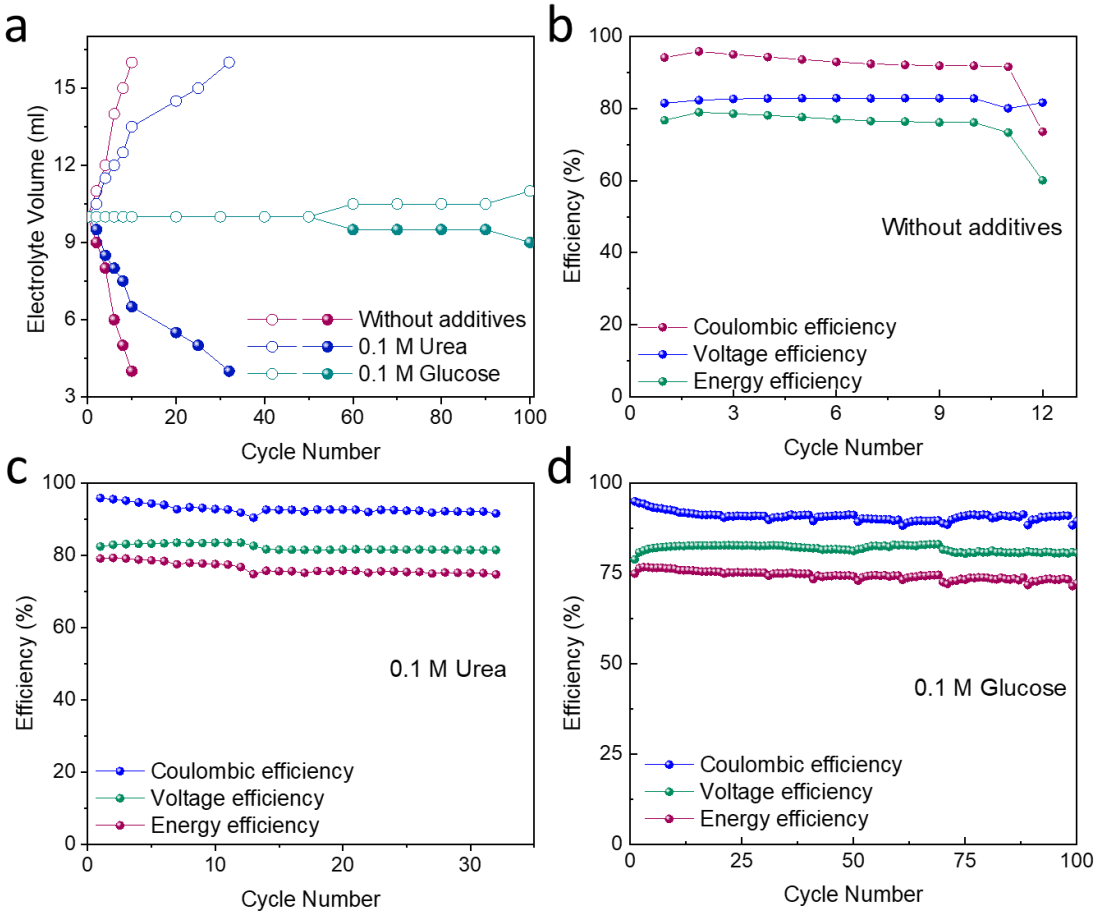

Figure 5.1. Water transport and electrochemical performance of organic additive-supported AC-ZIFBs. a) Volume of anolyte and catholyte over cycling. CE, VE and EE of the AC-ZIFBs with b) no organic compounds, c) 0.1 M urea and d) 0.1 M α-D-Glucose, with 5 M I^- and 2.5 M Zn^{2+} catholyte and anolyte compositions under current density of 80 mA cm^{-2} and 50% SOC.

5.3.2 Full-cell Polarization and EIS Measurements

To analyze the losses in flow cells and identify the dominant limitations in their performance, their polarization curves with associated cell resistance were studied. Figure 5.2a shows the polarization curve results for AC-ZIFBs with and without urea and glucose additives. The OCVs of all three systems were very close to the theoretical value that was reported in our previous work (~1.3 V) [113]. From the polarization curve, cell voltage follows the same trend and in both pristine and additive based AC-ZIFBs. The drop in cell voltage is associated with three regions: I) kinetic losses, associated with

electrode polarization, II) iR losses, associated with contact and ionic resistances, and III) mass transfer-limiting currents associated with the delivery of bulk reagent to the electrode. Minor kinetic polarization with ~0.010, 0.007, and 0.005 V drop at 10 mA cm^{-2} were exhibited in pristine, 0.1 M urea-supported, and 0.1 M glucose-supported AC-ZIFBs, respectively. Meanwhile, the kinetic and ohmic overpotentials are the predominant contributors to the voltage loss at lower current densities. The cell voltage of the systems begins to rapidly drop at current densities above 80 mA cm^{-2}, which identifies the point that mass transport starts to affect the flow cell performance. At a glance, the polarization curve of AC-ZIFBs with additives start to deviate from the pristine curve at current densities above 10 mA cm^{-2} (the end of the region I) by exhibiting higher cell voltage at all current densities. This result is likely attributed to the lower resistance of the flow cells with organic compound additives. In general, the losses due to electrode kinetics and mass transport issues have been proven to be minimal compared to iR losses in RFBs [136].

The electrochemical impedance spectroscopy (EIS) of full-cell flow batteries were carried out over a frequency range from 1 MHz to 0.2 Hz and a 0.01 V sinusoidal perturbation amplitude at 0% SOC, where the area-specific resistance (ASR) was obtained by using the high-frequency intercept of the electrochemical impedance spectrum at a given polarization [137]. From the Nyquist impedance plots in Figure 5.2b, the ASR of AC-ZIFBs without additives, with 0.1 M urea, and with 0.1 M glucose were found to be 2.79, 1.91, and 1.09 Ω cm^2, respectively. Although the ASR values of AC-ZIFBs based chemistries have not been reported in the literature for comparison, the ASR of all three systems is much less than other aqueous-based RFBs with Nafion membranes [138]. The EIS measurements of the pristine AC-ZIFBs with Nafion 117 membranes were also conducted and presented in Figure 5.3 for comparison. Overall, these results show that compared to ZIFB with Nafion 117 (ASR of 11.5 Ω cm^2), implementing PE membrane could substantially decrease the ASR of flow cells, and the addition of glucose can further improve the ionic conductivity and reduce resistance.

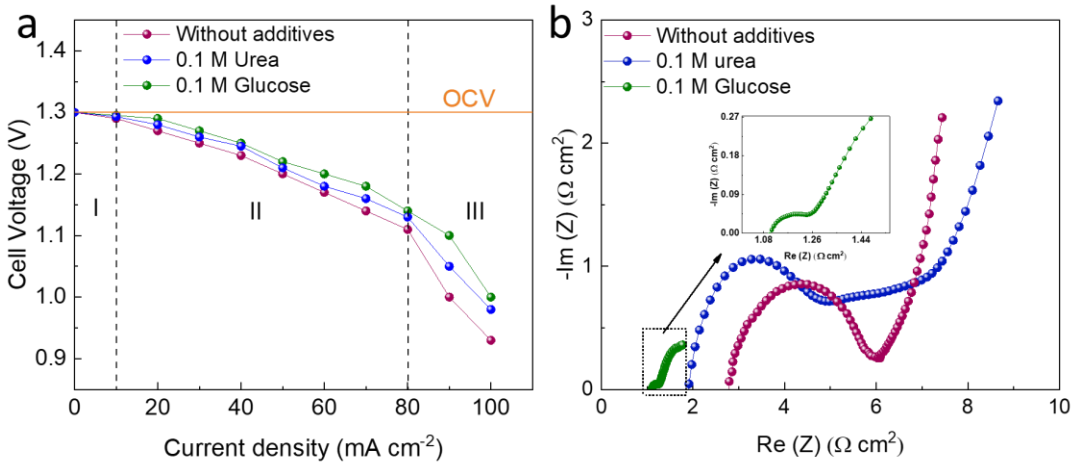

Figure 5.2. Full-cell polarization and EIS measurements of AC-ZIFBs. a) Discharging polarization curves, and b) EIS of AC-ZIFBs with and without additives with 5M I^- and 2.5 M Zn^{2+} catholyte and anolyte compositions.

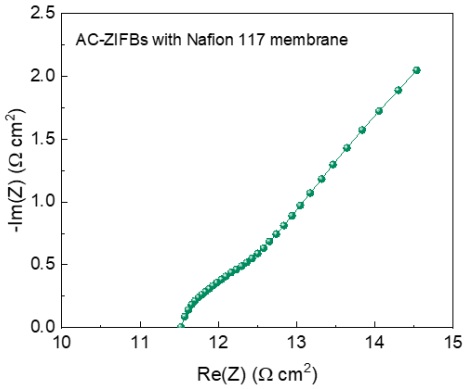

Figure 5.3. The EIS results of AC-ZIFBs with 5M I^- and 2.5 M Zn^{2+} catholyte and anolyte compositions.

The rate capability of the AC-ZIFBs with the proposed anolyte design was determined with the current density range varying from 20 to 100 mA cm^{-2}(Figure 5.4). In agreement with the EIS results, the higher ohmic resistance and electrochemical polarization of pristine AC-ZIFBs resulted in lower VE at different current densities. Meanwhile, addition of urea and glucose improved the VE and EE,

especially at higher current densities, which is evidence of their excellent power density. However, the glucose-supported flow cell showed more stable electrochemical performance during the whole current density range and overall outperformed the urea-supported AC-ZIFBs.

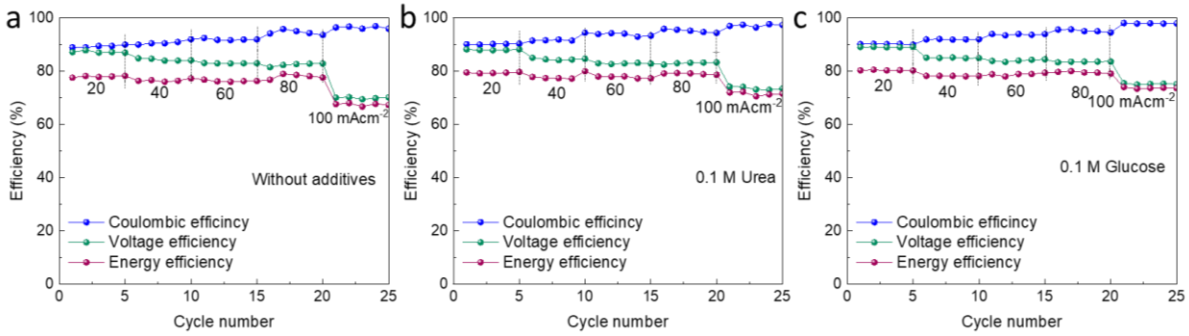

Figure 5.4. Rate capability of AC-ZIFBs a) without additives, b) with 0.1 M urea, and c) with 0.1 M α-D-Glucose, with 5M I^- and 2.5 M Zn^{2+} catholyte and anolyte compositions.

5.3.3 Evaluation of Contribution Factors in Electrochemical Performance

Cyclic voltammograms were obtained for 0.5M $ZnCl_2$ + 0.5M NH_4Cl blank solution and 0.5M $ZnCl_2$ + 0.5M NH_4Cl with 0.1 M of urea and glucose additives at a scan rate of 20 mV s^{-1}(Figure 5.5a). According to the CV curves, zinc deposits at the surface of glassy carbon electrode (GCE) below approximately -0.85 V (vs. Ag/AgCl), and a nucleation loop was produced at the end of the cathodic scan. Anodic peaks appeared at approximately -0.40 and -0.43 V (vs. Ag/AgCl) in blank and with additive solutions, respectively, at the reverse scan. The anodic peaks represent Zn^{2+} stripping from deposited zinc at the cathodic scan. The nucleation overpotential (NOP) was calculated by measuring the difference between the potential at which cathodic current is first observed and the potential at which the current switches from cathodic to anodic during the reverse scan (crossover potential).

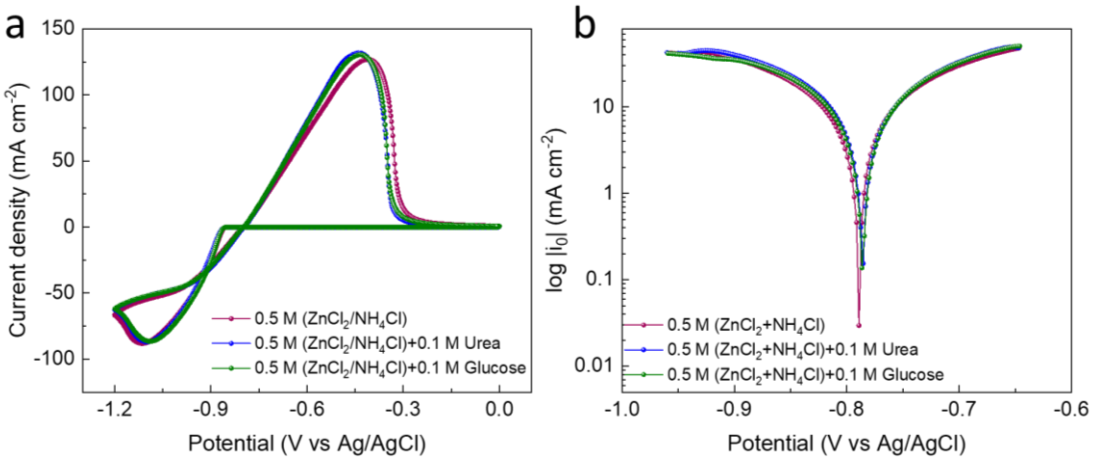

Figure 5.5. Half-cell study of zinc redox reaction in different anolyte compositions. a) Cyclic voltammograms of different anolyte composition on a glassy carbon electrode (GCE) at scan rate of 20 mV s^{-1}. b) Semi-log plot of current density vs potential on a GCE at a scan rate of 2 mV s^{-1}

The data extracted from the CVs (Table 5.1**Error! Reference source not found.**) indicated that the addition of urea and glucose could slightly decrease the nucleation overpotential (NOP), which indicates a minor improvement in the reversibility of the zinc plating and dissolution reactions and subsequently benefits the VE for flow-cells with additives. In addition, from the CV tests, the solution with 0.1 M urea slightly decreased the Coulombic efficiency (CE) for zinc deposition/dissolution, while 0.1 M glucose additives showed an increased 99.7% CE, indicating positive effect of glucose on the zinc redox reaction. Therefore, the glucose-supported anolyte solution displays promising properties in both maintaining the cathodic polarization and increasing the CE.

Table 5.1. Effect of organic additives on E_{nu}, Q_{an}, and CE of zinc deposition.

Anolyte composition	E_{nu} (V)	-NOP(mV)	Q_{an} (mA s)	CE (%)
0.5 M ($ZnCl_2$/NH_4Cl)	-0.85	48	208.2	99.5
0.5 M ($ZnCl_2$/NH_4Cl) + 0.1 M Urea	-0.84	47	203.5	99.1
0.5 M ($ZnCl_2$/NH_4Cl) +0.1 M Glucose	-0.84	46	206.8	99.7

The effect of additives on the Zn^{2+}/Zn kinetics were also investigated by polarization experiments (Figure 5.5b). According to the extracted data from Tafel plot in Table 5.2, minor increase in Tafel slopes in cathodic and anodic regions were found upon addition of urea and glucose. This indicated that the addition of these additives had negligible effects on the reaction mechanism of zinc deposition and dissolution. However, the exchange current density (i_0) of zinc reaction increased by 15% and 20% upon addition of urea and glucose, respectively, meaning that these additives facilitate charge transfer between the zinc metal cation and electrode surface.

Table 5.2. The calculated kinetic parameters of zinc reaction from Tafel plots of different anolyte compositions

Anolyte composition	E_{ocp} (V)	I_0 (mA cm^{-2})	β_a (mV)	β_c (mV)
0.5 M ($ZnCl_2$/NH_4Cl)	-0.793	11.65	227	212
0.5 M ($ZnCl_2$/NH_4Cl) + 0.1 M Urea	-0.789	13.42	227	229
0.5 M ($ZnCl_2$/NH_4Cl) +0.1 M glucose	-0.786	13.93	234	277

5.3.1 Electrochemical Performance of AC-ZIFB with Glucose Additives

Given that the glucose addition was found to deliver stable electrochemical operation, we conducted further investigations to determine its full capability to mitigate electrolyte crossover and understand the corresponding mechanism by testing different solute concentrations. To study the extent of capacity decay, with 0.1 M, 0.5 M and 1.5 M glucose were investigated with longer cycling times (Figure 5.6). The electrochemical performance and specific volumetric capacity of the cells were studied by cycling at 80 mA cm^{-2} with charging to 50% SOC unless the 1.6 V cut-off limit was reached first. As shown in the plots, the CE, VE and EE of the cells were mainly stable over long cycling periods with only slight variations (Figure 5.6a,b and c). However, by increasing the concentration of glucose in the anolyte

design, the cycle life using 50% SOC charging increased from 100 cycles for 0.1 M to 150 and 300 cycles for 0.5 M and 1.5 M, respectively (Figure 5.6d,e,f). This trend of decreased or delayed capacity losses is likely explained by higher glucose concentrations allowing lower amounts of iodide/polyiodide species migration from the catholyte to the anolyte for each cycle. After the first 100 cycles with 50% SOC charging, the flow cell with 0.1 M glucose experienced gradual capacity loss over the remaining 80 cycles until it was only capable of discharging approximately 25% SOC (Error! R eference source not found.d).

The same trend was observed when 0.5 M glucose was introduced to the anolyte with capacity loss mainly occurring over the last 150 cycles (Figure 5.6e). However, for the 1.5 M glucose-supported anolyte, 50% SOC was maintained for approximately 300 cycles before the capacity decreased sharply to 25% SOC (Figure 5.6f). Although the rate of capacity decay can be alleviated significantly by this strategy, the non-equilibrium transfer of water and iodide ions still occurs, ultimately leading to electrolyte imbalance. The onset of fast capacity degradation in all three concentrations corresponded closely with the observed onset of rapid catholyte transport to the anolyte side (Figure 5.6g,h,i). The improvement in cycle life at 50% SOC therefore verifies that reactant crossover was reduced in higher concentration, enabling the system to achieve much-improved capacity-retention capability.

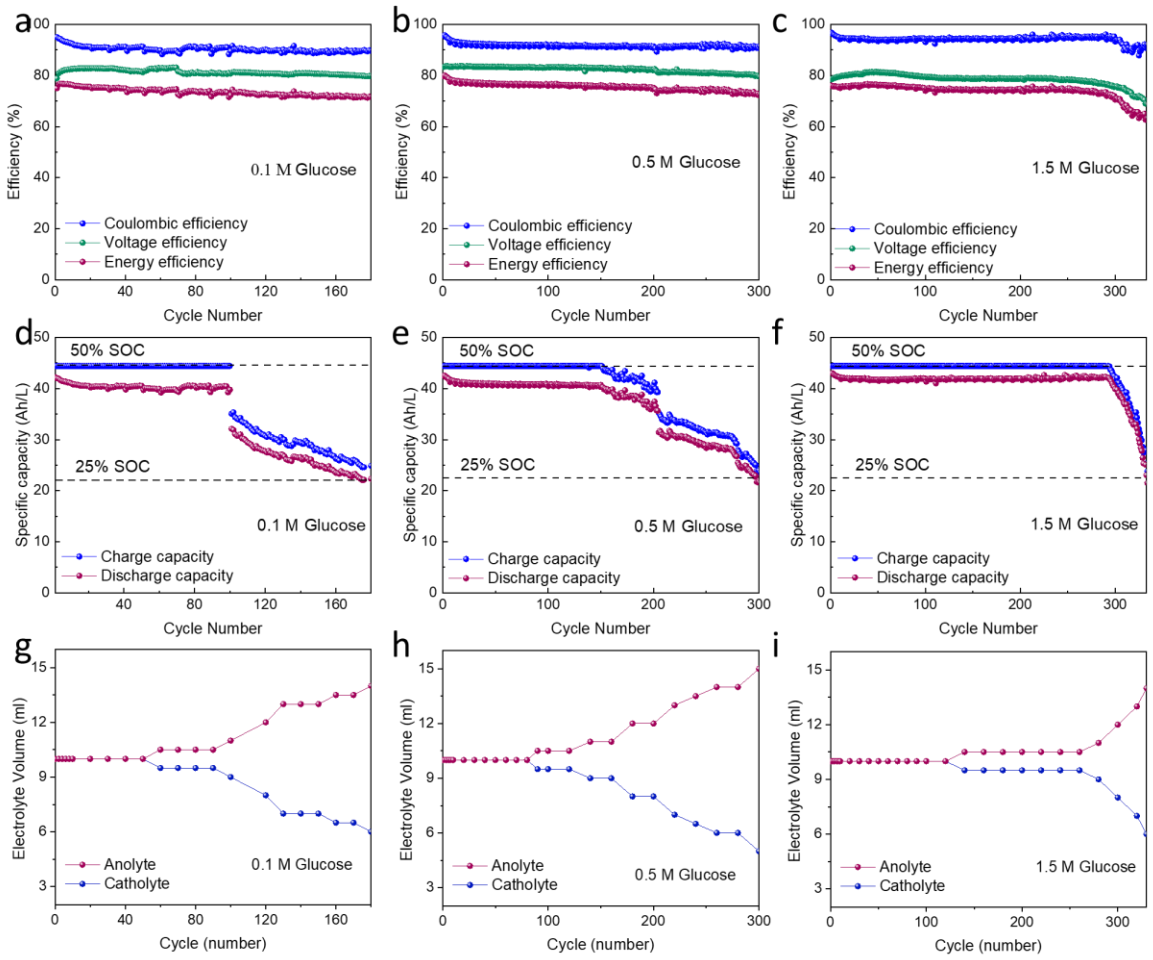

Figure 5.6. Electrochemical performance and water transport of glucose-supported zinc-iodine redox flow batteries during long-term cycle operation. Cycling performance of glucose-supported AC-ZIFBs with 5 M I^- catholyte and 2.5 M Zn^{2+} anolyte in terms of CE, VE and EE under current density of 80 mA cm^{-2} with a) 0.1 M, b) 0.5 M, and c) 1.5 M glucose. Specific capacity of the flow cell with d) 0.1 M, e) 0.5 M, and f) 1.5 M glucose. Volume of anolyte and catholyte of the cell over cycling with g) 0.1 M, h) 0.5 M and i) 1.5 M glucose.

5.3.2 Mechanism of Organic Compound Additives in Alleviating Capacity Fade

The mechanism of capacity decay in AC-ZIFBs with PE-porous membranes is schematically represented in Figure 5.7. Under ideal operation, only supporting ions (NH_4^+ and Cl^-) exchange between the two electrolytes to maintain charge neutrality; however, unwanted active species and solvent

passage between the electrolytes are inevitable due to the imperfect selectivity of the porous membrane [114]. The electrolyte transport can be more drastic if significant pressure imbalance exists between the two sides. The average hydraulic pressure (P_{ave}) of the anolyte or catholyte side can be calculated as $P_{ave}=\frac{P_{in}+P_{out}}{2}=P_{out}-0.5\Delta P$, where P_{in} is the inlet pressure, P_{out} is the outlet pressure and ΔP is the difference between P_{in} and P_{out} [68]. Generally, the catholyte of AC-ZIFBs experiences higher average hydraulic pressure than the anolyte due to the difference in their physical properties, including viscosity and density. This unbalanced hydraulic pressure acts as the driving force for convection, leading to collective movement of (poly)iodides coupled with water through the porous membrane to the anode side. The leakage of (poly)iodides can contribute to capacity decay by (i) chemical reaction with the deposited zinc at the surface of the negative electrode, and (ii) accumulation of (poly)iodide ions at the anode side, making them unavailable for electrochemical reaction at the cathode side. The water flux and (poly)iodide crossover, and corresponding capacity decay, could be alleviated by imposing an extra pressure in the reverse direction.

Upon addition of the organic compounds, the water flux and (poly)iodide crossover, and corresponding capacity decay, can be alleviated. Based on previous discussion, the anode side experiences less hydraulic pressure than the cathode side. Therefore, the addition of organic compounds could have compensated for the lower hydraulic pressure at the anode side by increasing its average pressure. As a result, a closer pressure balance between the two sides is maintained and the catholyte transport and (poly)iodide crossover is inhibited. The proposed mechanism of (poly)iodide crossover inhibition in new anolyte design is demonstrated in Figure 5.7b,c. A positive value (ΔP) could be added to the side with lower average pressure (i.e. anode) due to an apparent reduction in pressure drop by dissolving the organic compound additives. By the aid of this imposed counterbalancing pressure, the pressure difference across the two sides of the membrane can be reduced and less change of the electrolyte volume during the battery operation is expected.

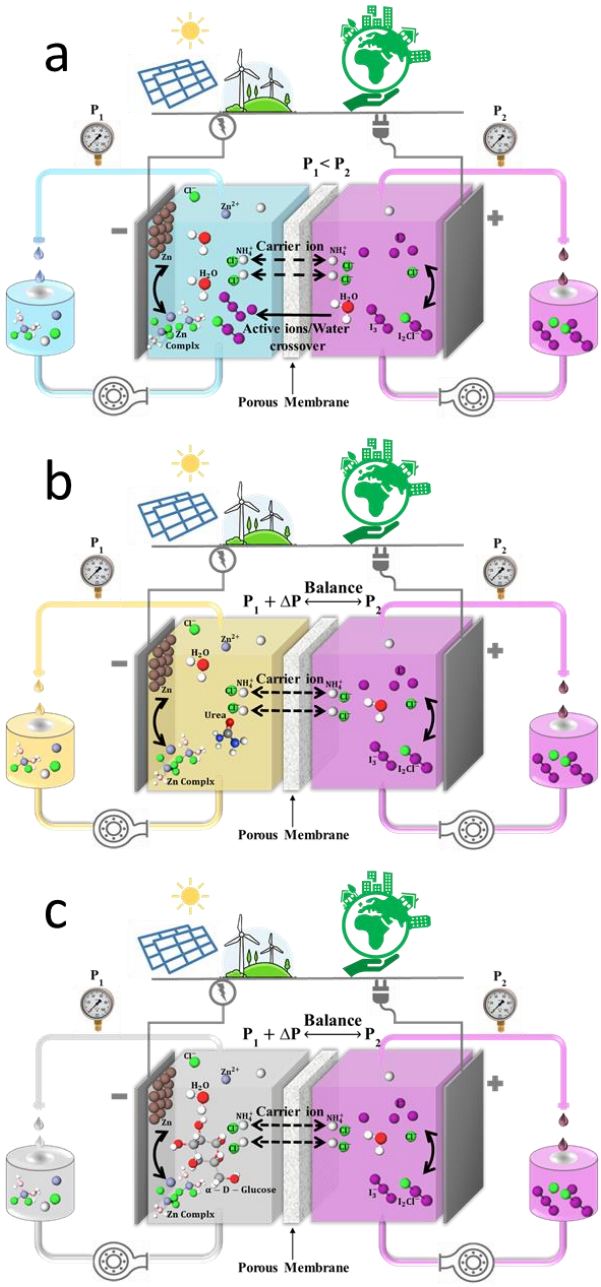

Figure 5.7. Schematic of the mechanism of capacity decay in AC-ZIFBs by (poly)iodide active ion crossover due to the unbalanced hydraulic pressure inside the cell stack. A) The pristine AC-ZIFBs, the AC-ZIFBs with b) Urea, and c) Glucose

The electrochemical performance of urea and glucose-supported flow cells showed that the addition of glucose is more effective for extending the cycle life. The reason for such behavior can be explained

through how these organic compounds function. There are two competing functions contributing to the effectiveness of these additives in AC-ZIFBs: the hydraulic pressure they create in the forward direction and their reverse flux in the opposite direction [135]. While the hydraulic pressure associated with addition of organic compounds to anolyte can alleviate the electrolyte crossover, the reverse flux of the compounds from anolyte to catholyte resumes the unbalanced pressure at two sides of membrane. Reverse permeation of organic compounds through the membrane eventually happens as a direct consequence of organic compound concentration difference across the membrane [135]. However, if the reverse flux of an additive happens fast, it can quickly diminish the effective osmotic pressure difference across the membrane, thus reducing the effectiveness of forward osmosis and in turn the cycling stability of the AC-ZIFBs. Glucose have been reported to have higher viscosity and density than urea at the same weight ratios [133,139]. Consequently, adding glucose to anolyte can more effectively balance the hydraulic pressure at two sides of membrane. Moreover, the permeability coefficient of glucose in commercial asymmetric cellulose triacetate (CTA) membranes is reported to be lower than urea [135]. This might be attributed to the larger size of glucose (8.6×8.4 Å for [140]) compared to urea (3.0×4.97×5.34 Å [141]). Thus, while both organic compound-supported electrolyte designs are likely to alleviate capacity decay and improve cycle life and electrochemical performance, the positive effect from glucose lasts longer than urea. With higher concentration of glucose, the hydraulic pressure of anolyte is higher, meaning that the catholyte transport can more effectively be alleviated. However, since the difference in concentration of glucose between the two sides of the membrane is also higher, higher reverse flux rate from anolyte to catholyte is expected. The balance between these two forces could determine when excessive catholyte transport happens.

5.3.3 Feasibility of AC-ZIFBs with Organic Additives-Supported Anolyte Design

To demonstrate the potential economic viability of the new design, techno-economic analyses were conducted based on the Darling model [99,100,113]. To rationally compare the cost of storage on an equal basis [99], the cost of energy (US$ kWh^{-1}) can be calculated as the ratio of the power cost (US$ kW^{-1}) to total storage duration (h) in a log-log plot of installed cost versus energy/power ratio (E/P). The resulting log-log plot is presented in Figure 5.8a, with the details of the calculation method presented in Appendix D. Since the major difference among cost contributions in these systems is the cost of additives to the anolyte, AC-ZIFBs with additives will have higher chemical costs. However, thanks to improved electrochemical performance upon addition of both additives, the energy cost of the AC-ZIFBs with 0.1 M urea and 0.1 M glucose decreased by 5% and 6%, respectively. In addition, due to the low cost of glucose, even the addition of higher concentration of Glucose showed minor effect on the discharge time necessary for the system to meet the DOE cost target of 150 US$ kWh^{-1} by the year of 2023 [28,113]. The installed cost of a 1.5 M glucose-supported AC-ZIFB with low-cost membrane could fall below 150 US$ kWh^{-1} with just a 6 h discharge time. The cost, cyclability, and EE comparison of the flow cells tested at 50% SOC under current density of 80 mA cm^{-2} are presented in Figure 5.8b. The flow cells with additives demonstrate highly improved cyclability compared to the pristine one, while the overall cost of the systems is nearly identical. Considering all five aspects of the radar plot, the AC-ZIFBs with 1.5 M glucose-supported anolyte is highlighted to be the most promising ZIFB system.

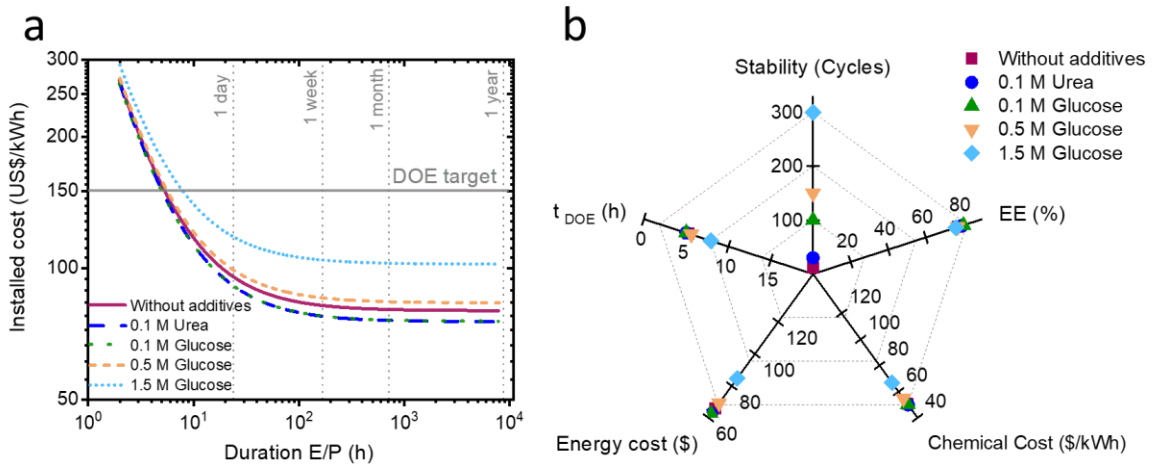

Figure 5.8. Summary of techno-economic analysis and electrochemical performance for AC-ZIFB system with and without additives. A log-log plot of installed cost versus storage duration for AC-ZIFB without additives and with 0.1 M urea, 0.1 M, 0.5 M, and 1.5 M glucose concentration in the anolyte. The gray solid line represents the DOE target for 2023. b) Comparison of the systems in terms of stability, energy efficiency, chemical and energy costs, and the discharge time necessary for each to meet the DOE cost target of 2023 (t_{DOE}).

5.4 Summary

In summary, a new anolyte design with organic task-specific additives (urea and glucose) for zinc-iodine redox flow batteries with polyolefin-based (PE) microporous membranes were proposed and fabricated. The effect of additives on zinc redox reaction kinetics and deposition efficiency showed that the exchange current density of zinc reaction was improved by 15% and 20% upon introducing urea and glucose, respectively, with additional advantage of 99.7% current efficiency of zinc deposition in glucose-supported anolytes. Both additives exhibited improvement in enhancing the cycle life of the flow batteries, while glucose was much more effective than urea. Employing this novel design, the zinc-iodine redox flow batteries with glucose (US$1-US$5 kg^{-1})-supported anolyte achieved outstanding Coulombic efficiency of ~95%, energy efficiency of ~78%, and a cycle-life of 300 cycles at 50% SOC and 80 mA cm^{-2} with a cost below 150 US$ kWh^{-1} in discharge times of just 8 h or greater, confirming the practicability and reliability of the system. Such performance and cyclability

improvements were mainly due to alleviating the electrolyte transport and capacity decay of the ZIFBs when glucose is employed in the anolyte design, especially at 1.5 M concentration. This organic compound was strategically implemented to effectively limit the permeation of water and (poly)iodide active ions by balancing the hydraulic pressure on the two sides of the porous membrane. By cost-effectively delivering balanced hydraulic pressure, this straightforward and impactful strategy of employing additives is expected to be a feasible method for bringing robust and economical RFBs to the grid-scale energy storage market.

Chapter 6
Conclusions and Future work

6.1 Conclusions

This thesis investigated new electrolyte and membrane design for durable, high energy density, cost-effective zinc-iodine redox flow batteries (ZIFBs). The studies were divided into three parts to fulfill the thesis objectives. Earlier in **Chapter 3**, a decoupled multifunctional NH_4Cl supported electrolyte was designed in ammonium-based zinc-iodine redox flow batteries (AC-ZIFBs). The new electrolyte design was beneficial in several aspects. Firstly, the cycle life was substantially improved as a result of NH_4Cl primarily facilitating zinc deposition and suppressing zinc dendrite formation at the anode. Secondly, the NH_4Cl addition enhanced capacity owing to the beneficial effects of both NH_4^+ and Cl^- ions. Thirdly, the excellent performance and cyclability were maintained independent of the charge/discharge state, which demonstrate the flexibility of the electrolyte. Lastly, the installed cost of the flow battery system was dramatically reduced by utilizing low-cost ammonium salts in a decoupled electrolyte, instead of the moderately costly zinc iodide (ZnI_2) in the conventional design. Overall, this zinc-iodine system demonstrates a new design with a promising performance. However, replacing costly Nafion membrane with an alternative low-cost membrane has received relatively little attention in the literature, which provided the motivation for the experimental investigations in **Chapters 4** and **Chapter 5** of the thesis.

In **Chapter 4**, the costly Nafion membrane were replaced by an alternative low-cost membrane to overcome both performance and cost challenges that AC-ZIFBs were faced towards their penetration in broad market. Thus, AC-ZIFBs with low-cost porous polyolefin-based (PE) membranes was designed. First, the mechanism of capacity fading with PE membrane was investigated, and the insight into the underlying cause of capacity loss alluded to a potential solution. It was observed that

(poly)iodide significantly crossed through the porous membrane as water moved from catholyte to anolyte. This process resulted in poor performance and a significant loss in capacity. Next, the adjusting electrolyte flow rates solution was optimized using theoretical calculations and verified with experimental testing. Convection, which results from electrolytes hydraulic pressure differentials at the two sides of the membranes, was considered to have a dominant effect on capacity fade over cycling. An optimum flow rate ratio of 1:7 (catholyte: anolyte) was theoretically determined to balance the pressure difference induced by changes in viscosity of the two sides of the membrane, which proves its effectiveness experimentally to remediate capacity by suppression of water flux and (poly)iodide crossover by establishing a counter-pressure to reduce the pressure gradient between the two sides of the flow cell.

Finally, **Chapter 5**, organic additives (urea and α-D-Glucose) for zinc-iodine redox flow batteries with porous polyolefin (PE) membranes were proposed and fabricated. Both additives could enhance the cycle life of the flow batteries, while α-D-Glucose (US$1-US$5 kg^{-1}) was more functional than urea. The sweet zinc-iodine redox flow batteries (SAC-ZIFBs) with 1.5 M α-D-Glucose supported anolyte achieved Coulombic efficiency of ~95%, energy efficiency of ~78%, and a cycle-life of 300 cycles at 50% SOC and 80 mA cm^{-2} with a cost below 150 US$ kWh^{-1} in discharge times of just 8 h or greater. The zinc redox reaction kinetics and deposition efficiency studies showed 15% and 20% improvement in the exchange current density of zinc reaction upon introducing urea and α-D-Glucose, respectively. Additionally, α-D-Glucose-supported anolytes exhibited 99.7% current efficiency of zinc deposition. Alleviating the electrolyte transport and capacity decay of the SAC-ZIFBs when α-D-Glucose is employed in the anolyte design was suggested as main reasons for such performance and cyclability improvements.

6.2 Future Work

Based on the results from the studies conducted in this thesis research, the following recommendations are proposed for future work.

1. Conducting fundamental in-situ and ex-situ experiments to obtain further understanding of the performance decay and capacity fade.

The ex-situ qualitative and quantitative analysis of cell stack components (PE porous membrane and graphite felt electrodes) before and after cycling could provide further insight into the morphological, crystallographic, and surface chemistry changes resulting from the electrochemical operation. Raman spectroscopy and XPS analysis are suggested to track down the formation of resistive films at positive and negative electrodes as well as the composition of the films and their contribution to the loss of electrodes surface area. XRD analysis is also suggested to evaluate electrode and membrane aging rates in the presence of corrosive iodine electrolyte during cycling. The in-situ characterization of electrolytes is also an invaluable approach to gain a better understanding of performance decay. The reference electrodes can be inserted into the positive and negative electrolyte for in-situ analysis to identify and corroborate activation overpotential in each half-cell during battery cycling.

2. Investigation on fundamental solution chemistry of other additives for RFB applications.

Several categories of additives including charged compounds, ionic liquids (ILs), and low-molecular weight polymers can be also studied for electrolyte design of RFBs. In this context, molecular simulations and theoretical calculations can be employed to predict energy states, electronic configurations, and chemical interactions of ideal additives to redox active material. Multifunctional additives with optimized charge, molecular weight, size, and shape in order to inhibit both the additives transport and active ions crossover are of interest in RFBs. Further studies in this field might lead to a much-improved performance in ZIFBs and other RFBs in general.

3. Investigating other polymer membranes in terms of electrochemical durability, power density, and cost.

The PE membranes were initially selected for their good chemical stability in ZIFB electrolytes, commercial viability, and low cost. However, other polymers including PES, PBI, and SPEEK, which have been used widely in VRFBs, are also viable options to be used in iodide-based environments. Unlike PE type polymers, many of these polymers are soluble in organic solvents (such as DMF) for membrane casting via phase inversion methods. With the aid of these methods, not only can a customized pore size and structure be achieved, but also a desirable amount of inorganic additives such as silica, alumina, and graphene can be also strategically introduced to the polymer matrix to further minimize active ion crossover. The membrane development of ZIFBs is a long path full of opportunities that could lead to the future commercialization of this promising RFB system.

References

[1] C. Zhang, L. Zhang, Progress and prospects of next-generation redox flow batteries, Energy Storage Materials. 15 (2018) 324–350. https://doi.org/10.1016/j.ensm.2018.06.008.

[2] C. Choi, S. Kim, R. Kim, Y. Choi, S. Kim, H. Jung, A review of vanadium electrolytes for vanadium redox fl ow batteries, Renewable and Sustainable Energy Reviews. 69 (2017) 263–274. https://doi.org/10.1016/j.rser.2016.11.188.

[3] C.G. Armstrong, K.E. Toghill, Stability of molecular radicals in organic non-aqueous redox flow batteries: A mini review, Electrochemistry Communications. 91 (2018) 19–24. https://doi.org/10.1016/j.elecom.2018.04.017.

[4] R. Ye, D. Henkensmeier, S.J. Yoon, Z. Huang, D.K. Kim, Z. Chang, S. Kim, R. Chen, Redox Flow Batteries for Energy Storage: A Technology Review, Journal of Electrochemical Energy Conversion and Storage. 15 (2018) 1–21. https://doi.org/10.1115/1.4037248.

[5] C. Zhang, L. Zhang, Y. Ding, S. Peng, X. Guo, Y. Zhao, G. He, G. Yu, Progress and prospects of next-generation redox flow batteries, Energy Storage Materials. 15 (2018) 324–350. https://doi.org/10.1016/j.ensm.2018.06.008.

[6] P. Alotto, M. Guarnieri, F. Moro, Redox flow batteries for the storage of renewable energy: A review, Renewable and Sustainable Energy Reviews. 29 (2014) 325–335. https://doi.org/10.1016/j.rser.2013.08.001.

[7] L. Cao, M. Skyllas-kazacos, C. Menictas, J. Noack, A review of electrolyte additives and impurities in vanadium redox flow batteries, Journal of Energy Chemistry. 27 (2018) 1269–1291. https://doi.org/10.1016/j.jechem.2018.04.007.

[8] A.Z. Weber, M.M. Mench, J.P. Meyers, P.N. Ross, J.T. Gostick, Q. Liu, Redox flow batteries: a review, Journal of Applied Electrochemistry. 41 (2011) 1137–1164. https://doi.org/10.1007/s10800-011-0348-2.

[9] J. Noack, N. Roznyatovskaya, T. Herr, P. Fischer, The Chemistry of Redox-Flow Batteries, Angewandte Chemie International Edition. 54 (2015) 9776–9809. https://doi.org/10.1002/anie.201410823.

[10] S.C. Chieng, M. Kazacos, M. Skyllas-Kazacos, Modification of Daramic, microporous separator, for redox flow battery applications, Journal of Membrane Science. 75 (1992) 81–91. https://doi.org/10.1016/0376-7388(92)80008-8.

[11] A. Khor, P. Leung, M.R. Mohamed, C. Flox, Q. Xu, L. An, R.G.A. Wills, J.R. Morante, A.A. Shah, Review of zinc-based hybrid flow batteries: From fundamentals to applications, Materials Today Energy. 8 (2018) 80–108. https://doi.org/10.1016/j.mtener.2017.12.012.

[12] Y. Shi, C. Eze, B. Xiong, W. He, H. Zhang, T.M. Lim, A. Ukil, J. Zhao, Recent development of membrane for vanadium redox flow battery applications: A review, Applied Energy. 238 (2019) 202–224. https://doi.org/10.1016/j.apenergy.2018.12.087.

[13] W. Wang, V. Sprenkle, Redox flow batteries go organic, Nature Chemistry. 8 (2016) 204–206. https://doi.org/10.1038/nchem.2466.

[14] H. Chen, T.N. Cong, W. Yang, C. Tan, Y. Li, Y. Ding, Progress in electrical energy storage system: A critical review, Progress in Natural Science. 19 (2009) 291–312.

https://doi.org/10.1016/j.pnsc.2008.07.014.

[15] C. Xie, H. Zhang, W. Xu, W. Wang, X. Li, A Long Cycle Life, Self-Healing Zinc–Iodine Flow Battery with High Power Density, Angewandte Chemie - International Edition. 130 (2018) 1–7. https://doi.org/10.1002/ange.201803122.

[16] J. Zhang, G. Jiang, P. Xu, A. Ghorbani Kashkooli, M. Mousavi, A. Yu, Z. Chen, An all-aqueous redox flow battery with unprecedented energy density, Energy and Environmental Science. 11 (2018) 2010–2015. https://doi.org/10.1039/c8ee00686e.

[17] G. Weng, Z. Li, G. Cong, Y. Zhou, Y. Lu, Unlocking the capacity of iodide for high-energy-density zinc/polyiodide and lithium/polyiodide redox flow batteries, Energy & Environmental Science. 10 (2017) 735–741. https://doi.org/10.1039/C6EE03554J.

[18] C.A. Aubin, S. Choudhury, R. Jerch, L.A. Archer, J.H. Pikul, R.F. Shepherd, Electrolytic vascular systems for energy-dense robots, Nature. 571 (2019) 51–57. https://doi.org/10.1038/s41586-019-1313-1.

[19] B. Li, Z. Nie, M. Vijayakumar, G. Li, J. Liu, V. Sprenkle, W. Wang, Ambipolar zinc-polyiodide electrolyte for a high-energy density aqueous redox flow battery, Nature Communications. 6 (2015) 1–8. https://doi.org/10.1038/ncomms7303.

[20] K.J. Kim, M.S. Park, Y.J. Kim, J.H. Kim, S.X. Dou, M. Skyllas-Kazacos, A technology review of electrodes and reaction mechanisms in vanadium redox flow batteries, Journal of Materials Chemistry A. 3 (2015) 16913–16933. https://doi.org/10.1039/c5ta02613j.

[21] Y.A. Gandomi, D.S. Aaron, J.R. Houser, M.C. Daugherty, J.T. Clement, A.M. Pezeshki, T.Y. Ertugrul, D.P. Moseley, M.M. Mench, Critical Review—Experimental Diagnostics and Material Characterization Techniques Used on Redox Flow Batteries, Journal of The Electrochemical Society. 165 (2018) A970–A1010. https://doi.org/10.1149/2.0601805jes.

[22] J. Winsberg, T. Hagemann, T. Janoschka, M.D. Hager, U.S. Schubert, Redox-Flow Batteries : From Metals to Organic Redox- Active Materials Angewandte, (2017) 686–711. https://doi.org/10.1002/anie.201604925.

[23] A. Townshend, Standard potentials in aqueous solutions, Analytica Chimica Acta. 198 (1987) 333–334. https://doi.org/10.1016/s0003-2670(00)85044-8.

[24] P.C. Butler, P.A. Eidler, P.G. Grimes, S.E. Klassen, R.C. Miles, Zinc/bromine batteries, in: Handbook of Batteries, 2001: pp. 37–01.

[25] L. Zhang, J. Cheng, Y. Yang, Y. Wen, Study of zinc electrodes for single flow zinc / nickel battery application, 179 (2008) 381–387. https://doi.org/10.1016/j.jpowsour.2007.12.088.

[26] J. Cheng, L. Zhang, Y. Yang, Y. Wen, G. Cao, X.-D. Wang, Preliminary study of single flow zinc–nickel battery, Electrochemistry Communications. 9 (2007) 2639–2642. https://doi.org/10.1016/j.elecom.2007.08.016.

[27] Z. Xie, Q. Su, A. Shi, B. Yang, B. Liu, J. Chen, X. Zhou, D. Cai, L. Yang, High performance of zinc-ferrum redox flow battery with Ac−/HAc buffer solution, Journal of Energy Chemistry. 25 (2016) 495–499. https://doi.org/10.1016/j.jechem.2016.02.009.

[28] K. Gong, X. Ma, K.M. Conforti, K.J. Kuttler, J.B. Grunewald, K.L. Yeager, M.Z. Bazant, S. Gu, Y. Yan, A zinc–iron redox-flow battery under $100 per kW h of system capital cost, Energy & Environmental Science. 8 (2015) 2941–2945. https://doi.org/10.1039/C5EE02315G.

[29] D.R. Martin, Lecture demonstrations of electrochemical reactions, Journal of Chemical Education. 25 (1948) 495–497.

[30] H.S. Lim, Zinc-Bromine Secondary Battery, Journal of The Electrochemical Society. 124 (1977) 1154. https://doi.org/10.1149/1.2133517.

[31] P.K. Leung, C.P. De León, F.C. Walsh, Electrochemistry Communications An undivided zinc – cerium redox fl ow battery operating at room temperature (295 K), Electrochemistry Communications. 13 (2011) 770–773. https://doi.org/10.1016/j.elecom.2011.04.011.

[32] J. Jorné, J.T. Kim, D. Kralik, The zinc-chlorine battery: half-cell overpotential measurements, Journal of Applied Electrochemistry. 9 (1979) 573–579. https://doi.org/10.1007/BF00610944.

[33] H. Prifti, A. Parasuraman, S. Winardi, T.M. Lim, M. Skyllas-Kazacos, Membranes for redox flow battery applications, Membranes. 2 (2012) 275–306. https://doi.org/10.3390/membranes2020275.

[34] B. Schwenzer, J. Zhang, S. Kim, L. Li, J. Liu, Z. Yang, Membrane development for vanadium redox flow batteries, ChemSusChem. 4 (2011) 1388–1406. https://doi.org/10.1002/cssc.201100068.

[35] X. Li, H. Zhang, Z. Mai, H. Zhang, I. Vankelecom, Ion exchange membranes for vanadium redox flow battery (VRB) applications, Energy & Environmental Science. 4 (2011) 1147. https://doi.org/10.1039/c0ee00770f.

[36] K. Lourenssen, J. Williams, F. Ahmadpour, R. Clemmer, S. Tasnim, Vanadium redox flow batteries: A comprehensive review, Journal of Energy Storage. 25 (2019) 100844. https://doi.org/10.1016/j.est.2019.100844.

[37] R. Kim, H.G. Kim, G. Doo, C. Choi, S. Kim, J. Lee, J. Heo, H. Jung, H. Kim, Ultrathin Nafion-filled porous membrane for zinc / bromine redox flow batteries, Scientific Reports. (2017) 1–8. https://doi.org/10.1038/s41598-017-10850-9.

[38] L. Zheng, H. Wang, R. Niu, Y. Zhang, H. Shi, Electrochimica Acta Sulfonated poly (ether ether ketone)/ sulfonated graphene oxide hybrid membrane for vanadium redox fl ow battery, Electrochimica Acta. 282 (2018) 437–447. https://doi.org/10.1016/j.electacta.2018.06.083.

[39] L. Yu, F. Lin, J. Xi, A recast Nafion/graphene oxide composite membrane for advanced vanadium redox flow batteries, RCS Advances. 6 (2016) 3756–3763. https://doi.org/10.1039/c5ra24317c.

[40] S.C. Chieng, M. Kazacos, M. Skyllas-Kazacos, Preparation and evaluation of composite membrane for vanadium redox battery applications, Journal of Power Sources. 39 (1992) 11–19. https://doi.org/10.1016/0378-7753(92)85002-R.

[41] J.F. Vélez, M. Aparicio, J. Mosa, Effect of Lithium Salt in Nanostructured Silica–Polyethylene Glycol Solid Electrolytes for Li-Ion Battery Applications, The Journal of Physical Chemistry C. 120 (2016) 22852–22864. https://doi.org/10.1021/acs.jpcc.6b07181.

[42] X. Wei, B. Li, W. Wang, Porous polymeric composite separators for redox flow batteries, Polymer Reviews. 55 (2015) 247–272. https://doi.org/10.1080/15583724.2015.1011276.

[43] M.S.K. T. Mohammadi, Evaluation of the chemical stability of some membrane in Vanadium solutions, Journal of Applied Chemistry. 27 (1997) 153–160.

[44] X. Wei, Z. Nie, Q. Luo, B. Li, V. Sprenkle, W. Wang, Polyvinyl Chloride/Silica Nanoporous

Composite Separator for All-Vanadium Redox Flow Battery Applications, Journal of The Electrochemical Society. 160 (2013) A1215–A1218. https://doi.org/10.1149/2.087308jes.

[45] B. Schwenzer, J. Zhang, S. Kim, L. Li, J. Liu, Z. Yang, Membrane development for vanadium redox flow batteries, ChemSusChem. 4 (2011) 1388–1406. https://doi.org/10.1002/cssc.201100068.

[46] A. Parasuraman, T.M. Lim, C. Menictas, M. Skyllas-Kazacos, Review of material research and development for vanadium redox flow battery applications, Electrochimica Acta. 101 (2013) 27–40. https://doi.org/10.1016/j.electacta.2012.09.067.

[47] H. Zhang, Y. Tan, J. Li, B. Xue, Studies on properties of rayon- and polyacrylonitrile-based graphite felt electrodes affecting Fe/Cr redox flow battery performance, Electrochimica Acta. 248 (2017) 603–613. https://doi.org/10.1016/j.electacta.2017.08.016.

[48] Y.S. Kim, S.H. Oh, Y.J. Kim, S. ji Kim, C.H. Chu, K. Park, Active material crossover through sulfonated poly (ether ether ketone) membrane in iron-chrome redox flow battery, Korean Chemical Engineering Research. 57 (2019) 17–21. https://doi.org/10.9713/kcer.2019.57.1.17.

[49] C.-Y. Sun, H. Zhang, X.-D. Luo, N. Chen, A comparative study of Nafion and sulfonated poly(ether ether ketone) membrane performance for iron-chromium redox flow battery, Ionics. 25 (2019) 4219–4229. https://doi.org/10.1007/s11581-019-02971-0.

[50] Y.S. Kim, S.H. Oh, E. Kim, D. Kim, S. Kim, C.H. Chu, K. Park, Iron-chrome crossover through nafion membrane in iron-chrome redox flow battery, Korean Chemical Engineering Research. 56 (2018) 24–28. https://doi.org/10.9713/kcer.2018.56.1.24.

[51] C. Sun, H. Zhang, Investigation of Nafion series membranes on the performance of iron-chromium redox flow battery, International Journal of Energy Research. (2019) 1–14. https://doi.org/10.1002/er.4875.

[52] Y.K. Zeng, T.S. Zhao, L. An, X.L. Zhou, L. Wei, A comparative study of all-vanadium and iron-chromium redox flow batteries for large-scale energy storage, Journal of Power Sources. 300 (2015) 438–443. https://doi.org/10.1016/j.jpowsour.2015.09.100.

[53] K. Gong, F. Xu, J.B. Grunewald, X. Ma, Y. Zhao, S. Gu, Y. Yan, All-Soluble All-Iron Aqueous Redox-Flow Battery, ACS Energy Letters. 1 (2016) 89–93. https://doi.org/10.1021/acsenergylett.6b00049.

[54] C. Tang, D. Zhou, Methanesulfonic acid solution as supporting electrolyte for zinc-vanadium redox battery, Electrochimica Acta. 65 (2012) 179–184. https://doi.org/10.1016/j.electacta.2012.01.036.

[55] C. Tang, D. Zhou, Methanesulfonic acid solution as supporting electrolyte for zinc-vanadium redox battery, Electrochimica Acta. 65 (2012) 179–184. https://doi.org/10.1016/j.electacta.2012.01.036.

[56] K. Amini, M.D. Pritzker, Electrodeposition and electrodissolution of zinc in mixed methanesulfonate-based electrolytes, Electrochimica Acta. 268 (2018) 448–461. https://doi.org/10.1016/j.electacta.2018.02.087.

[57] Z.M. and W.W. Hongzhang Zhang, Huamin Zhang, Xianfeng Li, Silica modified nanofiltration membranes with improved selectivity for redox flow battery application, Energy & Environmental Science View. 5 (2012) 6299–6303. https://doi.org/10.1039/c1ee02571f.

[58] Z. Xie, F. Xiong, D. Zhou, Study of the Ce^{3+}/Ce^{4+} Redox Couple in Mixed-Acid Media (CH_3SO_3H and H_2SO_4) for Redox Flow Battery Application, Energy & Fuels. 25 (2011) 2399–2404. https://doi.org/10.1021/ef200354b.

[59] G. Nikiforidis, W.A. Daoud, Electrochimica Acta Effect of Mixed Acid Media on the Positive Side of the Hybrid Zinc-Cerium Redox Flow Battery, Electrochimica Acta. 141 (2014) 255–262. https://doi.org/10.1016/j.electacta.2014.06.142.

[60] X. Wei, L. Li, Q. Luo, Z. Nie, W. Wang, B. Li, G. Xia, E. Miller, J. Chambers, Z. Yang, Microporous separators for Fe/V redox flow batteries, Journal of Power Sources. 218 (2012) 39–45. https://doi.org/10.1016/j.jpowsour.2012.06.073.

[61] B. Tian, C.. Yan, F.. Wang, Proton conducting composite membrane from Daramic/Nafion for vanadium redox flow battery, Journal of Membrane Science. 234 (2004) 51–54. https://doi.org/10.1016/j.memsci.2004.01.012.

[62] G. Couture, A. Alaaeddine, F. Boschet, B. Ameduri, Polymeric materials as anion-exchange membranes for alkaline fuel cells, Progress in Polymer Science (Oxford). 36 (2011) 1521–1557. https://doi.org/10.1016/j.progpolymsci.2011.04.004.

[63] S. Winardi, G. Poon, M. Ulaganathan, A. Parasuraman, Q. Yan, N. Wai, T.M. Lim, M. Skyllas-Kazacos, Effect of bromine complexing agents on the performance of cation exchange membranes in second-generation vanadium bromide battery, ChemPlusChem. 80 (2015) 376–381. https://doi.org/10.1002/cplu.201402260.

[64] P. Morrissey, D. Vesely, G. Cooley, Stability of sulphonate type membranes in aqueous bromine/bromide environments, Journal of Membrane Science. 247 (2005) 169–178. https://doi.org/10.1016/j.memsci.2004.07.034.

[65] A. Kusoglu, K.T. Cho, R.A. Prato, A.Z. Weber, Structural and transport properties of Nafion in hydrobromic-acid solutions, Solid State Ionics. 252 (2013) 68–74. https://doi.org/10.1016/j.ssi.2013.05.008.

[66] C. Choi, S. Kim, R. Kim, J. Lee, J. Heo, H.-T. Kim, In-situ observation of the degradation of all-vanadium redox flow batteries with dynamic hydrogen reference electrode under real operation conditions, Journal of Industrial and Engineering Chemistry. 70 (2019) 355–362. https://doi.org/10.1016/j.jiec.2018.10.036.

[67] D.I. Kushner, A.R. Crothers, A. Kusoglu, A.Z. Weber, Transport phenomena in flow battery ion-conducting membranes, Current Opinion in Electrochemistry. (2020). https://doi.org/10.1016/j.coelec.2020.01.010.

[68] B. Li, Q. Luo, X. Wei, Z. Nie, E. Thomsen, B. Chen, V. Sprenkle, W. Wang, Capacity decay mechanism of microporous separator-based all-vanadium redox flow batteries and its recovery, ChemSusChem. 7 (2014) 577–584. https://doi.org/10.1002/cssc.201300706.

[69] Z.P. Cano, D. Banham, S. Ye, A. Hintennach, J. Lu, M. Fowler, Z. Chen, Batteries and fuel cells for emerging electric vehicle markets, Nature Energy. 3 (2018) 279–289. https://doi.org/10.1038/s41560-018-0108-1.

[70] X. Wei, W. Duan, J. Huang, L. Zhang, B. Li, D. Reed, W. Xu, V. Sprenkle, W. Wang, A High-Current, Stable Nonaqueous Organic Redox Flow Battery, ACS Energy Letters. 1 (2016) 705–711. https://doi.org/10.1021/acsenergylett.6b00255.

[71] S. Zhang, X. Li, D. Chu, An Organic Electroactive Material for Flow Batteries, Electrochimica

Acta. 190 (2016) 737–743. https://doi.org/10.1016/j.electacta.2015.12.139.

[72] K. Wang, P. Pei, Z. Ma, H. Chen, H. Xu, D. Chen, X. Wang, Dendrite growth in the recharging process of zinc–air batteries, J. Mater. Chem. A. 3 (2015) 22648–22655. https://doi.org/10.1039/C5TA06366C.

[73] B. Huskinson, M.P. Marshak, C. Suh, S. Er, M.R. Gerhardt, C.J. Galvin, X. Chen, A. Aspuru-Guzik, R.G. Gordon, M.J. Aziz, A metal-free organic–inorganic aqueous flow battery, Nature. 505 (2014) 195–198. https://doi.org/10.1038/nature12909.

[74] B. Yang, L. Hoober-Burkhardt, F. Wang, G.K. Surya Prakash, S.R. Narayanan, An Inexpensive Aqueous Flow Battery for Large-Scale Electrical Energy Storage Based on Water-Soluble Organic Redox Couples, Journal of The Electrochemical Society. 161 (2014) A1371–A1380. https://doi.org/10.1149/2.1001409jes.

[75] M. Park, J. Ryu, W. Wang, J. Cho, Material design and engineering of next-generation flow-battery technologies, Nature Reviews Materials. 2 (2017) 16080. https://doi.org/10.1038/natrevmats.2016.80.

[76] K. Lin, R. Gómez-Bombarelli, E.S. Beh, L. Tong, Q. Chen, A. Valle, A. Aspuru-Guzik, M.J. Aziz, R.G. Gordon, A redox-flow battery with an alloxazine-based organic electrolyte, Nature Energy. 1 (2016) 16102. https://doi.org/10.1038/nenergy.2016.102.

[77] A. Orita, M.G. Verde, M. Sakai, Y.S. Meng, A biomimetic redox flow battery based on flavin mononucleotide, Nature Communications. 7 (2016) 13230. https://doi.org/10.1038/ncomms13230.

[78] J. Winsberg, T. Janoschka, S. Morgenstern, T. Hagemann, S. Muench, G. Hauffman, J. Gohy, M.D. Hager, U.S. Schubert, Poly(TEMPO)/Zinc Hybrid-Flow Battery: A Novel, "Green," High Voltage, and Safe Energy Storage System, Advanced Materials. 28 (2016) 2238–2243. https://doi.org/10.1002/adma.201505000.

[79] H. Chen, G. Cong, Y. Lu, Recent progress in organic redox flow batteries: Active materials, electrolytes and membranes, Journal of Energy Chemistry. 27 (2018) 1304–1325. https://doi.org/10.1016/j.jechem.2018.02.009.

[80] F.C. Walsh, C. Ponce de Léon, L. Berlouis, G. Nikiforidis, L.F. Arenas-Martínez, D. Hodgson, D. Hall, The Development of Zn-Ce Hybrid Redox Flow Batteries for Energy Storage and Their Continuing Challenges, ChemPlusChem. 80 (2015) 288–311. https://doi.org/10.1002/cplu.201402103.

[81] M.C. Wu, T.S. Zhao, H.R. Jiang, Y.K. Zeng, Y.X. Ren, High-performance zinc bromine flow battery via improved design of electrolyte and electrode, Journal of Power Sources. 355 (2017) 62–68. https://doi.org/10.1016/j.jpowsour.2017.04.058.

[82] J. Liu, Y. Wang, Preliminary study of high energy density Zn/Ni flow batteries, Journal of Power Sources. 294 (2015) 574–579. https://doi.org/10.1016/j.jpowsour.2015.06.110.

[83] B. Li, J. Liu, Z. Nie, W. Wang, D. Reed, J. Liu, P. McGrail, V. Sprenkle, Metal–Organic Frameworks as Highly Active Electrocatalysts for High-Energy Density, Aqueous Zinc-Polyiodide Redox Flow Batteries, Nano Letters. 16 (2016) 4335–4340. https://doi.org/10.1021/acs.nanolett.6b01426.

[84] H. Pan, B. Li, D. Mei, Z. Nie, Y. Shao, G. Li, X.S. Li, K.S. Han, K.T. Mueller, V. Sprenkle, J. Liu, Controlling Solid-Liquid Conversion Reactions for a Highly Reversible Aqueous Zinc-

Iodine Battery, ACS Energy Letters. 2 (2017) 2674–2680. https://doi.org/10.1021/acsenergylett.7b00851.

[85] J. Zhang, G. Jiang, P. Xu, A.G. Kashkooli, M. Mousavi, A. Yu, Z. Chen, An all-aqueous redox flow battery with unprecedented energy density, Energy & Environmental Science. (2018). https://doi.org/10.1039/c8ee00686e.

[86] Z. Yuan, Y. Yin, C. Xie, H. Zhang, Y. Yao, X. Li, Advanced Materials for Zinc-Based Flow Battery: Development and Challenge, Advanced Materials. 31 (2019) 1902025. https://doi.org/10.1002/adma.201902025.

[87] H.R. Jiang, W. Shyy, L. Zeng, R.H. Zhang, T.S. Zhao, Highly efficient and ultra-stable boron-doped graphite felt electrodes for vanadium redox flow batteries, Journal of Materials Chemistry A. 6 (2018) 13244–13253. https://doi.org/10.1039/C8TA03388A.

[88] T. Janoschka, N. Martin, U. Martin, C. Friebe, S. Morgenstern, H. Hiller, M.D. Hager, U.S. Schubert, An aqueous, polymer-based redox-flow battery using non-corrosive, safe, and low-cost materials, Nature. 527 (2015) 78–81. https://doi.org/10.1038/nature15746.

[89] H.L. Lord, W. Zhan, J. Pawliszyn, Fundamentals and Applications of Needle Trap Devices, in: Comprehensive Sampling and Sample Preparation, Elsevier, 2012: pp. 677–697. https://doi.org/10.1016/B978-0-12-381373-2.00056-9.

[90] T. Zhou, J. Zhang, J. Qiao, L. Liu, G. Jiang, J. Zhang, Y. Liu, High durable poly(vinyl alcohol)/Quaterized hydroxyethylcellulose ethoxylate anion exchange membranes for direct methanol alkaline fuel cells, Journal of Power Sources. 227 (2013) 291–299. https://doi.org/10.1016/j.jpowsour.2012.11.041.

[91] G. Jiang, J. Zhang, J. Qiao, Y. Jiang, H. Zarrin, Z. Chen, F. Hong, Bacterial nanocellulose/Nafion composite membranes for low temperature polymer electrolyte fuel cells, Journal of Power Sources. 273 (2015) 697–706. https://doi.org/10.1016/j.jpowsour.2014.09.145.

[92] J.L. Limpo, A. Luis, Solubility of zinc chloride in ammoniacal ammonium chloride solutions, Hydrometallurgy. 32 (1993) 247–260. https://doi.org/10.1016/0304-386X(93)90028-C.

[93] M. Skyllas-Kazacos, M.H. Chakrabarti, S.A. Hajimolana, F.S. Mjalli, M. Saleem, Progress in Flow Battery Research and Development, Journal of The Electrochemical Society. 158 (2011) R55. https://doi.org/10.1149/1.3599565.

[94] C. Xie, Y. Liu, W. Lu, H. Zhang, X. Li, Highly stable zinc-iodine single flow batteries with super high energy density for stationary energy storage, Energy and Environmental Science. 12 (2019) 1834–1839. https://doi.org/10.1039/c8ee02825g.

[95] R. de Levie, Anion Bridging and Anion Electrocatalysis on Mercury, Journal of The Electrochemical Society. 118 (1971) 185C. https://doi.org/10.1149/1.2408333.

[96] J. Heyrovsky, Retarded electrodeposition of metals studied oscillographically with mercury capillary electrodes., Discussions of the Faraday Society 1. (1947) 212–225.

[97] A. Kusoglu, A.Z. Weber, New Insights into Perfluorinated Sulfonic-Acid Ionomers, Chemical Reviews. 117 (2017) 987–1104. https://doi.org/10.1021/acs.chemrev.6b00159.

[98] E.R. Nightingale, Phenomenological Theory of Ion Solvation. Effective Radii of Hydrated Ions, The Journal of Physical Chemistry. 63 (1959) 1381–1387. https://doi.org/10.1021/j150579a011.

[99] Z. Li, M.S. Pan, L. Su, P.C. Tsai, A.F. Badel, J.M. Valle, S.L. Eiler, K. Xiang, F.R. Brushett, Y.M. Chiang, Air-Breathing Aqueous Sulfur Flow Battery for Ultralow-Cost Long-Duration Electrical Storage, Joule. 1 (2017) 306–327. https://doi.org/10.1016/j.joule.2017.08.007.

[100] R.M. Darling, K.G. Gallagher, J.A. Kowalski, S. Ha, F.R. Brushett, Pathways to low-cost electrochemical energy storage: a comparison of aqueous and nonaqueous flow batteries, Energy and Environmental Science. 7 (2014) 3459–3477. https://doi.org/10.1039/C4EE02158D.

[101] Gold Supplier with High Transaction Level from Www.Alibaba.Com. Available at: Https://Www.Alibaba.Com. (Accessed: 20th September 2019).

[102] W. Lu, Z. Yuan, Y. Zhao, H. Zhang, H. Zhang, X. Li, Porous membranes in secondary battery technologies, Chemical Society Reviews. 46 (2017) 2199–2236. https://doi.org/10.1039/C6CS00823B.

[103] Z. Yuan, Y. Duan, H. Zhang, X. Li, H. Zhang, I. Vankelecom, Advanced porous membranes with ultra-high selectivity and stability for vanadium flow batteries, Energy & Environmental Science. 9 (2016) 441–447. https://doi.org/10.1039/C5EE02896E.

[104] L. Qiao, H. Zhang, W. Lu, C. Xiao, Q. Fu, X. Li, I.F.J. Vankelecom, Advanced porous membranes with slit-like selective layer for flow battery, Nano Energy. 54 (2018) 73–81. https://doi.org/10.1016/j.nanoen.2018.10.003.

[105] R. Paul, Q. Dai, C. Hu, L. Dai, Ten years of carbon-based metal-free electrocatalysts, Carbon Energy. 1 (2019) 19–31. https://doi.org/10.1002/cey2.5.

[106] C. Minke, T. Turek, Materials, system designs and modelling approaches in techno-economic assessment of all-vanadium redox flow batteries – A review, Journal of Power Sources. 376 (2018) 66–81. https://doi.org/10.1016/j.jpowsour.2017.11.058.

[107] Z. Yuan, X. Liu, W. Xu, Y. Duan, H. Zhang, X. Li, Negatively charged nanoporous membrane for a dendrite-free alkaline zinc-based flow battery with long cycle life, Nature Communications. 9 (2018) 1–11. https://doi.org/10.1038/s41467-018-06209-x.

[108] S.B. Sherman, Z.P. Cano, M. Fowler, Z. Chen, Range-extending Zinc-air battery for electric vehicle, AIMS Energy. 6 (2018) 121–145. https://doi.org/10.3934/energy.2018.1.121.

[109] J. Fu, Z.P. Cano, M.G. Park, A. Yu, M. Fowler, Z. Chen, Electrically Rechargeable Zinc–Air Batteries: Progress, Challenges, and Perspectives, Advanced Materials. 29 (2017). https://doi.org/10.1002/adma.201604685.

[110] P. Alotto, M. Guarnieri, F. Moro, Redox flow batteries for the storage of renewable energy: A review, Renewable and Sustainable Energy Reviews. 29 (2014) 325–335. https://doi.org/10.1016/j.rser.2013.08.001.

[111] M. Skyllas-Kazacos, M.H. Chakrabarti, S.A. Hajimolana, F.S. Mjalli, M. Saleem, Progress in flow battery research and development, Journal of the Electrochemical Society. 158 (2011) 7–10. https://doi.org/10.1149/1.3599565.

[112] S. Jiang, S. Lu, Y. Xiang, S.P. Jiang, The Structure–Activity Relationship in Membranes for Vanadium Redox Flow Batteries, Advanced Sustainable Systems. 3 (2019) 1900020. https://doi.org/10.1002/adsu.201900020.

[113] M. Mousavi, G. Jiang, J. Zhang, A.G. Kashkooli, H. Dou, C.J. Silva, Z.P. Cano, Y. Niu, A. Yu,

Z. Chen, Decoupled low-cost ammonium-based electrolyte design for highly stable zinc–iodine redox flow batteries, Energy Storage Materials. 32 (2020) 465–476. https://doi.org/10.1016/j.ensm.2020.06.031.

[114] K.E. Rodby, T.J. Carney, Y. Ashraf Gandomi, J.L. Barton, R.M. Darling, F.R. Brushett, Assessing the levelized cost of vanadium redox flow batteries with capacity fade and rebalancing, Journal of Power Sources. 460 (2020) 227958. https://doi.org/10.1016/j.jpowsour.2020.227958.

[115] K. Wang, L. Liu, J. Xi, Z. Wu, X. Qiu, Reduction of capacity decay in vanadium flow batteries by an electrolyte-reflow method, Journal of Power Sources. 338 (2017) 17–25. https://doi.org/10.1016/j.jpowsour.2016.11.031.

[116] C.Y. Ling, H. Cao, M.L. Chng, M. Han, E. Birgersson, Pulsating electrolyte flow in a full vanadium redox battery, Journal of Power Sources. 294 (2015) 305–311. https://doi.org/10.1016/j.jpowsour.2015.06.020.

[117] L. Yan, D. Li, S. Li, Z. Xu, J. Dong, W. Jing, W. Xing, Balancing Osmotic Pressure of Electrolytes for Nanoporous Membrane Vanadium Redox Flow Battery with a Draw Solute, ACS Applied Materials and Interfaces. 8 (2016) 35289–35297. https://doi.org/10.1021/acsami.6b12068.

[118] C. Tanford, Intrinsic Viscosity and Kinematic Viscosity, The Journal of Physical Chemistry. 59 (1955) 798–799. https://doi.org/10.1021/j150530a027.

[119] X. Wei, B. Li, W. Wang, Porous Polymeric Composite Separators for Redox Flow Batteries, Polymer Reviews. 55 (2015) 247–272. https://doi.org/10.1080/15583724.2015.1011276.

[120] A. Tang, J. Bao, M. Skyllas-kazacos, Studies on pressure losses and fl ow rate optimization in vanadium redox fl ow battery, Journal of Power Sources. 248 (2014) 154–162. https://doi.org/10.1016/j.jpowsour.2013.09.071.

[121] S.L. Huang, H.F. Yu, Y.S. Lin, Modification of Nafion® Membrane via a Sol-Gel Route for Vanadium Redox Flow Energy Storage Battery Applications, Journal of Chemistry. 2017 (2017). https://doi.org/10.1155/2017/4590952.

[122] Q.P. Jian, M.C. Wu, H.R. Jiang, Y.K. Lin, T.S. Zhao, A trifunctional electrolyte for high-performance zinc-iodine flow batteries, Journal of Power Sources. 484 (2020) 229238. https://doi.org/10.1016/j.jpowsour.2020.229238.

[123] L.F. Arenas, C. Ponce de León, F.C. Walsh, Redox flow batteries for energy storage: their promise, achievements and challenges, Current Opinion in Electrochemistry. 16 (2019) 117–126. https://doi.org/10.1016/j.coelec.2019.05.007.

[124] T. Luo, S. Abdu, M. Wessling, Selectivity of ion exchange membranes: A review, Journal of Membrane Science. 555 (2018) 429–454. https://doi.org/10.1016/j.memsci.2018.03.051.

[125] Y. Pan, S. Chou, H.K. Liu, S.X. Dou, Functional membrane separators for next-generation high-energy rechargeable batteries, National Science Review. 4 (2017) 917–933. https://doi.org/10.1093/nsr/nwx037.

[126] T.N.L. Doan, T.K.A. Hoang, P. Chen, Recent development of polymer membranes as separators for all-vanadium redox flow batteries, RSC Advances. 5 (2015) 72805–72815. https://doi.org/10.1039/c5ra05914c.

[127] D.W. Shin, M.D. Guiver, Y.M. Lee, Hydrocarbon-Based Polymer Electrolyte Membranes: Importance of Morphology on Ion Transport and Membrane Stability, Chemical Reviews. 117 (2017) 4759–4805. https://doi.org/10.1021/acs.chemrev.6b00586.

[128] W. Wang, Z. Nie, B. Chen, F. Chen, Q. Luo, X. Wei, G. Xia, M. Skyllas-Kazacos, L. Li, Z. Yang, A New Fe/V Redox Flow Battery Using a Sulfuric/Chloric Mixed-Acid Supporting Electrolyte, Advanced Energy Materials. 2 (2012) 487–493. https://doi.org/10.1002/aenm.201100527.

[129] X.Z. Yuan, C. Song, A. Platt, N. Zhao, H. Wang, H. Li, K. Fatih, D. Jang, A review of all-vanadium redox flow battery durability: Degradation mechanisms and mitigation strategies, International Journal of Energy Research. 43 (2019) 6599–6638. https://doi.org/10.1002/er.4607.

[130] D.J. Johnson, W.A. Suwaileh, A.W. Mohammed, N. Hilal, Osmotic's potential: An overview of draw solutes for forward osmosis, Desalination. 434 (2018) 100–120. https://doi.org/10.1016/j.desal.2017.09.017.

[131] D. Zhao, S. Chen, C.X. Guo, Q. Zhao, X. Lu, Multi-functional forward osmosis draw solutes for seawater desalination, Chinese Journal of Chemical Engineering. 24 (2016) 23–30. https://doi.org/10.1016/j.cjche.2015.06.018.

[132] K. Boto, Organic additives in zinc electroplating, Electrodeposition and Surface Treatment. 3 (1975) 77–95. https://doi.org/10.1016/0300-9416(75)90048-6.

[133] S. Halonen, T. Kangas, M. Haataja, U. Lassi, Urea-Water-Solution Properties: Density, Viscosity, and Surface Tension in an Under-Saturated Solution, Emission Control Science and Technology. 3 (2017) 161–170. https://doi.org/10.1007/s40825-016-0051-1.

[134] S.K. Yen, F. Mehnas Haja N., M. Su, K.Y. Wang, T.S. Chung, Study of draw solutes using 2-methylimidazole-based compounds in forward osmosis, Journal of Membrane Science. 364 (2010) 242–252. https://doi.org/10.1016/j.memsci.2010.08.021.

[135] J.S. Yong, W.A. Phillip, M. Elimelech, Coupled reverse draw solute permeation and water flux in forward osmosis with neutral draw solutes, Journal of Membrane Science. 392–393 (2012) 9–17. https://doi.org/10.1016/j.memsci.2011.11.020.

[136] D. Aaron, Z. Tang, A.B. Papandrew, T.A. Zawodzinski, Polarization curve analysis of all-vanadium redox flow batteries, Journal of Applied Electrochemistry. 41 (2011) 1175–1182. https://doi.org/10.1007/s10800-011-0335-7.

[137] C.N. Sun, Z. Tang, C. Belcher, T.A. Zawodzinski, C. Fujimoto, Evaluation of Diels-Alder poly(phenylene) anion exchange membranes in all-vanadium redox flow batteries, Electrochemistry Communications. 43 (2014) 63–66. https://doi.org/10.1016/j.elecom.2014.03.010.

[138] K. Amini, M.D. Pritzker, In situ polarization study of zinc–cerium redox flow batteries, Journal of Power Sources. 471 (2020) 228463. https://doi.org/10.1016/j.jpowsour.2020.228463.

[139] V.R.N. Telis, J. Telis-Romero, H.B. Mazzotti, A.L. Gabas, Viscosity of aqueous carbohydrate solutions at different temperatures and concentrations, International Journal of Food Properties. 10 (2007) 185–195. https://doi.org/10.1080/10942910600673636.

[140] K. Lourvand, Thesis for doctor of philosophy in chemical engineering, 1995. https://bionumbers.hms.harvard.edu/bionumber.aspx?id=110368&ver=0.

[141] L.Y. Huang, W.A. Catterall, G. Ehrenstein, Selectivity of cations and nonelectrolytes for acetylcholine-activated channels in cultured muscle cells., Journal of General Physiology. 71 (1978) 397–410. https://doi.org/10.1085/jgp.71.4.397.

Appendix A
Molar Capacity Calculations

The volumetric discharge capacity per molar concentration of I^- or I_3^- containing salts (NH_4I, NH_4I_3, or ZnI_2) initially dissolved in catholyte.

$$\mathbf{C_n = \frac{C_V}{c_s}} \qquad \textbf{(A-1)}$$

Calculation and comparison of AC-ZIFB and AC-ZI_3FB at different concentrations as well as data presented in the literature [19] for conventional ZIFB.

$$\mathbf{C_v = \frac{Q_e}{V_s} = \frac{n_e\, F}{\frac{n_s}{c_s}} = \frac{n_e}{n_s}\, Fc_s = \xi_{e/s} Fc_s} \qquad \textbf{(A-2)}$$

$$\mathbf{C_n = \xi_{e/s} F} \qquad \textbf{(A-3)}$$

Where C_V and C_n are the volumetric capacity (for a given salt concentration of c_s in catholyte) and normalized molar capacity, respectively; Q_e and V_s are total quantity of electric charge from the electrochemical conversion between iodide and triiodide/iodine in catholyte and the volume of the catholyte, respectively; F is Faraday constant; n_e is the molar amount of transferred electrons and n_s is the molar amount of the salt in the fixed volume of catholyte where the subscript s means NH_4I, NH_4I_3, or ZnI_2 dissolved in catholyte; $\xi_{e/s}$ means the stoichiometric number of transferred electrons with respect to different salt solutes according to the reaction in equation 1. $\xi_{e/s}$ equals to 2/3, 2 and 4/3 for NH_4I, NH_4I_3, or ZnI_2, respectively. Then, the theoretical molar capacities of NH_4I, NH_4I_3, or ZnI_2 are 17.87, 53.60, and 35.74 Ah mol^{-1}, respectively.

Appendix B

Theoretical Capacity and Energy Density Calculations

The calculation of the theoretical volumetric capacity (C_V, Ah L^{-1}) and volumetric energy density (E_V, Wh L^{-1}) in the redox flow battery is through the following equation by knowing the stoichiometric ratio of transferred electron to iodine or iodide reactant (ξ), Faraday's constant (F), concentration of iodine or iodide reactant in the catholyte (c), and open circuit voltage (OCV)[16]:

$$\mathbf{C_V=\frac{F\times c\times \xi}{3600}} \qquad \textbf{(A-4)}$$

$$\mathbf{E_V=C_V\times OCV} \qquad \textbf{(A-5)}$$

ZIFB and AC-ZIFB systems: For 5 M of ZnI_2 solution as catholyte and unlimited amount of ZnI_2 as anolyte in the ZIFB system, we can calculate the theoretical volumetric capacity and energy density as follows:

$$\mathbf{Zn^{2+}+3I^-\rightarrow Zn+I_3^-} \quad \mathbf{E=-1.299\ V} \qquad \textbf{(A-6)}$$

$$\mathbf{C_v=\frac{96485\times 10\times \frac{2}{3}}{3600}=178.7\ (Ah\ L^{-1})} \qquad \textbf{(A-7)}$$

$$\mathbf{E_v=178.7\times 1.299=232.1\ (Wh\ L^{-1})} \qquad \textbf{(A-8)}$$

Without considering the presence of Cl^- ions in NH_4I catholyte in an AC-ZIFB system, the theoretical volumetric capacity and energy density of 4.5 M I^- catholyte composition in an AC-ZIFB test cell can be calculated as follows:

$$\mathbf{C_v=\frac{96485\times 4.5\times \frac{2}{3}}{3600}=80.4\ (Ah\ L^{-1})} \qquad \textbf{(A-9)}$$

$$E_v = 80.4 \times 1.299 = 104.4 \ (Wh\ L^{-1}) \quad (A\text{-}10)$$

Additionally, the presence of Cl^- ions in catholyte solution (I^- : Cl^- ratio of 2:1) leads to the following reaction:

$$Zn^{2+} + 2I^- + Cl^- \rightarrow Zn + I_2Cl^- \qquad E = -1.37\ V \quad (A\text{-}11)$$

In this case, for the concentration of 4.5 M NH_4I/2.25 M NH_4Cl catholyte if only the formation of I_2Cl^- happens, the energy density and capacity would be as follows:

$$C_v = \frac{96485 \times 4.5 \times 1}{3600} = 120.6 \ (Ah\ L^{-1}) \quad (A\text{-}12)$$

$$E_v = 120.6 \times 1.299 = 156.7 \ (Wh\ L^{-1}) \quad (A\text{-}13)$$

Since both reaction (A-6) and (A-11) exist in the catholyte of an AC-ZIFB test cell to some extent, the volumetric energy density and capacity of 4.5 M I^- catholyte composition in an AC-ZIFB test cell would be a value between 104.4 to156.7 Wh L^{-1}, and 80.4 to 120.6 Ah L^{-1}, respectively. Similarly, the volumetric energy density and capacity of 6.5 M I^- catholyte composition (of 6.5 M NH_4I/1.5 M NH_4Cl) in an AC-ZIFB test cell would be a value between 150.9 to185.6 Wh L^{-1}, and 116.1 to 142.9 Ah L^{-1}.

ZI_3FB and AC-ZI_3FB systems: With a similar approach, for 2.6 M NH_4I_3 catholyte composition and unlimited amount of NH_4Cl as anolyte in the ZI_3FB system, we can calculate the theoretical volumetric capacity and energy density as follows:

$$Zn + I_3^- \rightarrow Zn^{2+} + 3I^- \qquad E = 1.299\ V \quad (A\text{-}14)$$

$$C_V = \frac{96485 \times 2.6 \times 2}{3600} = 139.4 \ (Ah\ L^{-1}) \quad (A\text{-}15)$$

$$E_V = 53.60 \times 1.299 = 181.0 \ (Wh\ L^{-1}) \quad (A\text{-}16)$$

The presence of Cl^- ions in the catholyte solution (I^-:Cl^- ratio of 2:1) can lead to I_2Cl^- formation. Theoretically, if 1.3 M NH_4Cl is added to 2.6 M NH_4I solution followed by gradually adding the I_2, the resulting catholyte composition will be 2.6 M NH_4I_3/1.3 M NH_4I_2Cl. In that case, the energy density and capacity should be calculated as follows:

$$\mathbf{Zn+I_2Cl^- \rightarrow Zn^{2+}+2I^-+Cl^-} \qquad \mathbf{E= 1.37\ V} \quad \mathbf{(A\text{-}17)}$$

$$\mathbf{C_v = \frac{96485\times 2.6\times 2}{3600} + \frac{96485\times 1.3\times 2}{3600} = 209.7} \qquad \mathbf{(Ah\ L^{-1})} \quad \mathbf{(A\text{-}18)}$$

$$\mathbf{E_v = (104.85\times 1.299)+(104.85\times 1.37) = 279.9} \qquad \mathbf{(Wh\ L^{-1})} \quad \mathbf{(A\text{-}19)}$$

Since both reactions (A-14) and (A-17) happen to some extent, the volumetric energy density and capacity for 2.6 M NH_4I/1.3 M NH_4Cl/I_2 in an AC-ZI_3FB test cell would be in the range of 181.0- to 79.9 Wh L^{-1} and 139.4 to 209.7 Ah L^{-1}, respectively.

Appendix C
Cost Calculations for AC-ZIFBs

The installed cost of ZIFB, AC-ZIFB and AC-ZI_3FB were calculated [99] using the following equation:

$$\mathbf{C_{installed}=\left(\frac{C_{power}+C_{bop}}{t_d}+C_{energy}\right)\times(1+f_{installed})+\frac{C_{add}}{t_d}} \quad \textbf{(A-20)}$$

where C_{power} is the cost of power including the cell stack cost. C_{energy} is the cost of energy, which is the combined cost of anolyte and catholyte. C_{bop} is the balance-of-plant cost including the costs of accessories (heating/cooling equipment, state-of-charge and power managing electronics, and pumps, needed to run a flow battery system). C_{add} is the additional cost such as sales, administration, depreciation, warranty, research and development, profit margin, etc. $f_{installed}$ is the system installation cost adjustment factor, and t_d is the storage duration (hour). We considered 202.5 US$/kW and 87.5 US$/kW, and 20.5% for C_{bop} and C_{add}, and $f_{installed}$, [99] respectively. The C_{power} and C_{energy} calculation will be explained in the next sections.

Chemical cost calculation (C_{energy}): The chemical cost of storage (CCS) can be calculated from Eq. A-21.

$$\mathbf{C_{energy}=\frac{C\ chemical+C\ tank}{\varepsilon_{sys,d}\times\varepsilon_{q,rt}\times\varepsilon_{v,d}}} \quad \textbf{(A-21)}$$

Where C chemical is the combined cost of chemicals used in the anolyte and catholyte, and the C tank is the bulk tank price (US$0.15/L)[99] normalized by the energy density (kWh/L). In the denominator, $\varepsilon_{sys,d}$ is the system round trip efficiency taken as a constant of 0.94 [99]; $\varepsilon_{q,rt}$ is the Coulombic efficiency of system, while $\varepsilon_{v,d}$ is the discharge voltage divided by cell open circuit voltage. The calculations were done based on 50% state of charge (SOC) for all systems.

Assuming a 1 Ah system, the chemical cost can be calculated based on Eqs. A-22– A-24:

$$\mathbf{C_{chemical}\ (CCS)\left(\frac{US\ \$}{kWh}\right)=\frac{Cost\ of\ anolyte+Cost\ of\ catholyte}{OCV\times 1\times 0.001}} \quad \mathbf{(A\text{-}22)}$$

$$\mathbf{Cost\ of\ anolyte\ (US\ \$)=\left[P_a\times C_a+P_{a,s}\times C_{a,s}\right]\times\frac{1\ Ah}{Cap_a}} \quad \mathbf{(A\text{-}23)}$$

$$\mathbf{Cost\ of\ catholyte\ (US\ \$)=\left[P_c\times C_c+P_{c,s}\times C_{c,s}\right]\times\frac{1\ Ah}{Cap_c}} \quad \mathbf{(A\text{-}24)}$$

Where in the anolyte and catholyte, the P_a and P_c is the price $\left(\frac{\text{US \$}}{\text{mol}}\right)$ of active material, C_a and C_c are the concentration $\left(\frac{\text{mol}}{\text{L}}\right)$ of the active materials, $P_{a,s}$ and $P_{c,s}$ are the cost $\left(\frac{\text{US \$}}{\text{mol}}\right)$ of the supporting materials, $C_{a,s}$ and $C_{c,s}$ are the concentration $\left(\frac{\text{mol}}{\text{L}}\right)$ of supporting electrolyte, and Cap_a and Cap_c are the capacity $(\frac{\text{Ah}}{\text{L}})$ at the given concentration. The bulk prices for ZnI_2, NH_4I, I_2, $ZnCl_2$, and NH_4Cl are listed in Table A. 1, and the chemical cost calculation details by using the above equations are presented in Table A. 2 and Table A. 3.

Table A. 1. The bulk cost for chemicals used in the catholyte and anolyte of ZIFB, AC-ZIFB and AC-ZI$_3$FB systems.

Electrolyte Compound	M_w (g mol^{-1})	Price ($ kg^{-1})
ZnI_2	319.2	15.00[101]
NH_4I	144.9	2.70[101]
I_2	253.8	10.00[101]
NH_4Cl	53.5	0.14[99]
$ZnCl_2$	136.3	1.00[99]

Table A. 2. Details regarding electrolyte cost calculation for ZIFB, AC-ZIFB and AC-ZI_3FB systems, using volumetric capacity at 50% SOC.

System	Electrolytes	Electrolyte Component	Molar ratio	Price ($ mol^{-1})	C (mol L^{-1})	Capacity (Ah L^{-1})	Cost (US $)	Total Cost (US $)
ZIFBs	Catholyte	catholyte	ZnI_2 : 1	4.785	5.00	80.42	0.298	0.298
	Anolyte	anolyte	ZnI_2 : 1	4.785	5.00	80.42	0.298	0.298
AC-ZIFBs	Catholyte	catholyte	NH_4I: 1	0.392	6.50	57.47	0.044	0.045
		Supporting	NH_4Cl: 0.5	0.008	3.25	57.47	0.000	
	Anolyte	anolyte	$ZnCl_2$: 0.5	0.136	3.25	57.47	0.008	0.008
		Supporting	NH_4Cl: 0.5	0.008	3.25	57.47	0.000	
AC-ZI_3FBs	Catholyte	catholyte	NH_4I: 1	0.393	2.60	66.91	0.015	0.114
		catholyte	I_2: 1	2.540	2.60	66.91	0.099	
		Supporting	NH_4Cl: 1.5	0.008	3.90	66.91	0.000	
	Anolyte	Anolyte	NH_4Cl: 1	0.005	2.60	66.91	0.000	0.001
		Supporting	NH_4Cl: 1.5	0.008	3.90	66.91	0.000	

Table A. 3. Details regarding cost of energy calculation for ZIFB, AC-ZIFB and AC-ZI_3FB systems.

System	Cost of Catholyte (US $)	Cost of Anolyte (US $)	Voltage (V)	$C_{chemical}$ ($/kWh)	C_{tank} ($/kWh)	ε_{sys} (%)	$\varepsilon_{q,rt}$ (%)	$\varepsilon_{v,d}$ (%)	C_{energy} ($/kWh)
ZIFBs	0.298	0.298	1.22	487.71	1.53	0.94	0.90	0.79	734.91
AC-ZIFBs	0.045	0.008	1.21	43.66	2.16	0.94	0.99	0.88	55.67
AC-ZI_3FBs	0.114	0.001	1.22	94.27	1.84	0.94	0.96	0.88	121.71

Cost of power calculation (C_{power}): The power cost was calculated according to Eq. A-25:

$$\mathbf{C_{power}\left(\frac{US\ \$}{kWh}\right)=\frac{C_a}{\varepsilon_{sys,d}\times V\times I}} \qquad \textbf{(A-25)}$$

where C_a is total cell stack component cost per unit area $\left(\frac{\text{US }\$}{m^2}\right)$; V is the average discharge voltage of the cell (V), I is current density $\left(\frac{A}{m^2}\right)$; and $\varepsilon_{sys,d}$ is the system round trip efficiency as defined earlier. C_a depends on the cost of each stack component, as are represented in Table A. 4.

Table A. 4. Details regarding cost of power calculation for ZIFB, AC-ZIFB and AC-ZI_3FB systems.

System	Membrane ($ m^{-2})	Zinc plate ($ m^{-2})	GF/fiber – paper ($ m^{-2})	Frames, seals, and manifolds ($ m^{-2})	Stainless steel ($ m^{-2})	$C_{cell\ stack}$ ($ m^{-2})	I (A m^{-2})	V_d (V)	C_{power} ($/kWh)
ZIFBs	500.00	-	4.14 [99]	2.00 [99]	5.90 [99]	522.08	50	0.96	11,570.92
AC-ZIFBs	500.00	-	4.14 [99]	2.00 [99]	5.90 [99]	522.08	200	1.07	2,595.35
AC-ZI_3FBs	500.00	13.3 [99]	4.14 [99]	2.00 [99]	5.90 [99]	531.20	100	1.05	5,381.97

Cost calculation of AC-ZIFBs with predicted price for Nafion 117. The cost calculation of the AC-ZIFBs with the predicted future cost of Nafion 117 membrane (75 US$/m^2) was done using the same cost calculation. Since the chemical was not changed, only the cost of power calculation was repeated as presented in Table A. 5.

Table A. 5. Cost of power calculation for AC-ZIFB using the predicted future cost of the Nafion membrane.

Membrane (US$ m^{-2})	GF/fiber – paper (US$ m^{-2})	Frames, seals, and manifolds (US$ m^{-2})	Stainless steel (US$ m^{-2})	$C_{cell\ stack}$ (US$ m^{-2})	I (A m^{-2})	V_d (V)	C_{power} ($/kWh)
75.00[99]	4.14[99]	2.00[99]	5.90[99]	97.08	200	1.07	482.60

Cost calculation of AC-ZIFBs with polyolefin (PE) membrane. Similarly, the cost calculation of the AC-ZIFBs with PE membrane (10 US$/$m^2$) was done using the same cost calculation. Since 5 M AC-ZIFB was tested for evaluations, both chemical and power cost calculations were repeated as presented in Table A. 6 - Table A. 8.

Table A. 6. The cost of electrolyte for AC-ZIFB system with PE membrane in cell stack.

Electrolytes	Electrolyte Component	Molar ratio	Price ($ mol L^{-1})	C (mol L^{-1})	Capacity (Ah L^{-1})	Cost (US $)	Total Cost (US $)
Catholyte	Catholyte	NH_4I: 1	0.363	5.0	41.53	0.047	0.048
	Supporting	NH_4Cl: 0.5	0.008	2.5	41.53	0.000	
Anolyte	Anolyte	$ZnCl_2$: 0.5	0.136	2.5	41.53	0.008	0.009
	Supporting	NH_4Cl: 0.5	0.008	2.5	41.53	0.001	

Table A. 7. Details regarding cost of energy calculation for an AC-ZIFB test cell by using PE membrane in cell stack.

Cost of Catholyte (US $)	Cost of Anolyte (US $)	Voltage (V)	$C_{chemical}$ ($/kWh)	C_{tank} ($/kWh)	ε_{sys} (%)	$\varepsilon_{q,rt}$ (%)	$\varepsilon_{v,d}$ (%)	C_{energy} ($/kWh)
0.048	0.009	1.20	46.86	3.01	0.94[99]	0.93	0.98	58.01

Table A. 8. Details regarding cost of power for an AC-ZIFB test cell by using PE membrane in cell stack.

Membrane ($ m^{-2})	GF/fiber – paper ($ m^{-2})	Frames, seals, and manifolds ($ m^{-2})	Stainless steel ($ m^{-2})	$C_{cell\ stack}$ ($ m^{-2})	I (A m^{-2})	V_d (V)	C_{power} ($/kWh)
10[60]	4.14[99]	2.00[99]	5.90[99]	32.08	800	1.18	36.15

Appendix D

Cost Calculations for AC-ZIFBs with organic compound additives

The installed cost of pristine AC-ZIFB and AC-ZIFB with organic additives were calculated using Equation A-21- A-24 [99] . The bulk prices for NH_4I, $ZnCl_2$, NH_4Cl, urea, and α-D-Glucose are listed in Table A. 9, and the chemical cost and power cost calculation details by using the equations are presented in Table A. 10 - A-12.

Table A. 9. The bulk cost for chemicals used in the catholyte and anolyte of AC-ZIFBs with additives.

Electrolyte Compound	M_w (g mol^{-1})	Price ($ kg^{-1})
NH_4I	144.9	2.70 [101]
NH_4Cl	53.5	0.14 [99]
$ZnCl_2$	136.3	1.00 [99]
α-D-Glucose	180	2.5 [101]
Urea	60	1.5 [101]

Table A. 10. Details regarding electrolyte cost calculation for AC-ZIFBs with additives, using volumetric capacity at 50% SOC.

System	Electrolytes	Electrolyte Component	Molar ratio	Price ($ mol^{-1})	C (mol L^{-1})	Capacity (Ah L^{-1})	Cost (US $)	Total Cost (US $)
AC-AC-ZIFBs	Catholyte	catholyte	NH_4I: 1	0.392	5.0	41.53	0.047	0.048
		Supporting	NH_4Cl: 0.5	0.008	2.5	41.53	0.000	
	Anolyte	anolyte	$ZnCl_2$: 0.5	0.136	2.5	41.53	0.008	0.008
		Supporting	NH_4Cl: 0.5	0.008	2.5	41.53	0.000	
0.1 M Glucose	Catholyte	catholyte	NH_4I: 1	0.392	5.0	41.53	0.047	0.048
		Supporting	NH_4Cl: 0.5	0.008	2.5	41.53	0.000	
	Anolyte	anolyte	$ZnCl_2$: 0.5	0.136	2.5	41.53	0.008	0.010
		Supporting	NH_4Cl: 0.5	0.008	2.5	41.53	0.000	
		Supporting	Glucose:0.05	0.45	0.1	41.53	0.001	
0.5 M Glucose	Catholyte	catholyte	NH_4I: 1	0.392	5.0	41.53	0.047	0.048
		Supporting	NH_4Cl: 0.5	0.008	2.5	41.53	0.000	
	Anolyte	anolyte	$ZnCl_2$: 0.5	0.136	2.5	41.53	0.008	0.014
		Supporting	NH_4Cl: 0.5	0.008	2.5	41.53	0.000	
		Supporting	Glucose:0.1	0.45	0.5	41.53	0.005	
1.5 M Glucose	Catholyte	catholyte	NH_4I: 1	0.392	5.0	41.53	0.047	0.048
		Supporting	NH_4Cl: 0.5	0.008	2.5	41.53	0.000	
	Anolyte	anolyte	$ZnCl_2$: 0.5	0.136	2.5	41.53	0.008	0.025
		Supporting	NH_4Cl: 0.5	0.008	2.5	41.53	0.000	

		Supporting	Glucose:0.2	0.45	1.5	41.53	0.016	
0.1 M urea	Catholyte	catholyte	NH_4I: 1	0.392	5.0	41.53	0.047	0.048
		Supporting	NH_4Cl: 0.5	0.008	2.5	41.53	0.000	
	Anolyte	anolyte	$ZnCl_2$: 0.5	0.136	2.5	41.53	0.008	0.009
		Supporting	NH_4Cl: 0.5	0.008	2.5	41.53	0.000	
		Supporting	Urea:0.05	0.093	0.1	41.53	0.000	

Table A. 11. Details regarding cost of energy calculation for AC-ZIFB with additives.

System	Cost of Catholyte (US $)	Cost of Anolyte (US $)	Voltage (V)	$C_{chemical}$ ($/kWh)	C_{tank} ($/kWh)	ε_{sys} (%)	$\varepsilon_{q,rt}$ (%)	$\varepsilon_{v,d}$ (%)	C_{energy} ($/kWh)
AC-ZIFBs	0.048	0.009	1.21	50.66	3.25	0.94	0.94	0.93	65.96
0.1 M SAC-ZIFB	0.048	0.010	1.20	50.28	3.17	0.94	0.96	0.95	62.34
0.5 M SAC-ZIFB	0.048	0.014	1.20	54.92	3.20	0.94	0.95	0.94	69.11
1.5 M SAC-ZIFB	0.048	0.025	1.20	66.88	3.31	0.94	0.97	0.91	84.75
0.1 M SAC-ZIFB	0.048	0.009	1.20	49.96	3.20	0.94	0.96	0.94	62.56

Table A. 12. Details regarding cost of power calculation for ZIFB and SZIFB systems.

System	Membrane ($ m^{-2})	GF/fiber – paper ($ m^{-2})	Frames, seals, and manifolds ($ m^{-2})	Stainless steel ($ m^{-2})	$C_{cell\ stack}$ ($ m^{-2})	I (A m^{-2})	V_d (V)	C_{power} ($/kWh)
AC-ZIFBs	10[60]	4.14[99]	2.00[99]	5.90[99]	32.08	800	1.11	38.43
0.1 M SAC-ZIFB	10[60]	4.14[99]	2.00[99]	5.90[99]	32.08	800	1.14	37.42

0.5 M SAC-ZIFB	10[60]	4.14[99]	2.00[99]	5.90[99]	32.08	800	1.13	37.75
1.5 M SAC-ZIFB	10[60]	4.14[99]	2.00[99]	5.90[99]	32.08	800	1.09	39.14
0.1 M urea	10[60]	4.14[99]	2.00[99]	5.90[99]	32.08	800	1.13	37.75